JETP Letters, Vol. 77, No. 12, 2003, pp. 639–641. From Pis'ma v Zhurnal Éksperimental'noĭ i Teoreticheskoĭ Fiziki, Vol. 77, No. 12, 2003, pp. 769–771.

Vacuum Energy and the Universe in Special Relativity¶

G. E. Volovik

Low-Temperature Laboratory, Helsinki University of Technology, FIN-02015 HUT, Finland

Landau Institute of Theoretical Physics, Moscow, 117334 Russia

Received May 14, 2003

The problem of the cosmological constant and vacuum energy is usually thought of as the subject of general relativity. However, vacuum energy is important for the Universe even in the absence of gravity, i.e., in the case when Newton's constant G is exactly zero, $G = 0$. We discuss the response of the vacuum energy to the perturbations of the quantum vacuum in special relativity and find that, as in general relativity, the vacuum energy density is on the order of the energy density of matter. In general relativity, the dependence of the vacuum energy on the equation of state of matter does not contain G and thus is valid in the limit $G \longrightarrow 0$. However, the result obtained for the vacuum energy in a world without gravity, i.e., when $G = 0$ exactly, is different.

PACS numbers: 03.30.+p; 98.80.Jk

The problem of vacuum energy appears to be more general than the cosmological constant problem, which arises in general relativity [1]. Earlier, we discussed vacuum energy and its relation to the cosmological constant considering general relativity as an effective theory [2, 3]. We found that the energy of the equilibrium vacuum state at zero temperature is zero due to the general thermodynamic Gibbs–Duhem relation applied to the vacuum as a medium. The nonzero value of the vacuum energy, or more exactly the gravitating part of the vacuum energy, comes from perturbations of the vacuum state. In typical situations, the perturbations of the vacuum are caused by gravitating matter, and thus the induced vacuum energy density must be on the order of the energy density of matter, which results in a cosmological constant consistent with observations [4].

Now we extend the discussion of vacuum energy to the case of special relativity, i.e., to a Universe without gravity. Although in a world without gravity the cosmological constant is absent, the vacuum energy still plays an important role in the structure of the Universe. We find how the vacuum energy responds to matter in special relativity and how this allows us to stabilize a static special-relativity Universe filled with matter having an arbitrary equation of state.

The cosmological term in the action for general relativity is

$$S_\Lambda = -\int d^4x\sqrt{-g}\rho^{\rm vac}. \quad (1)$$

The corresponding stress-energy tensor of the vacuum is obtained by variation of the action over the metric tensor $g^{\mu\nu}$,

$$T^{\rm vac}_{\mu\nu} = \rho^{\rm vac}u_\mu u_\nu + P^{\rm vac}(u_\mu u_\nu - g_{\mu\nu}) = \rho^{\rm vac}g_{\mu\nu}. \quad (2)$$

Here, $\rho^{\rm vac}$ is the vacuum energy density and u^μ is the 4-velocity of the vacuum. Since the equation of state for the vacuum is

$$P^{\rm vac} = -\rho^{\rm vac}, \quad (3)$$

the energy-momentum tensor does not depend on the 4-velocity u^μ and thus is the same in any coordinate system.

Equation (2) with equation of state (3) is valid for the vacuum in special relativity too, i.e., in the absence of the dynamical field $g^{\mu\nu}$. These equations are obtained by the conventional procedure used in quantum field theory, when one introduces a fictitious field, such as fictitious gauge fields or a fictitious metric, and calculates the response of the vacuum to these fields. Moreover, the equation of state $P^{\rm vac} = -\rho^{\rm vac}$ is even more general, since it is valid even in the nonrelativistic theories, where the role of quantum vacuum is played by the ground state of the quantum condensed matter. This equation of state comes from the general thermodynamic Gibbs–Duhem relation applied to the homogeneous ground state of condensed matter (see, e.g., [3]).

Let us consider the Universe in special relativity (i.e., in the absence of gravity, $G = 0$), which is filled with nongravitating homogeneous matter—a perfect cosmic fluid—and discuss how the vacuum responds to

¶This article was submitted by the author in English.

the matter and stabilizes this Universe. The energy-momentum tensor of matter is

$$T^{M}_{\mu\nu} = \rho^{M} v_{\mu} v_{\nu} + P^{M}(v_{\mu} v_{\nu} - g_{\mu\nu}), \quad (4)$$

where v^{μ} is the 4-velocity of matter and ρ^{M} and P^{M} are energy density and pressure of matter in the comoving frame.

In the general coordinate frame, the energy and momentum density of matter are

$$\tilde{\rho}^{M} = \frac{\rho^{M} + \frac{v^2}{c^2}P^{M}}{1 - \frac{v^2}{c^2}}, \quad \mathbf{p}^{M} = \frac{\mathbf{v}}{c^2}\frac{\rho^{M} + P^{M}}{1 - \frac{v^2}{c^2}}. \quad (5)$$

The obvious consequence of Eq. (5) is that the energy and the momentum of matter do not satisfy the relativistic relation between the energy and momentum

$$\mathbf{P} = E\frac{\mathbf{v}}{c^2}. \quad (6)$$

The reason for this is related to the external forces acting on matter, which violate the Lorentz invariance, since they establish a preferred reference frame in which these forces are isotropic. These forces are presented in Eq. (5) through the pressure P^{M} of matter, which is supported by the external pressure (see Section 14 of [5]).

If the Universe is completely isolated from the "environment," the external pressure is absent, $P^{M} = P_{\text{external}} = 0$, and Lorentz-invariant equation (6) is restored. But the typical matter considered in cosmology, such as a relativistic plasma, does not exist at zero pressure as an equilibrium state, except for the extreme limiting case of cold matter. Thus, in special relativity, the Universe must either be empty or contain matter that can exist in equilibrium at zero pressure (the matter in a cold liquid state, for example).

The vacuum gives an alternative scenario for an equilibrium static Universe with matter to exist in special relativity. The equilibrium state is achieved when the pressure of the cosmological matter is compensated by the partial pressure of the vacuum, so that the external pressure goes to zero,

$$P_{\text{external}} = P^{\text{vac}} + P^{M} = 0, \quad (7)$$

and the Universe (matter + vacuum) can be in equilibrium without external environment. For this equilibrium Universe, Eq. (6) for the energy and momentum of the whole Universe is also restored.

Using equation of state (3) and the equilibrium condition (7), one obtains the density of the vacuum energy induced by matter with pressure P^{M} in the equilibrium Universe:

$$\rho^{\text{vac}} = P^{M}. \quad (8)$$

Since the vacuum momentum is zero,

$$\mathbf{p}^{\text{vac}} = 0, \quad (9)$$

the total energy density and momentum density of the system (matter + vacuum) become

$$\rho_{\text{total}} = \tilde{\rho}^{M} + \rho^{\text{vac}} = \frac{\rho^{M} + \rho^{\text{vac}}}{1 - \frac{v^2}{c^2}},$$
$$\mathbf{p}_{\text{total}} = \mathbf{p}^{M} + \mathbf{p}^{\text{vac}} = \frac{\mathbf{v}}{c^2}\frac{\rho^{M} + \rho^{\text{vac}}}{1 - \frac{v^2}{c^2}}. \quad (10)$$

They satisfy the relativistic equation (6), and the corresponding density of the rest mass of the system is

$$\rho_{\text{total}} = \frac{m_{\text{rest}}c^2}{\sqrt{1 - \frac{v^2}{c^2}}}, \quad m_{\text{rest}} = \frac{\rho^{M} + \rho^{\text{vac}}}{c^2\sqrt{1 - \frac{v^2}{c^2}}}. \quad (11)$$

The extra factor $\sqrt{1 - v^2/c^2}$ in the denominator of the rest mass is cancelled by the relativistic transformation of the volume: the volume V in the frame of measurement and the volume V_{comoving} in the comoving frame are related as $dV = dV_{\text{comoving}}\sqrt{1 - v^2/c^2}$, so that the total rest energy of the system is

$$M_{\text{rest}} = \int dV \frac{\rho^{M} + \rho^{\text{vac}}}{\sqrt{1 - \frac{v^2}{c^2}}} = V_0(\rho^{M} + \rho^{\text{vac}}). \quad (12)$$

Thus, the whole world represents a relativistic object whose rest mass is the sum of the rest energies of the matter and quantum vacuum. The energy density of the quantum vacuum induced by the nongravitating ($G = 0$) matter is completely determined by the equilibrium condition (7) and equation of state for matter $P^{M} = w^{M}\rho^{M}$:

$$\rho^{\text{vac}}_{G=0} = w^{M}\rho^{M}. \quad (13)$$

We can compare the vacuum energy (13) in the Universe in special relativity, i.e., when $G = 0$, with the vacuum energy in Universes in general relativity, i.e., when $G \neq 0$. For the Einstein static closed Universe [3, 6], the vacuum energy induced by the gravitating matter is

$$\rho^{\text{vac}}_{\text{Einstein}} = \frac{1}{2}(1 + 3w^{M})\rho^{M}, \quad (14)$$

and for the Gödel steady-state rotating Universe [3, 7], it is

$$\rho^{\text{vac}}_{\text{Goedel}} = -\frac{1}{2}(1 - w^{M})\rho^{M}. \quad (15)$$

In all three Universes, the density of the vacuum energy induced by matter is proportional to the energy density of matter. Equations (14) and (15) for worlds with gravity do not depend on Newton's constant G and thus are valid in the limit $G \longrightarrow 0$. But they do not coincide with Eq. (13) for a world without gravity, i.e., when G is exactly zero. While in special relativity the vacuum response to matter is determined by the condition of zero external pressure, $P_{\text{external}} = 0$, in the case of gravitating matter the condition of gravineutrality is added [3]. The pressure and energy of the gravitational field contribute to both conditions even in the limit $G \longrightarrow 0$. These contributions come from the space curvature in the Einstein Universe and from the local rotational metric in the Gödel Universe.

As distinct from static gravitating Universes, which experience different types of gravitational instabilities, in special relativity a Universe with matter is stable if the quantum vacuum itself is the stable object. In the latter case, small perturbations of the vacuum state, caused by cold or hot matter, do not destabilize the system. This fact is well known for the condensed-matter analogues of the Universe—quantum liquids, where the role of the quantum vacuum is played by the superfluid condensate and the role of the relativistic matter is played by "relativistic" quasiparticles, with c being the maximum attainable speed for low-energy quasiparticles. Examples are provided by Bose superfluid ^{4}He and Fermi superfluid ^{3}He-A. Both quantum liquids are stable at $T = 0$ and $P = 0$, and their stability is not violated by the massless "relativistic" quasiparticles that appear at $T \neq 0$ forming the analogue of matter in these toy Universes. For both liquids, equation (13) is valid with the "relativistic" equation of state $w^{\text{M}} = 1/3$ if the liquids are isolated from the environment [2]. Although in both quantum liquids there are low-frequency collective modes corresponding to the dynamics of the effective metric, this effective gravity does not obey the general covariance and is not Newtonian at large distances. As a result, the effective gravity in these liquids does not modify special-relativity equation (13).

For such condensed matter systems, the relativistic equations (10) obtained for the energy and momentum of a Universe in special relativity are also applicable, but with one reservation. As distinct from its special-relativity counterpart, the quantum vacuum (condensate) in condensed matter does not obey the effective Lorentz invariance obeyed by the excitations of the condensate—quasiparticles. In particular, the momentum density of the quantum condensate is nonzero. As distinct from Eq. (9), the superfluid condensate moving with the so-called superfluid velocity $\mathbf{u}_s$ carries the momentum density $\mathbf{p}^{\text{vac}} = mn\mathbf{u}_s$, where m is the mass of particles making up the condensate (atoms of liquid) and n is their number density. As a result, for quantum liquids, the relativistic equations are valid only in the reference frame moving with the condensate. Full correspondence between the quantum vacuum and a superfluid condensate could occur only for such hypothetical condensates whose "atoms" are massless, $m = 0$. However, the difference between the relativistic quantum vacuum and nonrelativistic quantum condensate does not change the conclusion that the vacuum response stabilizes a nongravitating Universe.

I thank A.A. Starobinsky for fruitful discussions. This work was supported by the ESF COSLAB Programme and by the Russian Foundation for Basic Research.

REFERENCES

1. S. Weinberg, Rev. Mod. Phys. **61**, 1 (1989).
2. G. E. Volovik, *The Universe in a Helium Droplet* (Clarendon Press, Oxford, 2003).
3. G. E. Volovik, gr-qc/0304061.
4. A. Riess, A. V. Filippenko, P. Challis, *et al.*, Astron. J. **116**, 1009 (1998); S. J. Perlmutter, G. Aldering, G. Goldhaber, *et al.*, Astrophys. J. **517**, 565 (1999).
5. A. Einstein, Jahrb. Radioakt. Elektron. **4**, 411 (1907).
6. A. Einstein, Sitzungsber. K. Preuss. Akad. Wiss. **1**, 142 (1917).
7. K. Gödel, Rev. Mod. Phys. **21**, 447 (1949).

JETP Letters, Vol. 77, No. 12, 2003, pp. 642–646. Translated from Pis'ma v Zhurnal Éksperimental'noĭ i Teoreticheskoĭ Fiziki, Vol. 77, No. 12, 2003, pp. 772–777.

Lyapunov Exponents in the Hénon–Heiles Problem

I. I. Shevchenko* and A. V. Mel'nikov

Pulkovo Observatory, Russian Academy of Sciences, Pulkovskoe sh. 65, St. Petersburg, 196140 Russia

**e-mail: iis@gao.spb.ru*

Received April 25, 2003; in final form, May 27, 2003

The maximal Lyapunov characteristic exponent of chaotic motion was calculated as a function of the system energy by numerical integration of the Hénon–Heiles problem. Contrary to the conclusions of Benettin *et al.* [4], this dependence is not exponential but is close to a power law. As to the energy dependence of dynamic entropy, it is close to an exponential law, in agreement with [4]. © *2003 MAIK "Nauka/Interperiodica".*

PACS numbers: 05.45.Pq

The Hénon–Heiles problem traditionally attracts the attention of researchers, because it uncovered a chaotic type of behavior in Hamiltonian mechanics [1]. The Hamiltonian of the problem has the form [1–3]

$$H = \frac{1}{2}(p_1^2 + p_2^2 + q_1^2 + q_2^2) + q_1^2 q_2 - \frac{1}{3}q_2^3, \qquad (1)$$

where q_1 and q_2 are the coordinates and p_1 and p_2 are the conjugate momenta.

Hénon and Heiles [1] numerically integrated a system described by Hamiltonian (1) to construct the Poincaré section in its phase space and reveal the regions of chaotic motion. The chaos regions expand with increasing energy and, for the energy $E \equiv H = 1/6$, almost the whole phase space accessible to the motion is filled by the chaotic component [1].

A qualitative character of the motion (regular/chaotic) can be determined by calculating the Lyapunov characteristic exponents (LCEs; see, e.g., [2]). LCE characterizes the mean velocity of the exponential divergence of close trajectories in the phase space. If the LCE is zero, the motion is regular, and if it is nonzero, the motion is chaotic. In the case of a Hamiltonian system with N degrees of freedom, the trajectory is characterized by N pairs of exponents; in each pair, the exponents are equal in magnitude but have opposite signs. To determine the character of motion, it suffices to calculate the maximal LCE (MLCE). The motion of the system is unpredictable on the time interval given by a value reciprocal of the MLCE.

Benettin *et al.* have constructed the MLCE as a function of the energy E of the system with Hamiltonian (1) (Fig. 7 in [4]). Analyzing this dependence, Benettin *et al.* concluded that it obeyed an exponential law. This widely known result is included in the Lichtenberg and Liberman's monograph devoted to nonlinear and chaotic dynamics (Fig. 5.8 in [2]).

It should be noted that this result was obtained from rather limited numerical data. Benettin *et al.* constructed 28 points in the curve for the entire energy range studied. According to the estimates presented below, a time interval of $t = 2 \times 10^4$ time units, where the authors of [4] carried out integration at each point for the system with Hamiltonian (1), is insufficient for obtaining proper asymptotic values for MLCE. In this work, we construct the curve with a considerably higher (more than a hundred times) energy resolution. The corresponding MLCEs are determined for a substantially longer time intervals, up to $t = 10^7$. The use of such times allows the resulting MLCEs to be verified much more reliably.

In calculating the MLCE, we used two methods: the method of "shadow trajectory" (used also in [4]) and the so-called HQR method.

The essence of the first method is as follows (for details, see, e.g., [2, 4, 5]). Let us take two close phase trajectories, "reference" and "shadow," which are separated at zero time by d_0. The approximation to MLCE at a time interval of n steps is calculated by the formula

$$L_n = \frac{1}{n\Delta t}\sum_{i=1}^{n} \ln\frac{d_i}{d_{i-1}}, \qquad (2)$$

where d_i is the distance between the reference and shadow trajectories at the ith step and Δt is the time step. When calculating, it is necessary to periodically renormalize the distance between the reference and shadow trajectories, in order that it be relatively small.

We take the initial values of three variables to be the same for all energies: $q_1 = 0$, $q_2 = -0.15$, and $p_2 = 0$. The value of p_1 for a given energy E is determined from Eq. (1). As in [1, 4], we set $p_1 \geq 0$. The shadow trajectory is initially displaced by $d_0 = 10^{-7}$ along the q_2 variable from the reference trajectory. The iteration step is $\Delta t = 0.1$. The magnitude of the vector of displacement from the reference to the shadow trajectory is renormalized at each iteration. Energy is varied from 0.0841 to 0.1666 (i.e., up to the limiting value $E = 1/6$) with a step

of 2×10^{-5}. Below the chosen minimal E value, the chaotic region becomes too narrow to be detected; the maximal value is chosen from the consideration that, at higher energies, the motion ceases to be oscillatory. The equations of motion were solved using the Dorman–Prince integrator [6] implementing the eighth-order Runge–Kutta method.

The MLCE was calculated four times for the same set of initial data and the time intervals $t = 10^4$, 10^5, 10^6, and 10^7. Due to the increase in t, the chaotic and regular orbits can be separated, so that one can assure whether the computation time is sufficient for determining the exact MLCE values or not: the current MLCE value must flatten out and not change with increasing computation time. Our numerical simulation indicates that the flattening time is $t = 10^5$–10^7. This time increases with a decrease in energy (Fig. 1).

The log–log plot of the calculated MLCE L against energy E, as obtained for the maximal integration time $t = 10^7$, is shown in Fig. 2. The graph of a power law $L \propto E^{\alpha}$ approximating the uppermost data at the section where the observed dependence is linear is also shown (in logarithmic coordinates, it is a straight line $\log L = \alpha \log E + \beta$). The choice of the section and the "uppermost" curve were guides to the eye and, hence, are approximate. For $t = 10^4$, 10^5, 10^6, and 10^7, we found $\alpha = 2.7$, 3.0, 3.4, and 3.6 and $\beta = 1.26$, 1.46, 1.78, and 1.95, respectively. The approximation was made for the uppermost (rather than average) values, because the so-called "stickness effect" strongly influences the observed dependence. Chaotic motion in Hamiltonian dynamics is characterized by Hamiltonian intermittence [7]: a trajectory may adhere for a long time to the boundaries of the chaotic region, where the motion is close to regular. In this case, the local LCEs are small, rendering the estimates of the resulting LCEs incorrect [7]. In Fig. 2, the stickness effect shows as downward spikes in the curve. A fine structure is also seen in the curve. It is caused by the absorption of the chaotic layers of marginal resonances by the main chaotic region as the energy increases.

The approximate exponential function $L = 0.0034\exp(22E)$ of Benettin *et al.* [4] is also drawn in Fig. 2. One can see that it satisfactorily describes the real dependence only at high energies.

We also calculated the MLCE by the HQR method suggested by von Bremen *et al.* [8]. This method allows the calculation of the entire LCE spectrum. It is based on the QR expansion of the tangential mapping matrix using the Hausholder transformation (this is reflected in the name of the method). The base algorithms were implemented in [9]. We use a modernized algorithm [10] that differs from [9] in that the tangential mapping matrix is calculated by the joint integration of the initial system and the system of variational equations.

With the Hénon–Heiles system, the second element of the Lyapunov spectrum must be zero, because the system has two degrees of freedom and is autonomous. As the computation time increases, the MLCE vs. energy curve stabilizes, whereas the curve for the energy dependence of the second element (nearly a horizontal line) moves down and tends asymptotically to the zero level. The energy dependence of the LCE obtained by the HQR method for the maximal integration time $t = 10^7$ is shown in Fig. 3. The initial conditions are the same as used above in the calculations by the shadow trajectory method. As in Fig. 2, the power-law approximation is also shown in Fig. 3. For $t = 10^4$, 10^5, 10^6, and 10^7, one has $\alpha = 2.75$, 3.1, 3.5, and 3.6 and $\beta = 1.32$, 1.55, 1.88, and 1.90, respectively.

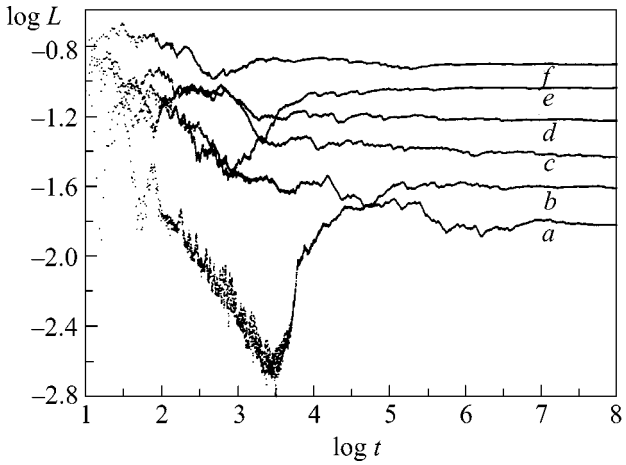

Fig. 1. Time dependence of the current MLCE value for system (1) at various energies; log$E$ = (*a*) –1.025, (*b*) –0.975, (*c*) –0.925, (*d*) –0.875, (*e*) –0.825, and (*f*) –0.780.

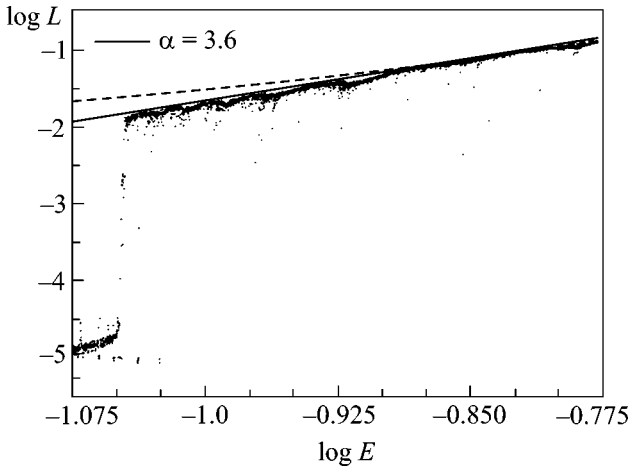

Fig. 2. Energy dependence of MLCE. The solid line is the power-law approximation, and the dashed line is the function of Benettin *et al.* [4].

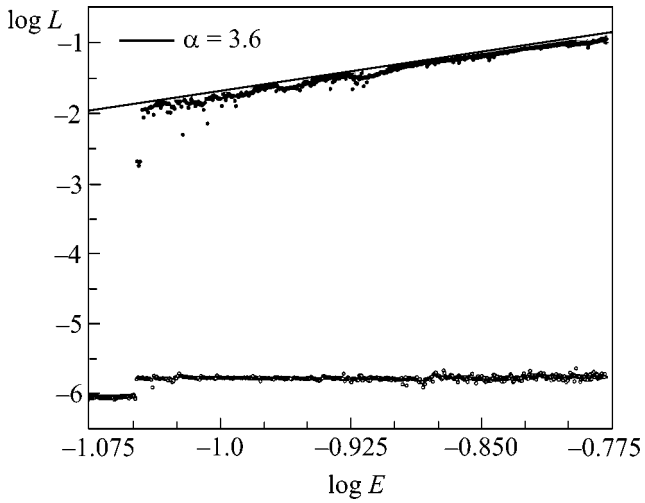

Fig. 3. Energy dependence of the LCE spectrum. A power-law approximation to the MLCE is shown.

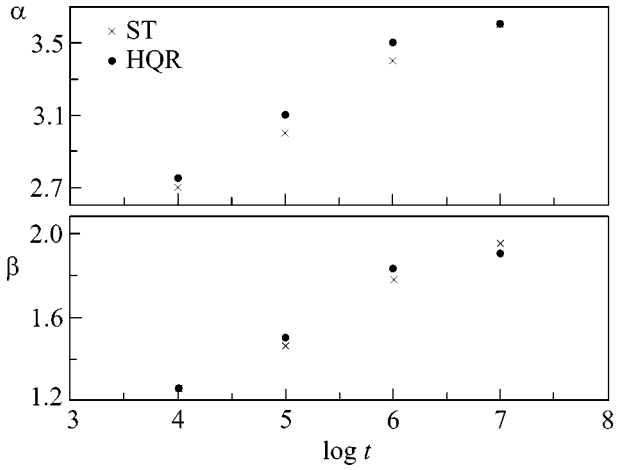

Fig. 4. The calculated α and β values as functions of the integration time. Crosses are for the shadow-trajectory method, and circles are for the HQR method.

The α and β dependences on the integration time are shown in Fig. 4 for both computational methods. The HQR data distinctly demonstrate the flattening out at large integration times. For the shadow-trajectory data, this tendency is less pronounced. However, the HQR method is, undoubtedly, more accurate. For this reason, the values $\alpha = 3.6$ and $\beta = 1.9$ can be considered accurate to 0.1.

Let us consider whether the character of the MLCE vs. energy dependence changes upon the generalization of Hamiltonian (1). The general system with the Hamiltonian

$$H = \frac{1}{2}(p_1^2 + p_2^2 + q_1^2 + q_2^2) + \varepsilon q_1^2 q_2 - \frac{1}{3}q_2^3 \qquad (3)$$

coincides with the Hénon–Heiles system (1) at $\varepsilon = 1$, and it is close to the integrable system at the ε values close to zero [3]. Figure 5 presents the shadow-trajectory ($t = 10^6$) MLCE energy dependence for $\varepsilon = 0.5$, 0.8, and 1.0. One can see from the figure that, as ε decreases, the curve moves down in parallel to itself. Hence, the character of the dependence is retained and expressed as a power law $\log L = \alpha \log E + \beta$ with the same coefficient $\alpha = 3.4$. One can assume that, as t increases, the ultimate α value would be 3.6, as in the case of Hamiltonian (1). The parameter β for the curves in Fig. 5 is equal to 1.78, 1.45, and 1.18.

Apart from the LCE, the relative measure μ of a chaotic component in the phase space, when determined, is an important characteristic of the chaotic motion. Hénon and Heiles [1] calculated the relative area $\tilde{\mu} = 1 - \mu$ occupied by the regular trajectories of a system with Hamiltonian (1) at the (q_2, p_2) surface of section for $q_1 = 0$ and a fixed E (for a given E, p_1 can be found from Eq. (1); only the values $p_1 \geq 0$ are used). The resulting energy dependence of this area is presented in Fig. 7 in [1]. This graph has received wide acceptance and, in particular, is presented in [11]. As for the energy dependence of the MLCE [4], it was constructed using rather limited numerical data. In this work, we use three independent methods for calculating μ.

The first one was proposed by Hénon and Heiles in [1]. The essence of this method is as follows. On the surface of a certain phase-space section, the initial values of the variables (q_2, p_2) are fixed, whereupon the equations of motion are integrated for two close (reference and shadow) trajectories. The separation between them is calculated at the final point of integration. If the initial data correspond to the chaotic component, the separation between the reference and shadow trajectories increases exponentially with time. No exponential

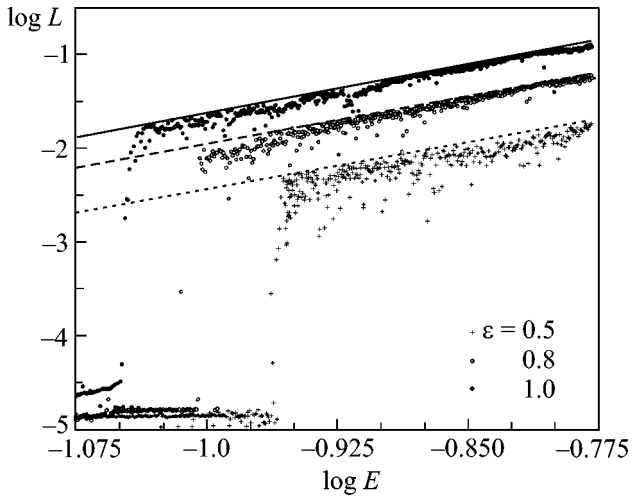

Fig. 5. Energy dependence of MLCE for a system with generalized Hamiltonian (3); ε = (crosses) 0.5, (circles) 0.8, and (points) 1.

increase occurs for the regular trajectory. Therefore, one can distinguish between the chaotic and regular trajectories. The initial data grid is specified, and then the relative measure of the chaotic region is determined from the relative number of the chaotic trajectories on the grid.

The initial conditions are taken as follows: $q_1 = 0$ and q_2 and p_2 are specified on a uniform rectangular grid $q_2 \in [-0.6, 1.1]$ and $p_2 \in [-0.7, 0.7]$; p_1 is determined by Eq. (1) for given q_1, q_2, p_2, and E. As in the case of MLCE, the shadow trajectory is shifted by 10^{-7} along the q_2 coordinate from the reference trajectory. To separate the chaotic and regular trajectories, the distribution of distances between the final phase-trajectory points is constructed. The separation criterion is determined from the analysis of mode distribution. A similar procedure, although for the MLCE, was applied in [5]. The relative area μ occupied by the chaotic component in the section is determined from the formula $\mu = n_{ch}/n$, where n_{ch} is the number of grid points corresponding to the chaotic trajectories and n is the number of all grid points accessible to the motion.

The second method is different from the first one in that not the final distances between the trajectories but the MLCEs are calculated on the same initial data grid. The MLCEs are calculated by the shadow-trajectory method. The MLCE distribution is constructed first. The chaotic and regular trajectories are separated as a result of the mode analysis of MLCE distribution (for details, see [5]), and the value $\mu = n_{ch}/n$ is calculated.

The third method is a "single trajectory" method. The surface of the phase-space section is divided into identical rectangular meshes. Then the initial data for a chaotic trajectory are specified at the section and the trajectory is integrated over a sufficiently long time interval. When integrating, the number of grid meshes intersected by the trajectory is tallied. The ratio of the number of these meshes to their total amount in the region accessible to motion gives the relative area of chaotic component. This method was first applied by B.V. Chirikov [12] in the analysis of the phase space of standard mapping.

The calculations by the first, second, and third methods were carried out on grids containing, respectively, 200×200, 50×50, and 400×400 meshes; the trajectories were integrated, respectively, on the time intervals $t = 10^3$, $t = 10^4$, and $t = 10^8$. In the latter case, there was a single trajectory, whereas in the first two cases the number of trajectories was equal to the number of grid meshes.

The areas $\tilde{\mu}$ calculated for the regular component by the three methods are shown in Fig. 6. One can see that the Hénon–Heiles method overestimates $\tilde{\mu}$ as compared to the MLCE distribution analysis and the single-trajectory method. The data obtained by the third method seem to be most accurate, because this method allows the finest phase-space subdivision. The energy dependence obtained by this method for the relative measure of the chaotic component is presented in Fig. 7.

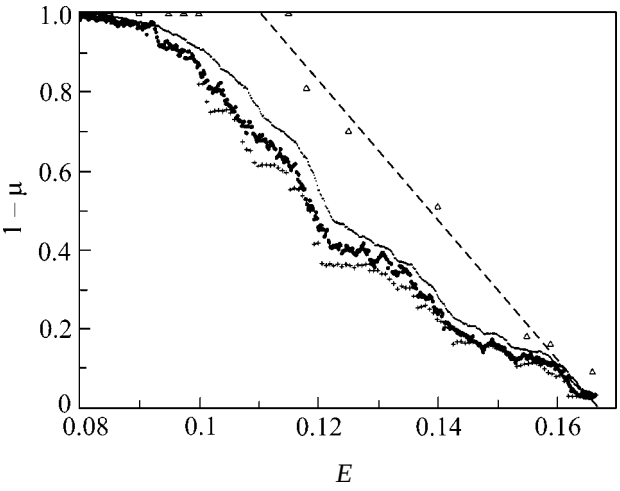

Fig. 6. Relative measure of the phase-space regular component of system (1) as a function of energy. The points correspond to the calculations by the first method, the circles are for the second method, and the crosses are for the third method. The data from [1] are drawn as triangles, and the linear approximation [4] to these data is shown by the dashed line.

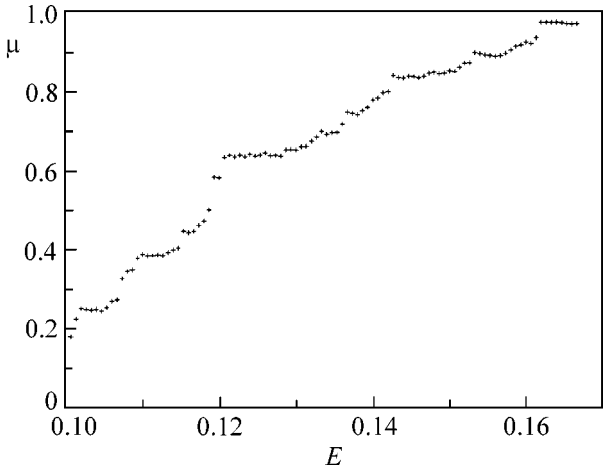

Fig. 7. Relative measure of the phase-space chaotic component of system (1) as a function of energy.

In Fig. 6, the data from [1] are additionally presented together with the linear approximating function $\tilde{\mu} = 1–17.6(E – 0.11)$ used, on the basis of these data, by Benettin *et al.* [4] in their calculations for $0.11 < E < 1/6$. These data strongly deviate from the real $\tilde{\mu}$ values (sometimes more than twofold).

Using the available numerical data on the MLCE and on the relative area of chaotic component, we can

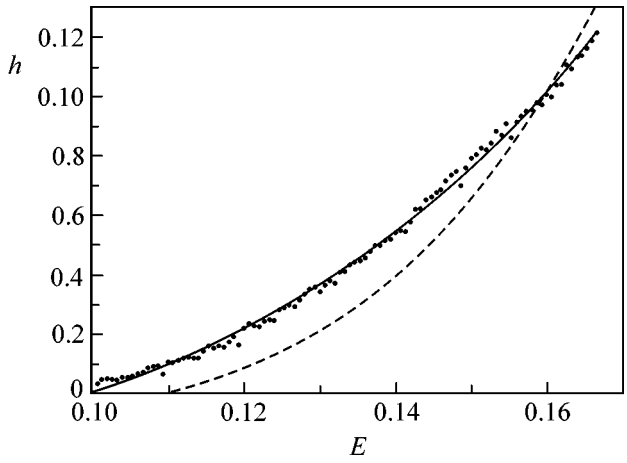

Fig. 8. Energy dependence of the dynamic entropy of system (1). Exponential approximation. The Benettin *et al.* dependence [4] is also shown (dashed line).

calculate the energy dependence of the dynamic entropy of the system. This dependence was obtained by Benettin *et al.* in [4]. According to [4], the dynamic entropy is calculated by the formula $h = L\mu$.

To calculate the dynamic entropy, we used the MLCE values calculated by the shadow-trajectory method with the maximal integration time interval $t = 10^7$ (the result virtually does not change for the HQR data). The values used for μ were obtained by the single-trajectory method, because they are most reliable. The resulting dependence and its exponential approximation $h = h_0 + A\exp(kE)$, with $h_0 = -0.046 \pm 0.003$, $A = 0.0067 \pm 0.0008$, and $k = 19.36 \pm 0.66$, is shown in Fig. 8. The parameters are given with their standard errors. The obtained dependence is also approximated well by the function $h = AE^k/(B^k + E^k)$, with $A = 0.190 \pm 0.006$, $B = 0.157 \pm 0.001$, and $k = 7.97 \pm 0.15$. The proximity of k to an integer number is noteworthy; i.e., we deal, in fact, with a rational function. The correlation coefficient is $R \approx 0.998$ for the exponential approximation and $R \approx 0.999$ is for the approximation by a rational function. In Fig. 8, the Benettin *et al.* [4] function $h = 0.060(E - 0.11)\exp(22E)$ is additionally presented for $0.11 < E < 1/6$. One can see that it describes the real dependence only at high E values.

In summary, the analysis of the energy dependence constructed for the MLCE of the Hénon–Heiles problem by two (shadow-trajectory and HQR) methods has shown that this dependence is not exponential and is close to a power law with an exponent of ≈ 3.6. For the generalized Hamiltonian (3) with $\varepsilon = 0.5$, 0.8, and 1.0, the dependences also obey a power law with nearly the same exponent. The energy dependence constructed in this work for the measure of chaotic component by three independent methods also refines, to a large degree, the hitherto accepted positions; the difference with the previous estimates of μ reaches 100% or greater. This dependence has discontinuities and is not described by a simple approximating function. Although the energy dependence of dynamic entropy, in agreement with [4], can be described by the exponential function, it can also be well and even better described by a rational function.

We are grateful to V.V. Kouprianov for discussions and consultations. This work was supported by the Russian Foundation for Basic Research, project no. 03-02-17356.

REFERENCES

1. M. Hénon and C. Heiles, Astron. J. **69**, 73 (1964).
2. A. J. Lichtenberg and M. A. Lieberman, *Regular and Stochastic Motion* (Springer, New York, 1982; Mir, Moscow, 1984).
3. M. Tabor, *Chaos and Integrability in Nonlinear Dynamics* (Wiley, New York, 1989; Éditorial URSS, Moscow, 2001).
4. G. Benettin, L. Galgani, and J.-M. Strelcyn, Phys. Rev. A **14**, 2338 (1976).
5. A. V. Mel'nikov and I. I. Shevchenko, Astron. Vestn. **32**, 548 (1998).
6. E. Hairer, S. P. Nørsett, and G. Wanner, *Solving Ordinary Differential Equations*, Vol. 1: *Nonstiff Problems* (Springer, Berlin, 1987; Mir, Moscow, 1990).
7. I. I. Shevchenko, Phys. Lett. A **241**, 53 (1998).
8. H. F. von Bremen, F. E. Udwadia, and W. Proskurowski, Physica D (Amsterdam) **101**, 1 (1997).
9. I. I. Shevchenko and V. V. Kouprianov, Astron. Astrophys. **394**, 663 (2002).
10. V. V. Kouprianov and I. I. Shevchenko, Astron. Astrophys. (2003) (in press).
11. I. King, *Introduction to Classical Stellar Dynamics* (Éditorial URSS, Moscow, 2002).
12. B. V. Chirikov, Phys. Rep. **52**, 263 (1979).

Translated by V. Sakun

JETP Letters, Vol. 77, No. 12, 2003, pp. 647–652. From Pis'ma v Zhurnal Éksperimental'noĭ i Teoreticheskoĭ Fiziki, Vol. 77, No. 12, 2003, pp. 778–783.

Trapping of Plasmons in Ion Holes¶

P. K. Shukla and B. Eliasson

Institut für Theoretische Physik IV, Ruhr-Universität Bochum, D-44780 Bochum, Germany

Received April 29, 2003; in final form, May 14, 2003

We present analytical and numerical studies of a new electron plasma wave interaction mechanism, which reveals trapping of Langmuir waves in ion holes associated with nonisothermal ion distribution functions. This Langmuir ion hole interaction is a unique kinetic phenomenon governed by two second nonlinear differential equations in which the Langmuir wave electric field and ion hole potential are coupled in a complex fashion. Numerical analyses of our nonlinearly coupled differential equations exhibit trapping of localized Langmuir wave envelops in the ion hole, which is either standing or moving with sub- or super ion thermal speed. The resulting ambipolar potential of the ion hole is essentially negative, giving rise to bipolar slow electric fields. The present investigation thus offers a new Langmuir wave contraction scenario that has not been rigorously explored in plasma physics. © *2003 MAIK "Nauka/Interperiodica".*

PACS numbers: 52.35.Hr

More than three decades ago, Hasegawa [1], Karpman [2, 3], and Zakharov [4] presented an elegant description of strong electromagnetic and Langmuir wave turbulence in which high-frequency photons and plasmons interact nonlinearly with low-frequency ion-acoustic waves via the ponderomotive force arising due to the spatial gradient of the high-frequency wave intensity. This nonlinear interaction is typically described by the two-fluid and Poisson–Maxwell equations, and the governing equations admit the localization of photon and plasmon wave packets, leading to the formation of envelope light and Langmuir wave solitons (also called cavitons) [5–8]. The latter are composed of electron/ion density depression, which traps photon and Langmuir wave envelops. Moreover, Yan'kov [9] studied the response of kinetic untrapped ions in the Langmuir envelope soliton theory and predicted the formation of sub ion thermal small-amplitude negative potential wells in plasmas. On the other hand, Mokhov and Chukbar [10] found a Langmuir envelope soliton accompanied by a small-amplitude negative potential well created by a localized Langmuir wave electric field in a quasineutral plasma with nonisothermal ions whose temperature is much smaller than the electron thermal temperature. In two and three dimensions, one encounters photon self-focusing, Langmuir wave collapse [4, 11]. The formation of cavitons has been observed in the ionosphere [12], as well as in several laboratory experiments [13–15].

In this letter, we present for the first time a new Langmuir turbulent state in the presence of ion phase-space vortices [16–19] that are associated with density holes and bipolar electric fields in collisionless plasmas. Ion phase-space vortices are natural products of ion-beam driven two-stream instabilities, and they play a very important role in laboratory experiments [20–22], as well as in the near-Earth plasma environment [23–25]. They are described by a wide class of Bernstein–Greene–Kruskal solutions to the Vlasov–Poisson equations. In the following, we show that nonlinearly coupled Langmuir waves and fully nonlinear ions holes admit a new class of solutions. Specifically, we demonstrate the existence of standing and sub ion thermal ion holes that trap Langmuir wave envelopes.

We consider an unmagnetized electron–ion plasma in the presence of Langmuir waves and large-amplitude ion holes. At equilibrium, we have $n_{e0} = n_{i0} = n_0$, where n_{j0} is the unperturbed number density of the particle species j (j equals e for electrons and i for ions). The Langmuir wave frequency is $\omega = (\omega_{pe}^2 + 3k^2 V_{Te}^2)^{1/2}$, where $\omega_{pe} = (4\pi n_e e^2/m_e)^{1/2}$ is the electron plasma frequency, n_e is the number density of electrons, e is the magnitude of the electron charge, m_e is the electron mass, k is the wavenumber, $V_{Te} = (T_e/m_e)^{1/2}$ is the electron thermal speed, and T_e is the electron temperature. Large-amplitude Langmuir waves interacting nonlinearly with ion holes generate a Langmuir wave envelope whose electric field E evolves slowly (in comparison with the electron plasma wave period) according to the nonlinear Schrödinger equation

$$2i\omega_p\left(\frac{\partial}{\partial t} + v_g\frac{\partial}{\partial x}\right)E + 3V_{Te}^2\frac{\partial^2 E}{dx^2} + \omega_p^2\left(1 - \frac{n_e}{n_0}\right)E = 0, \quad (1)$$

¶This article was submitted by the authors in English.

0021-3640/03/7712-0647$24.00 © 2003 MAIK "Nauka/Interperiodica"

where $\omega_p = (4\pi n_0 e^2/m_e)^{1/2}$ is the unperturbed electron plasma frequency and $v_g = 3kV_{Te}^2/\omega_p$ is the group velocity of the Langmuir waves. We note that (1) is derived by combining the electron continuity and momentum equations, as well as by using Poisson's equation with fixed ions, and by retaining the arbitrarily large electron number density variation n_e associated with ion holes in the presence of the Langmuir wave ponderomotive force. Assuming that the phase speed of ion holes is much smaller than the electron thermal speed, we readily obtain from the inertialess electron equation of motion the electron number density in the presence of the ponderomotive force of Langmuir waves. The result is

$$n_e = n_0 \exp[\tau(\phi - W^2)], \tag{2}$$

where $\tau = T_e/T_i$, T_i is the ion temperature, $\phi = e\varphi/T_i$, $W^2 = |E|^2/16\pi n_0 T_i$, and φ is the electrostatic potential of the ion hole. We note that the W term in Eq. (2) comes from the averaging of the nonlinear term $m_e \mathbf{v}_{he} \cdot \nabla \mathbf{v}_{he}$ over the Langmuir wave period $2\pi/\omega_{pe}$, where $\mathbf{v}_{he} \approx -\hat{\mathbf{x}}\, ieE/m_e\omega_{pe}$ is the electron quiver velocity in the Langmuir wave electric field.

If the potential has a maximum $\phi_{\max} > 0$, then there exist in general trapped ions where $\phi < \phi_{\max}$, while at the point where $\phi = \phi_{\max}$ there are no trapped ions. Similar to Schamel [16], we chose at this point a displaced Maxwellian distribution for the free ions. The ion distribution function associated with ion holes can then be obtained by solving the ion Vlasov equation for free and trapped ions, which have speeds larger and smaller than $[2(\phi_{\max} - \phi)]^{1/2}$, respectively. The electric potential will turn out to be essentially negative, with only a small-amplitude positive maximum $\phi_{\max}$ compared to the large-amplitude negative potential well with a minimum at $\phi_{\min} \equiv -\psi$. Thus, the potential is restricted by $-\psi \le \phi \le \phi_{\max}$, where ψ plays the role of the amplitude. Integrating the sum of the free and trapped ion distribution functions over velocity space, we obtain the ion number density [17]

$$n_i = n_0 b \exp\left(-\frac{M^2}{2}\right)\left[I(\phi_{\max} - \phi) + K\left(\frac{M^2}{2}, \phi_{\max} - \phi\right) + \frac{2}{\sqrt{\pi|\alpha|}} W_D\left(\sqrt{\alpha(\phi - \phi_{\max})}\right)\right], \tag{3}$$

where $M = V/V_{Ti}$ is the Mach number, V is the ion hole speed, $V_{Ti} = (T_i/m_i)^{1/2}$ is the ion thermal speed, m_i is the ion mass, and α is a (negative) parameter which determines the number of trapped ions. The normalization constant b is chosen so that when $\phi = 0$, the total density of ions is n_0. Furthermore, we have denoted [17] $I(x) = \exp(x)[1 - \mathrm{erf}(\sqrt{x})]$, $K(x, y) = (2/\sqrt{\pi})\int_0^{\pi/2} \sqrt{x}\cos\theta \exp(-y\tan^2\phi + x\cos^2\theta)\mathrm{erf}(\sqrt{x}\cos\theta)d\theta$, and the Dawson integral $W_D(x) = \exp(-x^2)\int_0^x \exp(t^2)\, dt$. A plateau in the resonant region is given by $\alpha = 0$, and $\alpha < 0$ corresponds to a vortexlike excavated trapped ion distribution. For positive α, we use [26] $W_D(ix) = i(\sqrt{\pi}/2)\exp(x^2)\mathrm{erf}(x)$ (where $i = \sqrt{-1}$) and replace the term $(2/\sqrt{\pi|\alpha|})W_D[\sqrt{\alpha(\phi - \phi_{\max})}]$ in Eq. (3) with $(1/\sqrt{\alpha})\exp[-\alpha(\phi - \phi_{\max})]\mathrm{erf}[\sqrt{-\alpha(\phi - \phi_{\max})}]$; we note especially that $M = 0$, $\alpha = 1$ leads to a Boltzmann distribution $n_i = n_0\exp(-\phi)$ for the ion density. The Langmuir wave ponderomotive force acting on ions is weaker by the electron to ion mass ratio in comparison with that acting on electrons, and, therefore, it is ignored in Eq. (3). The electron ponderomotive force is transmitted to ions via the ambipolar potential ϕ, which is determined from Poisson's equation

$$\tau\lambda_{De}^2 \frac{\partial^2\phi}{\partial x^2} = \frac{n_e}{n_0} - \frac{n_i}{n_0}, \tag{4}$$

where $\lambda_{De} = (T_e/4\pi n_0 e^2)^{1/2}$ is the electron Debye length.

We are interested in quasi-steady-state solutions of Eqs. (1)–(4), which are fully nonlinear. We insert $E(x, t) = W(\xi)\exp\{i[X(x) + T(t)]\}$ and $\phi(x) = \phi(\xi)$, where $\xi = x - Vt$ and $W(x)$, $X(x)$, $T(x)$ are assumed to be real, into Eqs. (1)–(4) and obtain the coupled set of the nonlinear equations

$$3\frac{\partial^2 W}{\partial\xi^2} - (\lambda - 1)W - W\exp[\tau(\phi - W^2)] = 0, \tag{5}$$

and

$$\tau\frac{\partial^2\phi}{\partial\xi^2} - \left(\exp[\tau(\phi - W^2)] + b\exp\left(-\frac{M^2}{2}\right)\right) \times \left[I\left(-(\phi - \phi_{\max}) + K\left(\frac{M^2}{2}, -(\phi - \phi_{\max})\right)\right.\right. + \left.\left.\frac{2}{\sqrt{\pi|\alpha|}} W_D\left(\sqrt{\alpha(\phi - \phi_{\max})}\right)\right] = 0, \tag{6}$$

where ξ is normalized by λ_{De} and $\lambda = 2\omega_p^{-1}(dT/dt) - 3k^2\lambda_{De}^2(1 - V^2/v_g^2)$ represents a nonlinear frequency shift. The system of Eqs. (5) and (6) admits the first integral in the form of a Hamiltonian

$$H(W, \phi, \lambda, M) = 3\left(\frac{\partial W}{\partial\xi}\right)^2 - \frac{\tau}{2}\left(\frac{\partial\phi}{\partial\xi}\right)^2$$

$$-(\lambda-1)W^2+\frac{1}{\tau}\{\exp[\tau(\phi-W^2)]-1\}$$
$$+b\exp\left(-\frac{M^2}{2}\right)[P(\phi_{\max}-\phi,\alpha)$$
$$+h\left(\frac{M^2}{2},0,\phi_{\max}-\phi\right)-1\Big]H_0=0, \quad (7)$$

where in the unperturbed state ($|\xi| = \infty$) we have used the boundary conditions $W = 0$, $\phi = 0$, $\partial W/\partial\xi = 0$, $\partial\phi/\partial\xi = 0$. The constant H_0 is chosen so that $H = 0$ at $|\xi| = \infty$. The auxiliary functions are defined as $P(x\,y) = I(x) + 2\sqrt{x/\pi}(1 - y^{-1}) + (2/y\sqrt{\pi|y|})W_D(\sqrt{-xy})$ and $h(x, a, b) = \int_a^b K(x, y)dy$.

Because we are interested in symmetric solutions defined by $W(\xi) = W(-\xi)$ and $\phi(\xi) = \phi(-\xi)$, the appropriate boundary conditions at $\xi = 0$ are $W = W_0$, $\phi = -\psi$, $\partial W/\partial\xi = 0$, and $\partial\phi/\partial\xi = 0$. Hence, from Eq. (7) we have

$$(\lambda-1)W_0^2-\frac{1}{\tau}\{\exp[\tau(-\psi-W_0^2)-1]\}$$
$$-b\exp\left(-\frac{M^2}{2}\right)\Big[P(\phi_{\max}+\psi,\alpha) \quad (8)$$
$$+h\left(\frac{M^2}{2},0,\phi_{\max}+\psi\right)-1\Big]-H_0=0,$$

which shows how the maximum values of W_0 and ψ are related to M, $\phi_{\max}$, and λ for given values of τ and α. A practical application of the Hamiltonian (7) is to check the correctness of any numerical scheme used to solve Eqs. (5) and (6), while Eq. (8) depicts the parameter regimes for the existence of trapped plasmons in ion holes.

In the absence of the Langmuir waves, ion holes are governed by the energy integral [27]

$$\frac{1}{2}\left(\frac{\partial\phi}{\partial\xi}\right)^2+\Psi(\phi,M)=0 \quad (9)$$

where the Sagdeev potential for our purposes with $\phi_{\max} = 0$ is [17]

$$\Psi(\phi,M)=-\frac{1}{\tau}\left\{\frac{1}{\tau}\{\exp[\tau\phi]-1\}+\exp\left(-\frac{M^2}{2}\right)\right.$$
$$\left.\times\left[P(-\phi,\alpha)+h\left(\frac{M^2}{2},0,-\phi\right)-1\right]\right\}. \quad (10)$$

Equation (9), which is obtained from Eq. (7) in the limit of vanishing Langmuir wave electric fields, determines the profile of ion holes. The latter exist provided that $\Psi(\phi)$ is negative between zero and $\pm\phi_0$. Multivalued solutions of $\Psi(0)$ are ensured provided that $\partial^2\Psi/\partial^2\phi =$ 0, while at $\phi = \phi_0(-\phi_0)$, we must have $\partial\Psi/\partial\phi > 0$ (<0). The condition $\Psi(\phi_0, M) = 0$ gives a relation between ϕ_0 and M for given values of α and τ. It turns out that ion holes without Langmuir waves have only a negative potential, as presumed earlier.

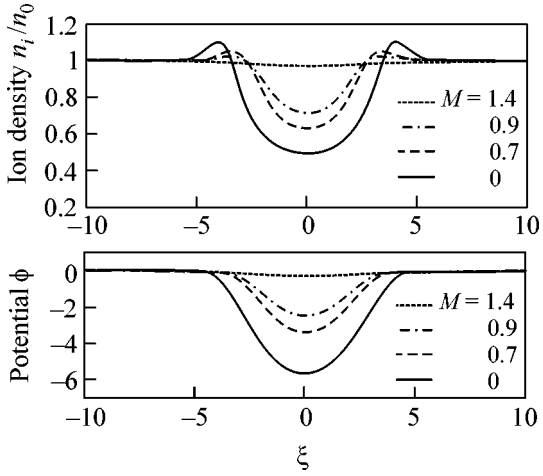

Fig. 1. Ion holes without Langmuir waves ($W = 0$) for different Mach numbers M with $\tau = 0.1$ and $\alpha = -1.0$.

We have carried out numerical studies of the equations governing ion holes with and without Langmuir waves for $\tau = 0.1$ and $\alpha = -1.0$. First, we consider small-amplitude Langmuir waves which are not strong enough to modify the ion hole but which can be linearly trapped in the density well of the hole. Accordingly, for $W^2 \ll 1$, Eq. (5) turns into a linear eigenvalue problem of the form $3(d^2W/d\xi^2) + [1 - \exp(\phi) - \lambda]W = 0$, with the eigenvalue λ and the corresponding eigenfunction W, and where ϕ is obtained by assuming $W = 0$ in the solution of Eq. (6) (see the numerical solution of Eq. (6) in the form of ion density profiles and the associated ambipolar potentials, respectively, in the upper and lower panels of Fig. 1). The eigenvalue problem will have a continuous spectrum for $\lambda < 0$, corresponding to "free particles" (in the language of quantum mechanics), and a point spectrum for $\lambda > 0$, corresponding to "trapped particles." We have numerically investigated the cases corresponding to four different Mach numbers displayed in Fig. 1 and found the corresponding positive eigenvalues listed in the second column of the table below, where each eigenvalue λ is associated with a bell-shaped eigenfunction W. Only one positive eigenvalue was found for each case, and thus these cases only admit the ground states for waves to be linearly trapped.

Next, we studied the presence of finite-amplitude Langmuir waves in the ion hole, in which the fully nonlinear system of equations (5) and (6) has to be solved numerically. The numerical solutions reveal that the ion hole deepened and widened, allowing the eigenvalue λ to be larger. We investigated the special case with a nonlinear shift of 0.1 of λ as listed in the fourth column

Table

Small amplitude problem		Finite amplitude problem	
M	λ	M	λ
1.4	0.0013	1.4	0.1013
0.9	0.0463	0.9	0.1463
0.7	0.0772	0.7	0.1772
0.0	0.1906	0.0	0.2906

in the table above and found solutions for all cases except for $M = 1.4$; the numerical solutions are depicted in Fig. 2. We can see from Figs. 1 and 2 that the presence of trapped finite-amplitude Langmuir waves makes the ion density depletion both deeper and wider, and the same holds for the ambipolar potential well. The deepening of the ambipolar negative potential well is a feature closely related to the strongly nonisothermal trapped ion distribution function. For this case, the electrostatic potential had small-amplitude maxima ϕ_{max} on the order of $\approx 10^{-3}$ on each side of the ion hole; this maximum of the potential increased with increasing M.

In order to investigate the conditions for existence of ion holes in the presence of strong Langmuir fields, we numerically solved Eq. (8) for ψ as a function of M (see Fig. 3). We used the same parameters $\tau = 0.1$ and $\alpha = -1.0$ as above. Here, we assumed the Langmuir field to be given as an external parameter (say, $W_0 = 0.8$) and with a nonlinear shift that follows $\lambda(M) = 0.3–0.14M$, as obtained approximately from the table above. This slightly overestimates the Langmuir field W_0 for small M and slightly underestimates the field for the highest M (see the upper panel in Fig. 2). We assumed a maximum potential of $\phi_{max} = 0.003$. We found that, for this set of parameters, the solution had an upper bound $M = 1.25$ for the existence of localized solutions, which is clearly smaller than the existence in the absence of the Langmuir fields. In a more exact mapping of the existence of ion holes, one needs more carefully to explore the relationships between different parameters in Eq. (8), possibly by solving system of equations (5) and (6) for different cases. Furthermore, the stability of the time-dependent system is not explored here but could be studied by direct simulations of the Vlasov–Poisson system.

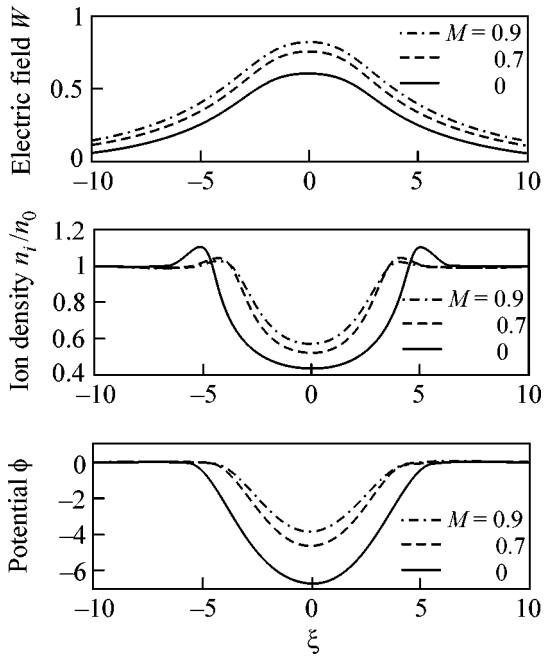

Fig. 2. Ion holes in the presence of Langmuir waves for different Mach numbers M with $\tau = 0.1$ and $\alpha = -1.0$.

It should be stressed that the properties of the present Langmuir envelope solitons significantly differ from those based on Zakharov's model [4], which utilizes the fluid ion response for driven (by the Langmuir wave ponderomotive force) ion-acoustic perturbations and yields subsonic density depression accompanied by a positive localized ambipolar potential structure. Furthermore, consideration of a Boltzmann ion density distribution, viz. $n_i = n_0\exp(-\phi)$, would correspond to the case $M = 0$ and $\alpha = 1$ in Eq. (6). Here, as shown in Fig. 4, we have a localized Langmuir wave electric field envelope trapped in a standing ion density cavity. The corresponding slow ambipolar potential is positive and localized.

In the numerical solutions of Eqs. (5) and (6), the second derivatives were approximated by a second-order centered difference scheme [28], and the values of W and ϕ were set to zero at the boundaries of the computational domain at $\xi = \pm 40$. The resulting nonlinear system of equations was solved iteratively. We used 2000 sampling points to resolve the solution.

In summary, we have presented the first analytical and numerical studies of a novel nonlinear plasma state in which the Langmuir waves interact with fully nonlinear ion holes. It is found that Langmuir waves have a dramatic effect on the ion hole in that the formation of envelope Langmuir solitons (Langmuir waves trapped in an ion hole) becomes an eigenvalue problem, and only discrete eigenstates are allowed. Self-trapped Langmuir waves in an ion hole are found to be either standing or moving with sub- or super ion thermal speed. An ion cavity loaded with Langmuir waves is typically wider and is accompanied by a negative localized ambipolar potential. Physically, the broadening of the ion hole and the enhancement of negative ambipolar potential occur because the ponderomotive force of the Langmuir waves locally expels electrons, which pull ions along to maintain the local charge neutrality. The deficit of ions in plasmas, in turn, produces more negative potential within the ion hole that is now widened

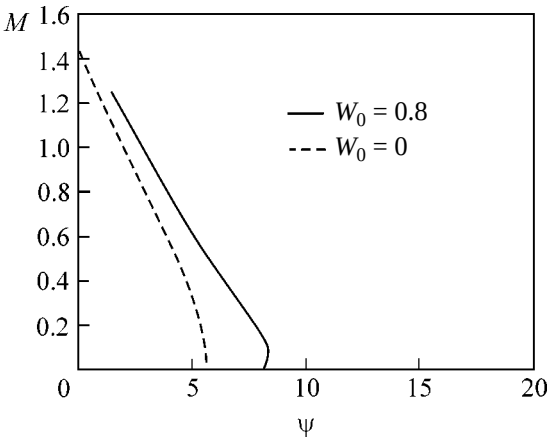

Fig. 3. Numerical solutions of Eq. (8), depicting $\psi(=-\phi_{min})$ vs. M for (dashed line) $W_0 = 0.0$ and (solid line) $W_0 = 0.8$, with $\lambda = 0.1$ and $\alpha = -1.0$. We see that the ion hole loaded with the Langmuir wave electric fields has an upper bound on the Mach number, which is smaller than that without the Langmuir wave fields.

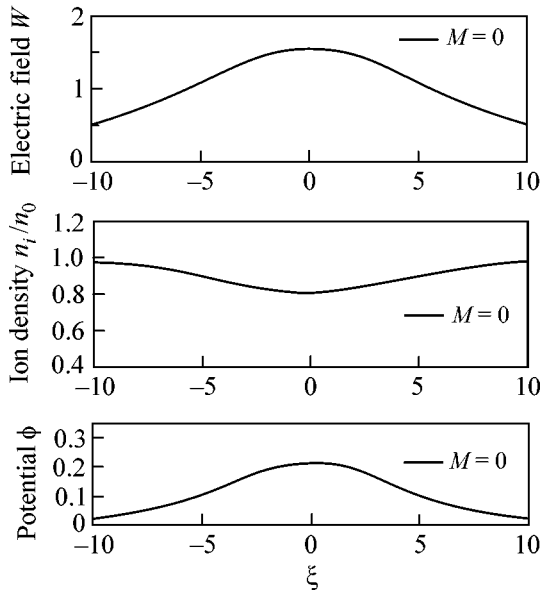

Fig. 4. A Langmuir caviton with a Boltzmann ion distribution for $M = 0$, $\lambda = 0.1$, $\tau = 0.1$, and $\alpha = 1.0$.

and enlarged to trap the localized Langmuir wave electric field envelope. Hence, the properties of the ion holes in the presence of Langmuir waves are significantly different from ion holes without the Langmuir waves, or cavitons involving the fluid [2, 3] or a Boltzmann ion response. In conclusion, we stress that the present localized structures are outside the realm of the two-fluid model, as they involve a trapped ion vortex state, which can be dealt with within the framework of a kinetic description only. We have thus solved one of the fundamental problems of nonlinear plasma physics, which has potential applications in space and laboratory plasmas that are driven by electron and ion beams.

This work was partially supported by the European Commission through contract no. HPRN-CT-2001-00314, as well as by the Deutsche Forschungsgemeinschaft through the Sonderforschungsbereich 591.

REFERENCES

1. A. Hasegawa, Phys. Rev. A **1**, 1746 (1970).
2. V. I. Karpman, Plasma Phys. **13**, 477 (1971); Phys. Scr. **11**, 263 (1975).
3. V. I. Karpman, *Nonlinear Waves in Dispersive Media* (Nauka, Moscow, 1973; Pergamon, Oxford, 1975).
4. V. E. Zakharov, Zh. Éksp. Teor. Fiz. **62**, 1745 (1972) [Sov. Phys. JETP **35**, 908 (1972)].
5. L. I. Rudakov, Dokl. Akad. Nauk SSSR **207**, 821 (1972) [Sov. Phys. Dokl. **17**, 1116 (1973)].
6. H. Schamel, M. Y. Yu, and P. K. Shukla, Phys. Fluids **20**, 1986 (1977); P. Deeskow, H. Schamel, N. N. Rao, *et al.*, Phys. Fluids **30**, 2703 (1987).
7. R. K. Varma and N. N. Rao, Phys. Lett. A **79**, 311 (1980).
8. N. N. Rao and R. K. Varma, J. Plasma Phys. **27**, 95 (1982).
9. V. V. Yan'kov, Pis'ma Zh. Éksp. Teor. Fiz. **29**, 179 (1979) [JETP Lett. **29**, 160 (1979)].
10. Yu. V. Mokhov and K. V. Chukbar, Fiz. Plazmy (Moscow) **10**, 206 (1984) [Sov. J. Plasma Phys. **10**, 122 (1984)].
11. V. D. Shapiro and V. I. Shevchenko, in *Handbook of Plasma Physics* (North-Holland, Amsterdam, 1984), Vol. 2, p. 8; M. V. Goldman, Rev. Mod. Phys. **56**, 709 (1984).
12. H. C. Wong, R. Stenzel, and A. Y. Wong, Phys. Rev. Lett. **33**, 886 (1974).
13. A. Y. Wong and B. H. Quon, Phys. Rev. Lett. **34**, 1499 (1975).
14. H. Ikezi, R. P. H. Chang, and R. A. Stern, Phys. Rev. Lett. **36**, 1047 (1976).
15. T. Intrator, C. Chan, N. Hershkowitz, and D. Diebold, Phys. Rev. Lett. **53**, 1233 (1984).
16. H. Schamel, Plasma Phys. **13**, 491 (1971); Phys. Rep. **140**, 161 (1986).
17. S. Bujarbarua and H. Schamel, J. Plasma Phys. **25**, 515 (1981).
18. F. Skiff, G. Bachet, and F. Doveil, Phys. Plasmas **8**, 3139 (2001).
19. L. K. S. Daldorff, P. Guio, S. Börve, *et al.*, Europhys. Lett. **54**, 161 (2001).
20. H. L. Pécseli, R. I. Armstrong, and J. Trulsen, Phys. Lett. A **81**, 386 (1981); H. L. Pécseli *et al.*, Phys. Scr. **29**, 241 (1984); H. L. Pécseli, Laser Part. Beams **5**, 211 (1987).

21. G. Bachert, F. N. Skiff, M. Dindelegan, *et al.*, Phys. Rev. Lett. **80**, 3260 (1998).

22. Y. Nakamura, H. Bailung, and P. K. Shukla, Phys. Rev. Lett. **83**, 1602 (1999); C. Franck, T. Klinger, A. Piel, and H. Schamel, Phys. Plasmas **8**, 4271 (2001).

23. J. Dombeck, C. Cattell, J. Crumley, *et al.*, J. Geophys. Res. **106**, 19013 (2001).

24. C. Cattell *et al.*, Geophys. Res. Lett. **29**, 9 (2002); J. P. McFadden *et al.*, J. Geophys. Res. **108** (A4), 8018 (2003).

25. P. Guio, S. Börve, L. K. S. Daldorff, *et al*., Nonlinear Proc. Geophys. **10**, 75 (2003).

26. *Handbook of Mathematical Functions*, Ed. by M. Abramowitz and I. A. Stegun, 2nd ed. (Dover, New York, 1972; Nauka, Moscow, 1979).

27. R. Z. Sagdeev, in *Reviews of Plasma Physics*, Ed. by M. A. Leontovich (Consultants Bureau, New York, 1966), Vol. 4, p. 23; R. Z. Sagdeev, Rev. Mod. Phys. **51**, 11 (1979).

28. E. Isaacson and H. B. Keller, *Analysis of Numerical Methods* (Dover, New York, 1994).

JETP Letters, Vol. 77, No. 12, 2003, pp. 653–656. Translated from Pis'ma v Zhurnal Éksperimental'noĭ i Teoreticheskoĭ Fiziki, Vol. 77, No. 12, 2003, pp. 784–787.

Cyclotron Mechanism of Electron Acceleration in Subpicosecond Laser Plasma

V. S. Belyaev[1], O. F. Kostenko[1]*, and V. S. Lisitsa[2]

[1] *Central Research Institute of Machine Building, Korolev, Moscow region, 141070 Russia*

**e-mail: olegkostenko@mtu-net.ru*

[2] *Institute of Nuclear Fusion, Russian Research Centre Kurchatov Institute, pl. Akademika Kurchatova 1, Moscow, 123182 Russia*

Received May 28, 2003

The effect of ultrastrong magnetic fields generated in a relativistic-intensity subpicosecond laser plasma on the acceleration of fast electrons was studied. It is shown that resonance electrons can continuously accumulate energy from the circularly polarized laser field in the presence of a longitudinal magnetic field. For the linear polarization and a transverse magnetic field, energy accumulation has a pulse-periodic character, and the electron trajectories correspond to electron rotation in the Larmor orbit in a quasi-stationary magnetic field, while the energy strongly oscillates. In both cases, electron energy may attain values higher than 100 MeV for intensities of 10^{20} W/cm^2. © *2003 MAIK "Nauka/Interperiodica".*

PACS numbers: 52.38.Kd; 52.27.Ny

In the interaction of subpicosecond laser petawatt pulses with solid targets, a high-energy component with an energy of up to ~100 MeV was observed in the spectrum of electrons generated at laser intensities higher than 10^{20} W/cm^2 [1, 2]. The possibility of accelerating electrons in the laser electromagnetic field to energies exceeding, by an order of magnitude, their oscillation energy was confirmed by the numerical PIC calculations [2]. Mechanisms such as electron acceleration in the wake-wave field and electron betatron resonance in a quasistatic electric and magnetic fields of a plasma channel are also discussed (see, e.g., review [3]).

It is shown in this work that electrons can be accelerated by a laser wave to energies higher than 100 MeV in a subpicosecond laser plasma under conditions where the electron cyclotron frequency

$$\omega_c = e_0 B_s / mc \tag{1}$$

in a quasistatic magnetic field B_s is on the order of the laser frequency ω. The scale of the required magnetic fields is given by

$$B_0 = mc\omega/e_0,$$

because

$$\omega_c/\omega = B_s/B_0.$$

For the laser wavelength $\lambda = 1.05$ μm, one has $B_0 = 107$ MG. Magnetic fields in the range 340–460 MG have already been observed in the dense plasma region in the course of interaction of a laser pulse of a duration of 0.7–1 ps and intensity $I \approx 10^{20}$ W/cm^2 with a solid target [4].

Our analysis is based on the equations of motion for an electron in a laser field and a constant magnetic field, because electron collisions can be neglected at relativistic energies. Circularly and linearly polarized laser waves are considered. The direction of the magnetic field corresponds to different mechanisms of its generation.

1. Autoresonance in a circularly polarized laser field. Magnetic-field generation by the interaction of a subpicosecond circularly polarized laser pulse of relativistic intensity with dense-plasma electrons was considered theoretically in [5] for the electron below-critical density. It follows from [5] that, if a laser pulse of relativistic intensity $I \geq 10^{20}$ W/cm^2 propagates in the self-channeling regime with electron expulsion from the channel, a uniform magnetic field with an induction of higher than 100 MG is generated in the central region of the beam. For right-hand polarization of the laser wave, the direction of a quasistatic magnetic field coincides with the direction of its wave vector.

The covariant equation of motion for an electron in the channel has the form

$$m\frac{du^\mu}{d\tau} = \frac{e}{c}F^{\mu\nu}u_\nu. \tag{2}$$

Here, u^μ is the 4-velocity and τ is the "intrinsic" time ($e = -e_0$ is the electron charge). The electromagnetic field tensor is

$$F^{\mu\nu} = B_s(e_2^\mu e_1^\nu - e_1^\mu e_2^\nu) - \frac{mc^2}{e}\xi(f_1^{\mu\nu}\cos\varphi + f_2^{\mu\nu}\sin\varphi), \tag{3}$$

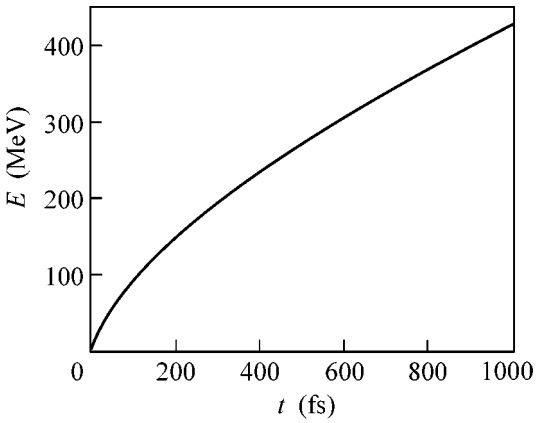

Fig. 1. Energy of a resonance electron in the circularly polarized laser wave with an intensity of 10^{20} W/cm^2 in a longitudinal magnetic field.

where $\varphi = k^\mu x_\mu$ is the wave phase, $k^\mu = (\omega/c)n^\mu$ is the wave 4-vector, and $f_s^{\mu\nu} = k^\mu e_s^\nu - e_s^\mu k^\nu$ ($e_\alpha^\mu = (0, \mathbf{i}_\alpha)$, $n^\mu = (1, \mathbf{i}_3)$ are linearly independent 4-vectors and $\mathbf{i}_\alpha$ are three-dimensional unit vectors of the coordinate system). The tensor $F^{\mu\nu}$ corresponds to a constant magnetic field $\mathbf{B}_s = B_s\mathbf{i}_3$ and the electromagnetic wave with right-hand circular polarization

$$\mathbf{E}_l = \frac{mc\omega}{e}\xi[\mathbf{i}_1\cos\omega(t - z/c) + \mathbf{i}_2\sin\omega(t - z/c)], \quad \mathbf{B}_l = [\mathbf{i}_3 \times \mathbf{E}_l]. \tag{4}$$

Equation (2) has the integral of motion $d\varphi/d\tau = \text{const}$, which relates the electron energy $E = mc^2\gamma$ to the electron longitudinal momentum p_z:

$$dp_z = dE/c. \tag{5}$$

Using this integral, Eq. (2) can be solved analytically [6]. From the solution, it follows that the energy of electrons, whose initial velocity satisfies the cyclotron autoresonance condition

$$\gamma_0\left(1 - \frac{v_{0z}}{c}\right) = \frac{\omega_c}{\omega}, \tag{6}$$

increases with time t. This can be expressed in the parametric form as

$$\gamma = \gamma_0 + k\tau^2, \quad t = \gamma_0\tau + \frac{k\tau^3}{3}. \tag{7}$$

The coefficient k depends on the ratio ω_c/ω and laser intensity I:

$$k = \frac{\omega\omega_c\xi^2}{2} = \frac{2\pi e^2}{m^2c^3}\frac{\omega_c}{\omega}I. \tag{8}$$

The dependence (7) can be approximated by the expression

$$\gamma = (9kt^2)^{1/3} - \gamma_0 \tag{9}$$

for $I > 10^{19}$ W/cm^2, $t > 100$ fs, and initial electron energy $E_0 = mc^2\gamma_0 < 5$ MeV. This leads to the scaling law $E \propto I^{1/3}$.

The dependence $E(t)$ (7) for an initially nonrelativistic electron, $\omega_c = \omega$, and $I = 10^{20}$ W/cm^2 is shown in Fig. 1. In estimates, we assume that the acceleration time is determined by the diffraction length $L_z \approx \pi r_0^2/\lambda$. For the focal radius $r_0 \approx 5$ μm and wavelength $\lambda = 1$ μm [4], one has $L_z \approx 80$ μm. In the self-channeling regime, this value can be an order of magnitude larger. The electron trajectory in the relativistic regime is determined from the equations

$$\frac{dx}{d\tau} = c\xi\omega\tau\cos\omega\tau, \quad \frac{dy}{d\tau} = c\xi\omega\tau\sin\omega\tau, \quad \frac{dz}{d\tau} = \frac{c}{2}\xi^2\omega^2\tau^2. \tag{10}$$

From Eqs. (7) and (10) it follows that the electron acquires an energy of 175 MeV during 260 fs on the length L_z. The transverse radius of the orbit does not exceed 6 μm, which corresponds to the focus size.

As the electron energy increases in the electric field of the laser wave, the longitudinal electron momentum (5) increases due to the action of the wave magnetic field. Since $p_z = Ev_z/c^2$, the time dependence of the longitudinal velocity is given by the expression

$$v_z = c(1 - mc^2/E(t)).$$

For the intensity considered, an electron acquires relativistic energy in a time interval shorter than the period of laser radiation and moves in the longitudinal direction with a velocity close to the velocity of light. It follows from Eqs. (10) that the electron leaves the acceleration region at an angle

$$v = 2/\xi\omega\tau \approx 8 \times 10^{-2} \text{ rad}$$

to the axis of the laser beam.

It is of interest to estimate the synchrotron radiation loss for the accelerated ultrarelativistic electron moving in an ultrastrong magnetic field. The radiation energy-loss rate for a charged particle is given by the formula [7]

$$P = -\frac{2e^2}{3c^3}\left(\frac{du}{d\tau}\right)^2.$$

With allowance for the τ dependence of the 4-velocity (7) and (10), one gets

$$P = \frac{2e^2\xi^2\omega^2}{3c}(1 + \omega^2\tau^2).$$

It follows that the integrated losses during the acceleration time are ~1 keV. The ratio of the lost and acquired power increases with time but is still rather small:

$$\frac{P}{(dE/dt)} \approx 2 \times 10^{-5},$$

justifying the neglect of the radiation reaction force in equation of motion (2).

2. Electron acceleration by a linearly polarized laser wave in the presence of a transverse magnetic field. Among the possible mechanisms of generating quasistatic magnetic fields by the interaction of an ultrastrong subpicosecond laser pulse with a solid target, there is a Weibel instability that appears due to the anisotropic velocity distribution of photoelectrons formed upon the over-barrier ionization of atomic ions [8]. According to [8], the magnetic field in the dense plasma region rapidly increases to reach $B_s \approx 70$ MG in a time on the order of the laser period for a linearly polarized laser radiation at a wavelength of 1 μm with an intensity of 10^{19} W/cm^2. The resulting quasistatic magnetic field is parallel to the magnetic field of the laser wave.

In this case, the electromagnetic field tensor has the form

$$F^{\mu\nu} = B_s(e_1^\mu e_3^\nu - e_3^\mu e_1^\nu) - \frac{mc^2}{e}\xi f_1^{\mu\nu}\cos\varphi.$$

It corresponds to a constant magnetic field $\mathbf{B}_s = B_s\mathbf{i}_2$ and a linearly polarized electromagnetic wave

$$\mathbf{E}_l = \frac{mc\omega}{e}\xi\mathbf{i}_1\cos\varphi, \quad \mathbf{B}_l = \frac{mc\omega}{e}\xi\mathbf{i}_2\cos\varphi.$$

The solution to equation of motion (2) can be represented in the form of a combination of the linearly independent 4-vectors

$$u^\mu = u_1 e_1^\mu + u_2 e_2^\mu + l_3 n^\mu + l_4 \bar{n}^\mu,$$

where $\bar{n}^\mu = (1, -\mathbf{i}_3)$. The resulting nonlinear system of differential equations is

$$\frac{du_1}{d\tau} = -\Omega l_3 + \Omega l_4 + 2\omega\xi l_4\cos\varphi,$$

$$\frac{dl_4}{d\tau} = -\frac{\Omega}{2}u_1, \quad \frac{d\varphi}{d\tau} = \frac{2\omega}{c}l_4, \quad \frac{dt}{d\tau} = \frac{1}{c}(l_3 + l_4), \quad (11)$$

$$4l_3 l_4 = c^2 + u_1^2 + u_2^2, \quad \Omega = \frac{eB_s}{mc}.$$

In this case, $du_2/dt = 0$; i.e., the electron motion along the magnetic field proceeds with a constant velocity and does not affect the motion in the perpendicular plane. In the limiting cases $\Omega = 0$ and $\xi = 0$, the system of Eqs. (11) gives the proper analytic expressions for the electron motions in the field of a linearly polarized wave and in a uniform magnetic field, respectively.

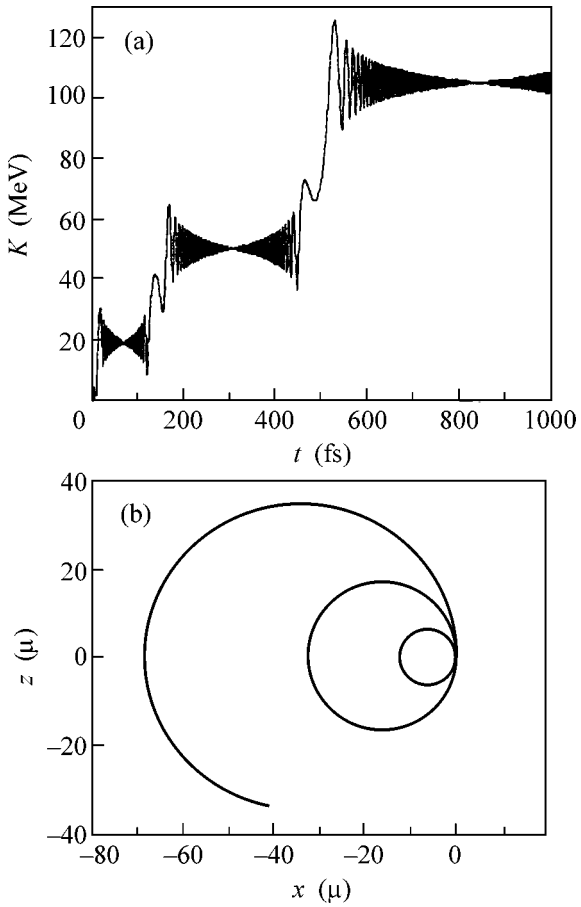

Fig. 2. (a) Electron kinetic energy and (b) trajectory in a linearly polarized laser wave with $\Omega = \omega$ and an intensity of 10^{20} W/cm^2 in a transverse magnetic field.

In the general case, this system of equations can be solved only numerically. In the calculations, the energy $K(t) = mc^2(dt/d\tau - 1)$ acquired by an electron during a laser pulse of duration 1 ps was determined. It was assumed for definiteness that the initial electron velocity was zero and that the laser wavelength was $\lambda = 1.05$ μm. The solution showed strong oscillations (Fig. 2a), and its validity was checked by comparison with the solutions by three methods: the Bulirsch–Stoer method for smooth solutions, the variable-step Runge–Kutta method, and the Stiff method for rigid systems.

It is seen from Fig. 2a that an electron undergoes impulsive transitions between "levels" with certain mean energies. Analysis of the time dependence of the electron velocity for relativistic intensities and different values of Ω indicates that this mean energy corresponds to the electron motion in a constant magnetic field B_s in a circular orbit with the relativistic Larmor frequency $|\Omega|/\gamma$ and velocity close to c. The energy oscillations reach a minimum when the electron velocity is in opposition to the wave vector, because the phase of the electromagnetic wave in the electron trajectory changes most rapidly in this case. When the electron velocity is

aligned with the wave vector, the phase changes relatively slowly. If, simultaneously, the electron is brought into the acceleration phase where the projections of its velocity onto the longitudinal and transverse directions are aligned with the corresponding projections of electromagnetic force, it acquires a portion of energy and moves to a new circular orbit with large radius (Fig. 2b). In the general case, an electron can acquire or lose a considerable portion of energy, on the order of several tens of MeV, in a time interval shorter than the Larmor period. During the time of quasistationary phase, an electron can either acquire or lose almost the same energy portions, so that its energy changes only slightly.

Interestingly, the electron trajectory is determined by the constant magnetic field, although it is an order of magnitude lower than the electric field of the laser wave. According to [9], this occurs if the condition $B_s\gamma^2 \gg E_l$ is fulfilled for the relativistic electron energies. The perturbative analysis of the electron acceleration mechanism at nonrelativistic intensities in a transverse magnetic field is presented in works [9] and [10]. According to the classification of the latter work, the impulsive electron-energy changes correspond to the scattering from the resonance.

The above mechanism accounts for the electron acceleration in the case where Ω deviates appreciably from ω. For instance, if $\Omega = 0.05\omega$ and intensity $I = 10^{20}$ W/cm^2, the electron energy attains 170 MeV in 350 fs. The corresponding transverse size of the acceleration region is 8 μm, and the longitudinal size is 100 μm. If $\Omega = \omega$ and the wave magnetic field is aligned with the constant magnetic field at zero time, the electron energy reaches ~105 MeV in ~530 fs (Fig. 2a). It is only required that the focus diameter exceed the diameter (33 μm) of the preceding orbit. The oscillations of electron energy and the dependence of their dynamics on the initial conditions provide continuous energies, with which electrons leave the focal region.

In summary, ultrastrong magnetic fields generated in dense laser plasma at relativistic intensities have a deciding action on the trajectory of an accelerated electron. In a circularly polarized laser field and in a longitudinal magnetic field, resonance electrons can continuously accumulate energy. If the resonance electrons uniformly occupy the focal region, more than 50% of them accumulate an energy higher than 100 MeV at an intensity of 10^{20} W/cm^2 and move forward at an angle less than 0.1 rad. For the linear polarization and transverse magnetic field, energy is acquired in the impulse–periodic character. The mean electron trajectory corresponds to the rotation in the Larmor orbit in a quasistationary magnetic field, and energy strongly oscillates. For the indicated intensity, the upper bound for the electron spectrum can also exceed 100 MeV.

We are grateful to V.P. Kraĭnov for discussions.

This work was supported by the ISTC, project no. 2155.

REFERENCES

1. T. E. Cowan, M. D. Perry, M. H. Key, *et al.*, Laser Part. Beams **17**, 773 (1999).
2. T. E. Cowan, A. W. Hunt, T. W. Phillips, *et al.*, Phys. Rev. Lett. **84**, 903 (2000).
3. A. Pukhov, Rep. Prog. Phys. **66**, 47 (2003).
4. M. Tatarakis, A. Gopal, I. Watts, *et al.*, Phys. Plasmas **9**, 2244 (2002).
5. V. I. Berezhiani, S. M. Mahajan, and N. L. Shatashvili, Phys. Rev. E **55**, 995 (1997).
6. Yu. G. Pavlenko, *Lectures on Theoretical Mechanics* (Mosk. Gos. Univ., Moscow, 1991).
7. Ya. P. Terletskiĭ and Yu. P. Rybakov, *Electrodynamics*, 2nd ed. (Vysshaya Shkola, Moscow, 1990).
8. V. P. Kraĭnov, JETP **96**, 430 (2003).
9. M. V. Fedorov, *Electron in a Strong Light Field* (Nauka, Moscow, 1991).
10. A. P. Itin, Fiz. Plazmy (Moscow) **28**, 639 (2002) [Plasma Phys. Rep. **28**, 592 (2002)].

Translated by V. Sakun

JETP Letters, Vol. 77, No. 12, 2003, pp. 657–661. From Pis'ma v Zhurnal Éksperimental'noĭ i Teoreticheskoĭ Fiziki, Vol. 77, No. 12, 2003, pp. 788–793.

Variational Principle in Canonical Variables, Weber Transformation, and Complete Set of the Local Integrals of Motion for Dissipation-Free Magnetohydrodynamics¶

A. V. Kats

Usikov Institute for Radiophysics and Electronics, National Academy of Sciences of Ukraine, Kharkov, 61085 Ukraine
e-mail: avkats@akfirst.kharkiv.com, avkats@ire.kharkov.ua

Received May 28, 2003

The intriguing problem of the "missing" MHD integrals of motion is solved in this paper; i.e., analogues of the Ertel, helicity, and vorticity invariants are obtained. The two latter have been discussed earlier in the literature only for specific cases, and the Ertel invariant is presented for the first time. The set of ideal MHD invariants obtained appears to be complete: to each hydrodynamic invariant corresponds its MHD generalization. These additional invariants are found by means of the fluid velocity decomposition based on its representation in terms of generalized potentials. This representation follows from the discussed variational principle in Hamiltonian (canonical) variables, and it naturally decomposes the velocity field into the sum of "hydrodynamic" and "magnetic" parts. The "missing" local invariants are expressed in terms of the "hydrodynamic" part of the velocity and therefore depend on the (nonunique) velocity decomposition; i.e., they are gauge-dependent. Nevertheless, the corresponding conserved integral quantities can be made decomposition-independent by the appropriate choice of the initial conditions for the generalized potentials. It is also shown that the Weber transformation of MHD equations (partial integration of the MHD equations) leads to the velocity representation coinciding with that following from the variational principle with constraints. The necessity of exploiting the complete form of the velocity representation in order to deal with general-type MHD flows (nonbarotropic, rotational, and with all possible types of breaks as well) in terms of single-valued potentials is also under discussion. The new basic invariants found allow one to widen the set of the local invariants on the basis of the well-known recursion procedure. © *2003 MAIK "Nauka/Interperiodica".*

PACS numbers: 47.65.+a; 47.10.+g

The fact that in dissipation-free hydrodynamics there exist vorticity, helicity, and Ertel invariants makes it evident that corresponding analogues have to exist for the ideal MHD as well. But in spite of the fact that for the dissipation-free MHD flows there exist additional topological invariants, namely, magnetic helicity and cross-helicity, introduced by Moffatt [1], the analogues of the vorticity and helicity invariants have not yet been discussed with the necessary completeness (cf., for instance, the recent review [2]). Related quantities were mentioned for the specific cases of symmetric flows in [3–5], while the vorticity and helicity invariants for incompressible flows were obtained in [6, 7]. A complete discussion of the generalized vorticity and helicity invariants for the compressible MHD flows without any restrictions relating to the flow symmetry and an introduction of the generalized Ertel invariant will be presented below (see also [8]). Note here that these generalized invariants cannot be expressed in terms of the conventional Euler variables (the velocity, pressure, entropy, magnetic field, etc.)—their definition involves the specific decomposition of the velocity, which is natural in terms of the Weber transformation (or in terms of the Clebsch representation) and involves subsidiary fields. Suppose this fact was the main obstacle in their derivation. The necessary subsidiary fields are related to the specific symmetry of the MHD equations. This symmetry is naturally expressed in terms of the Lagrange variables labeling the fluid particles: the corresponding symmetry group consists in relabeling (cf. [2] and references therein). In the Hamiltonian approach, these Lagrange labels are generalized coordinates, and the velocity field is expressed in terms of their gradients multiplied by conjugate momenta constituting a Clebsch-type representation (cf. [9] and [2, 10]).

For the MHD case, the velocity representation includes an additional term proportional to the magnetic field originally introduced in [11]. Below, we use a representation that decomposes the velocity field into two parts, say, a "hydrodynamic" one, which coincides with the velocity representation for the hydrodynamics, and a "magnetic" part (the latter vanishes identically for zero magnetic field). The generalized integrals of motion are then expressed using the hydrodynamic part of the velocity representation. Such decomposition of the velocity is not unique, and the corresponding inte-

¶ This article was submitted by the author in English.

grals of motion undergo some changes caused by the change in the generalized potentials (gauge transformations). We show that such changes can be eliminated by an appropriate choice of the initial conditions for the generalized potentials.

As it may seem, the velocity representation following from the variational principle is somewhat artificial; we prove its equivalence to that obtained from the generalization of the Weber transformation (cf. [12, 13]) for the compressible nonbarotropic MHD flows (for the incompressible flows, this was done in [6]; for the barotropic case, see [14]).

Based on the additional invariants found, it is possible to derive a wide set of new invariants resulting from the recursion relations (cf. [15, 16]; see also [2, 10]). These sets of invariants are briefly discussed in the paper as well.

Let us start with the MHD equations in the Hamiltonian form. The dissipation-free MHD flows can be described in terms of the canonical variables (cf., for instance, [2]). Here we need the more complete set of the canonical variables enabling one to describe general-type flows. An example of such an approach, allowing us to deal with discontinuous motion as well, is presented in [8, 17]. For our case, the appropriate Hamiltonian density $\mathcal{H}$ can be chosen in the form

$$\mathcal{H}(\mathcal{P}, \mathcal{Q}, \nabla\mathcal{Q}) = \frac{\rho\mathbf{v}^2}{2} + \rho\varepsilon + \frac{(\mathrm{curl}\mathbf{A})^2}{8\pi} + (\mathbf{M}\cdot\nabla\Lambda), \quad (1)$$

where ρ, ε, and s denote density, internal energy, and entropy, respectively; $\mathbf{A}$ is the vector potential; and $\mathbf{H} = \mathrm{curl}\mathbf{A}$.[1] The velocity field $\mathbf{v}$ is expressed in terms of the generalized coordinates, $\mathcal{Q} = (Q, \mathbf{M})$, and conjugate momenta, $\mathcal{P} = (P, \mathbf{A})$

$$Q = (\varphi, \boldsymbol{\mu}, s), \quad P = (\rho, \boldsymbol{\lambda}, \sigma), \quad (2)$$

$$\mathbf{v} = \mathbf{v}(\mathcal{P}, \mathcal{Q}) \equiv \mathbf{v}_h + \mathbf{v}_M, \quad \mathbf{v}_h = -\rho^{-1}P\nabla Q, \quad \mathbf{v}_M = -\rho^{-1}[\mathbf{H}\times\mathbf{M}]. \quad (3)$$

Here, subindexes h and M correspond to the "hydrodynamic" and "magnetic" parts of the velocity field. The hydrodynamic part, $\mathbf{v}_h$, corresponds to the generalized Clebsch representation for the conventional hydrodynamics (compare, for instance, papers [17–19]), and the magnetic part, $\mathbf{v}_M$, coincides with the conventional MHD term if we replace the divergence-free field $\mathbf{M}$ by $\mathrm{curl}\mathbf{S}$. The latter was first introduced by Zakharov and Kuznetsov (cf. [11]).

[1] The action differs slightly from that proposed in [17]. The main difference consists in introducing the vector potential for the magnetic field. Therefore, the canonical pair is $\mathbf{A}$, $\mathbf{M}$ instead of $\mathbf{H}$, $\mathbf{S}$, where $\mathbf{S} = \mathrm{curl}\mathbf{M}$. We do not deal with the discontinuous flows and omit the surface term in the action.

The set of canonical equations

$$\dot{\mathcal{Q}} = \delta\mathcal{H}/\delta\mathcal{P}, \quad \dot{\mathcal{P}} = -\delta\mathcal{H}/\delta\mathcal{Q}, \quad (4)$$

or, in explicit form,

$$\dot{\rho} + \mathrm{div}(\rho\mathbf{v}) = 0, \quad D\varphi = w - v^2/2, \quad (5)$$

$$D\boldsymbol{\mu} = 0, \quad \dot{\lambda}_m + \mathrm{div}(\lambda_m\mathbf{v}) = 0, \quad (6)$$

$$Ds = 0, \quad \dot{\sigma} + \mathrm{div}(\sigma\mathbf{v}) = -\rho T, \quad (7)$$

$$\dot{\mathbf{A}} = [\mathbf{v}\times\mathrm{curl}\mathbf{A}] - \nabla\Lambda, \quad \dot{\mathbf{M}} = \frac{\mathrm{curl}\mathbf{H}}{4\pi} + \mathrm{curl}[\mathbf{v}\times\mathbf{M}], \quad (8)$$

includes mass conservation, entropy transport, and magnetic field dynamic equations. Here, w and T are the enthalpy and temperature, dot denotes time derivative, and $D \equiv \partial_t + (\mathbf{v}\cdot\nabla)$ is the substantial (material) derivative.

From the velocity representation (Eq. (3) and Eqs. (5)–(8)), it strictly follows that the velocity field satisfies the Euler equation with the magnetic force taken into account,

$$\rho D\mathbf{v} = -\nabla p + (4\pi)^{-1}[\mathrm{curl}\mathbf{H}\times\mathbf{H}], \quad (9)$$

where p is the fluid pressure.

Note here that variation of the action

$$\mathcal{A} = \int dt\int d\mathbf{r}(\mathcal{P}\partial_t\mathcal{Q} - \mathcal{H}) \quad (10)$$

with respect to Λ leads to the divergence-free condition for the subsidiary field $\mathbf{M}$, $\mathrm{div}\mathbf{M} = 0$. This is consistent with the equation of motion for $\mathbf{M}$, which leads to $\partial_t(\mathrm{div}\mathbf{M}) = 0$. Therefore, supposing that $\mathrm{div}\mathbf{M} = 0$ holds for some initial moment, we arrive at the conclusion that this is valid for an arbitrary moment. On the other hand, putting $\Lambda \equiv 0$ in the action leads to vanishing of the Λ term in the vector potential equation of motion, making it gauge-dependent. It proves convenient to deal with $\Lambda \neq 0$, which makes it possible to use different gauge conditions for the vector potential.

We do not include the subsidiary field Λ into the set of the canonical variables but suppose it to be an independent variable in the variational principle with the action defined by Eq. (10), dealing with the extended Hamiltonian description (cf. [20]). Alternatively, one can include it into the set of generalized coordinates. Denoting corresponding conjugate momentum π_Λ and adding to the Hamiltonian density (Eq. (1)), the term $\pi_\Lambda\nu$ results in $\dot{\pi}_\Lambda = -\delta\mathcal{H}/\delta\Lambda = -\mathrm{div}\mathbf{M}$, $\dot{\Lambda} = \delta\mathcal{H}/\delta\pi_\Lambda = \nu$. The subsidiary function ν can be expressed in terms of other variables as $\nu = \partial_t\Delta^{-1}([\mathbf{v}\times\mathbf{H}] - \dot{\mathbf{A}}) + \nu_0$, where Δ denotes the Laplace operator and ν_0 is an arbitrary solution of the Laplace equation. π_Λ is a linear function of t, $\pi_\Lambda = \pi_\Lambda(t_0) - (t - t_0)\mathrm{div}\mathbf{M}$, as follows from (8). Putting $\pi_\Lambda(t_0)$ and $\mathrm{div}\mathbf{M}(t) \equiv \mathrm{div}\mathbf{M}(t_0) = 0$, we arrive at the

specific case with the *a posteriori* zero-valued π_Λ. Note also that for $\mathbf{M}(t_0) = 0$, some generalized invariants become gauge-independent (see below).

The canonical description introduced for MHD is equivalent (obviously, up to the gauge transformations of the subsidiary fields) to the conventional description. This fact strictly follows from the generalization of the Weber transformation. The latter consists in partial integration of the Euler equation. Suppose that the fluid particles are labeled by Lagrange markers $\mathbf{a} = (a_1, a_2, a_3)$. Then the label of the particle passing through point $\mathbf{r} = (x_1, x_2, x_3)$ at time t is

$$\mathbf{a} = \mathbf{a}(\mathbf{r}, t), \text{ and, consequenty, } D\mathbf{a} = 0. \quad (11)$$

The particle paths and velocities are given by the inverse function

$$\mathbf{r} = \mathbf{r}(\mathbf{a}, t), \quad \mathbf{v} = D\mathbf{r}(\mathbf{a}, t) = \partial\mathbf{r}/\partial t|_{\mathbf{a}=\text{const}}. \quad (12)$$

Representing the equation of motion in the form

$$Dv_k = -\frac{\partial w}{\partial x_k} + T\frac{\partial s}{\partial x_k} + [\mathbf{J}\times\mathbf{h}]_k, \qquad \mathbf{h} \equiv \frac{\mathbf{H}}{\rho}, \quad \mathbf{J} = \frac{\text{curl}\mathbf{H}}{4\pi}, \quad (13)$$

multiplying it by dx_k/da_i, and performing simple transformations, we have

$$D\left(v_k\frac{\partial x_k}{\partial a_i}\right) = \frac{\partial}{\partial a_i}(v^2/2 - w) + T\frac{\partial s}{\partial a_i} + [\mathbf{J}\times\mathbf{h}]_k\frac{\partial x_k}{\partial a_i}. \quad (14)$$

Introducing subsidiary fields φ, σ, and $\mathbf{M}$ governed by equations (compare second equations in (5), (7), (8))

$$D\varphi = w - \frac{v^2}{2}, \quad D\left(\frac{\sigma}{\rho}\right) = -T, \qquad \dot{\mathbf{M}} = \text{curl}[\mathbf{v}\times\mathbf{M}] + \mathbf{J} \quad (15)$$

we can represent the right-hand side of Eq. (14) as the sum of the substantial derivatives in accordance with identities:

$$T\frac{\partial s}{\partial a_i} = -D\left(\frac{\partial s}{\partial a_i}\frac{\sigma}{\rho}\right),$$

$$\frac{\partial}{\partial a_i}\left(w - \frac{v^2}{2}\right) = D\left(\frac{\partial\varphi}{\partial a_i}\right),$$

$$[\mathbf{J}\times\mathbf{h}]_k\partial x_k/\partial a_i = D([\mathbf{M}\times\mathbf{h}]_k\partial x_k/\partial a_i)$$

which makes it possible to integrate the Euler equation (14):

$$-v_k\frac{\partial x_k}{\partial a_i} = \frac{\partial\varphi}{\partial a_i} + \frac{\partial s}{\partial a_i}\frac{\sigma}{\rho} + [\mathbf{h}\times\mathbf{M}]_k\frac{\partial x_k}{\partial a_i} + b_i, \qquad D\mathbf{b} = 0. \quad (16)$$

Multiplying this relation by $\partial a_i/\partial x_j$ allows one to revert from Lagrangian, $(\mathbf{a}, t)$, to the Eulerian, $(\mathbf{r}, t)$, variables,

$$\mathbf{v} = -\nabla\varphi - b_k\nabla a_k - \frac{\sigma}{\rho}\nabla s - [\mathbf{h}\times\mathbf{M}]. \quad (17)$$

The velocity representation following from the Weber transformation obviously coincides with the above-introduced generalized Clebsch representation if one identifies $\mathbf{b}$ with $\boldsymbol{\lambda}/\rho$ and $\mathbf{a}$ with $\boldsymbol{\mu}$. This proves the above-mentioned equivalence between description of the general-type magnetohydrodynamic flows in terms of canonical variables introduced and the conventional description in Lagrange or Euler variables. Moreover, this indicates that the velocity representation of the form of Eq. (3) is the basic one. The possible reductions based upon the Darboux (in other words, Pfaff's) theorem lead to the restrictions for the motion or, otherwise, involve non-single-valued functions (cf. [2]).

The decomposition of the velocity in the "hydrodynamic" and "magnetic" parts allows one to obtain "missing" MHD invariants. Namely, strict but rather cumbersome calculations show that the generalized vorticity

$$\boldsymbol{\omega}_h \equiv \text{curl}\mathbf{v}_h \quad (18)$$

satisfies equation

$$\dot{\boldsymbol{\omega}}_h = [\Delta\rho\times\nabla p]/\rho^2 + \text{curl}[\mathbf{v}\times\boldsymbol{\omega}_h]. \quad (19)$$

For the barotropic flows, $\boldsymbol{\omega}_h/\rho$ becomes a frozen-in field,

$$D\left(\frac{\boldsymbol{\omega}_h}{\rho}\right) = \left(\frac{\boldsymbol{\omega}_h}{\rho}\cdot\nabla\right)\mathbf{v} \text{ for } p = p(\rho), \quad (20)$$

presenting a clear generalization of the hydrodynamic vorticity for the MHD case. Note that the quantity $\boldsymbol{\omega}/\rho$, $\boldsymbol{\omega} \equiv \text{curl}\mathbf{v}$, is not a frozen field due to the nonpotential character of the Lorentz force.

Starting with Eq. (19), one can prove the generalization of the Thompson theorem: circulation Γ of $\mathbf{v}_h$ over the closed substantial contour $\mathcal{C}$ lying on the entropy-constant surface is the integral of motion

$$D\Gamma \equiv D\oint_{\mathcal{C}}(\mathbf{v}_h\cdot d\mathbf{l}) = 0 \text{ for } s|_{\mathcal{C}} = \text{const}. \quad (21)$$

Analogously, the pseudoscalar $h_H \equiv (\mathbf{v}_h\cdot\boldsymbol{\omega}_h)$ (generalized helicity) is conserved for the barotropic flows

$$\dot{h}_H + \text{div}\mathbf{q}_H = 0, \quad h_H = (\mathbf{v}_h\cdot\boldsymbol{\omega}_h), \qquad \mathbf{q}_H = h_H\mathbf{v} + (\chi - v^2/2)\boldsymbol{\omega}_h, \quad \chi \equiv \int dp/\rho. \quad (22)$$

The corresponding integral-conserved quantity $\mathcal{I}_H$ can be obtained by integration of h_H over substantial volume $\tilde{V}$ such that on its boundary the normal component of the generalized vorticity vanishes, $\omega_{hn} = 0$ (note that it is sufficient to require fulfillment of the latter condi-

tion for the initial moment only due to the frozen-in character of $\boldsymbol{\omega}_h/\rho$),

$$D\mathcal{I}_H = 0 \text{ for } (\boldsymbol{\omega}_h \cdot \mathbf{n})|_{\partial\tilde{V}} = 0, \quad \mathcal{I}_H \equiv \int_{\tilde{V}} d\mathbf{r} h_H. \quad (23)$$

For the incompressible case, the generalized vorticity and helicity were introduced earlier in the paper [6].

The generalization of the Ertel invariant is represented by the quantity $\alpha_E = (\boldsymbol{\omega}_h \cdot \nabla s)/\rho$ following from the conventional hydrodynamics expression by substitution $\boldsymbol{\omega}_h = \mathrm{curl}\mathbf{v}_h$ instead of $\boldsymbol{\omega} = \mathrm{curl}\mathbf{v}$,

$$D\alpha_E = 0, \quad (24)$$

without any restrictions concerning the flow. Integration of $h_E = \rho\alpha_E$ over the substantial volume yields the following conserved integral:

$$\mathcal{I}_E = \int_{\tilde{V}} d\mathbf{r} h_E, \quad D\mathcal{I}_E = 0. \quad (25)$$

$\mathcal{I}_E$ in its structure is not gauge-invariant, in contrast to the hydrodynamic case. Let us examine its change under gauge transformation $\mathbf{v}_h \longrightarrow \mathbf{v}'_h$, $\mathbf{v}_M \longrightarrow \mathbf{v}'_M$ with $\mathbf{v}'_h + \mathbf{v}'_M = \mathbf{v}_h + \mathbf{v}_M$. Then

$$\mathcal{I}'_E - \mathcal{I}_E = -\int_{\partial\tilde{V}} d\Sigma(\mathbf{n} \cdot [\nabla s \times (\mathbf{v}'_M - \mathbf{v}_M)]). \quad (26)$$

Now we can proceed in two ways. First, making use of the identity $[\nabla s \times \mathbf{X}] = \mathrm{curl}(s\mathbf{X}) - s \cdot \mathrm{curl}\mathbf{X}$ and taking into account that the integral of the first term vanishes (which is trivial for a closed boundary $\partial\tilde{V}$ and assumes the necessary decreasing of the integrand for the infinite volume $\tilde{V}$), we have

$$\mathcal{I}'_E - \mathcal{I}_E = \int_{\partial\tilde{V}} d\Sigma(\mathbf{n} \cdot (\boldsymbol{\omega}'_M - \boldsymbol{\omega}_M))s. \quad (27)$$

From representation (26), it immediately follows that the integral Ertel invariant becomes gauge-independent for the substantial volume $\tilde{V}$ chosen in such a way that its boundary coincides with the entropy-constant surface, $s|_{\partial\tilde{V}} = \mathrm{const}$.

The second way is as follows. Substituting into Eq. (26) $\mathbf{v}'_M - \mathbf{v}_M = -[\mathbf{h} \times (\mathbf{M}' - \mathbf{M})]$, we obtain

$$\mathcal{I}'_E - \mathcal{I}_E = \int_{\partial\tilde{V}} d\Sigma(\mathbf{n} \cdot [\nabla s \times [\mathbf{h} \times (\mathbf{M}' - \mathbf{M})]]). \quad (28)$$

Inasmuch as both $\mathbf{M}'$ and $\mathbf{M}$ satisfy the second equation in (8), their difference, $\overline{\mathbf{M}} = \mathbf{M}' - \mathbf{M}$, is governed by the corresponding homogeneous equation $\partial_t\overline{\mathbf{M}} = \mathrm{curl}[\mathbf{v} \times \overline{\mathbf{M}}]$, i.e., $\overline{\mathbf{m}} = \overline{\mathbf{M}}/\rho$ is a frozen-in field. From this property, it follows that the vector quantity $\mathbf{W} \equiv [\nabla s \times [\mathbf{h} \times \overline{\mathbf{m}}]]$ entering the integrand is a frozen-in field (this can be proved by strict calculations and also follows from the recursion relations between different types of invariants; see, for instance, [2, 10] and Eqs. (31), (32) below). Therefore, if we restrict ourselves to zero initial condition for the field $\mathbf{M}$, $\mathbf{M}_{t=t_0} = 0$, the initial value of $\mathbf{W}$ becomes zero, and, consequently, the initial value of its normal component on the surface of the substantial volume $\partial\tilde{V}$ is zero. But the normal component of the frozen-in field is invariant of the motion. Thus, we arrive at the conclusion that condition $(\mathbf{n} \cdot \mathbf{W}) = 0$ holds true for an arbitrary moment, and $\mathcal{I}_E$ becomes gauge-invariant if we imply zero initial conditions for the subsidiary field $\mathbf{M}$. Note that this choice does not impose any constraint on the motion.

There are also other possibilities to make $\mathcal{I}_E$ gauge-independent. For instance, we can restrict ourselves to a subset of the initial conditions for $\mathbf{M}$ such that $\mathbf{M}_{t=t_0} = f\mathbf{H}_{t=t_0}$, where f is an arbitrary function. (Then $\mathrm{div}\mathbf{M} = \mathrm{div}\mathbf{M}_{t=t_0} = (\nabla f \cdot \mathbf{H}_{t=t_0})$ and, for the particular choice of f such that $(\mathbf{H}_{t=t_0} \cdot \nabla f) = 0$, we have $\mathrm{div}\mathbf{M} = 0$.) For these initial conditions, $\mathbf{M}$ and $\mathbf{M}'$ are collinear to $\mathbf{H}$ at the initial moment, and therefore the initial value of $(\mathbf{n} \cdot \mathbf{W})$ is zero, and, consequently, it is zero for all moments. Thus, we can make the conclusion that the gauge dependence of the Ertel invariant can be partly eliminated by appropriate choice of the initial conditions or substantial volumes.

The performed analysis of the additional MHD integrals of motion makes it quite evident that, along with the well-known MHD integrals of motion (cf. [2]), they form the basis of the MHD local invariants. Starting with these invariants, one can obtain a wide set of invariants by means of recursion relations between different types of invariants. Recall that for hydrodynamic-type systems there exist four types of local invariants. By definition they obey the following equations:

$$D\alpha = 0, \quad D\mathbf{I} = 0, \quad D\mathbf{J} - (\mathbf{J} \cdot \nabla)\mathbf{v} = 0, \quad (29)$$

$$D\mathbf{L} + (\mathbf{L} \cdot \nabla)\mathbf{v} + [(\mathbf{L} \times \mathrm{curl}\mathbf{v}] = 0. \quad (30)$$

Here, α and $\mathbf{I}$ represent the scalar and vector Lagrange invariants, $\mathbf{J}$ is frozen-in field, and $\mathbf{L}$ presents Lamb-type momentum invariant (cf. [16]). The main representative of the fourth-type invariants is the fluid density ρ; all other ρ-type invariants can be obtained by multiplying the local Lagrange invariants by ρ. The recursion relations

$$\mathbf{L}' = \nabla\alpha, \quad \alpha' = (\mathbf{J} \cdot \mathbf{L}), \quad (31)$$

$$\mathbf{J}' = [\mathbf{L} \times \mathbf{L}']/\rho, \quad \mathbf{L}' = \rho[\mathbf{J} \times \mathbf{J}'] \quad (32)$$

allow one to construct new invariants in terms of the initial ones. The procedure is somewhat different for the general-type motion and barotropic (or isentropic)

flows. Let us consider the general case. The basic set of invariants can be chosen as

$$s, \alpha_E, \mathbf{h} = \mathbf{H}/\rho. \quad (33)$$

Applying recursion relations, we first obtain new **L**-type invariants, $\mathbf{L}_s = \nabla s$, $\mathbf{L}_E = \nabla\alpha_E$. These invariants allow us to get new α-type,

$$\alpha_P = (\mathbf{h}\cdot\nabla)s, \quad \alpha_E^{(1)} = (\mathbf{h}\cdot\nabla)\alpha_E, \quad (34)$$

and **J**-type, $\mathbf{J}' = [\nabla s \times \nabla\alpha_E]/\rho$, invariants. The first invariant in Eq. (34) was obtained in [21]. It is evident that invariants α_P and α_E are members of the infinite sets of (monomial) invariants

$$\alpha_P^{(m)} = \mathcal{D}^m s, \quad \alpha_E^{(m)} = \mathcal{D}^m\alpha_E, \quad m = 0, 1, \ldots, \quad (35)$$

where $\mathcal{D} = (\mathbf{h}\cdot\nabla)$. The first set was discussed in [2], and the second is the new one together with the generalized Ertel invariant α_E. The more general set of the scalar invariants can be represented by expression $\alpha_f = f(\{\alpha_P^{(m)}\}, \{\alpha_E^{(m)}\})$, where f is an arbitrary function. Note that the set $\{\alpha_f\}$ is closed relative to the operation $\mathcal{D}$.

We can proceed further constructing new scalar invariants by applying operation $\mathcal{D}_1 = (\mathbf{J}'\cdot\nabla)$ to the scalar invariants obtained at the previous step and obtaining new **L**- and **J**-type invariants. The problems relating to the complete set of the local invariants, their gauge invariance, and specific types of flows will be discussed further.

The results obtained can be summarized as follows. First, the variant of introducing the canonical description of the MHD flows by means of the variational principle is presented. It is shown that in order to describe general-type MHD flows it is necessary to use in the generalized Clebsch-type representation for the fluid velocity field the vector Clebsch variables (the Lagrange markers and conjugate momenta) along with the entropy term (compare papers [18, 19] describing hydrodynamic case) and the conventional magnetic term. This complete representation allows one to deal with general-type MHD flows, including all types of breaks (see [17]). Second, the generalization of the Weber transformation for the MHD flows is performed. Third, the equivalence between the velocity representations, following, respectively, from the Weber transformation, and that introduced by means of the variational principle is proved. Fourth, the generalized Ertel invariant for MHD flows is found. Fifth, the generalized vorticity and helicity invariants for the compressible barotropic MHD flows are obtained. Sixth, the relations between the local and integral invariants are discussed along with the gauge dependence of the latter. Seventh, as a consequence of the completeness of the representation proposed, we arrive at the correct limit transition from the MHD to the conventional hydrodynamic flows. The results obtained allow one to deal with complicated MHD problems by means of the Hamiltonian variables. The use of such an approach was demonstrated for the specific case of incompressible flows in the series of papers devoted to the nonlinear stability criteria.

This work was supported by INTAS (grant no. 00-00292).

REFERENCES

1. H. K. J. Moffatt, J. Fluid Mech. **35**, 117 (1969).
2. V. E. Zakharov and E. A. Kuznetsov, Usp. Fiz. Nauk **167**, 1137 (1997) [Phys. Usp. **40**, 1087 (1997)].
3. E. Hameiri, Phys. Plasmas **5**, 3270 (1998).
4. J. A. Almaguer, E. Hameiri, J. Herrera, and D. D. Holm, Phys. Fluids **31**, 1930 (1988).
5. V. I. Ilgisonis and V. P. Pastukhov, Fiz. Plasmy (Moscow) **22**, 228 (1996) [Plasma Phys. Rep. **22**, 208 (1996)].
6. V. A. Vladimirov and H. K. Moffatt, J. Fluid Mech. **283**, 125 (1995).
7. V. A. Vladimirov, H. K. Moffatt, and K. I. Ilin, J. Fluid Mech. **390**, 127 (1999).
8. A. V. Kats, physics/0212023 (2002).
9. A. Clebsch, J. Angew. Math., Crelle **56** (1) (1859).
10. V. P. Goncharov and V. I. Pavlov, *The Problems of Hydrodynamics in Hamiltonian Description* (Mosk. Gos. Univ., Moscow, 1993).
11. V. E. Zakharov and E. A. Kuznetsov, Dokl. Akad. Nauk SSSR **194**, 1288 (1970) [Sov. Phys. Dokl. **15**, 913 (1970)].
12. H. Weber, J. Reine Angew. Math. **68**, 286 (1868).
13. H. Lamb, *Hydrodynamics*, 6th ed. (Cambridge Univ. Press, Cambridge, 1932; Gostekhizdat, Moscow, 1947).
14. E. A. Kuznetsov and V. P. Ruban, Phys. Rev. E **61**, 831 (2000).
15. S. S. Moiseev, R. Z. Sagdeev, A. V. Tur, and V. V. Yanovskiĭ, Zh. Éksp. Teor. Fiz. **83**, 215 (1982) [Sov. Phys. JETP **56**, 117 (1982)]; S. S. Moiseev *et al.*, in *Nonlinear Phenomena in Plasma and Hydrodynamics* (Mir, Moscow, 1986).
16. D. V. Volkov, A. V. Tur, and V. V. Yanovsky, Phys. Lett. A **203**, 357 (1995).
17. A. V. Kats, Radiofiz. Radioastron. **7**, 232 (2002).
18. A. V. Kats and V. M. Kontorovich, Fiz. Nizk. Temp. **23**, 120 (1997) [Low Temp. Phys. **23**, 89 (1997)].
19. A. V. Kats, Physica D (Amsterdam) **152–153**, 459 (2001).
20. D. M. Gitman and I. V. Tyutin, *Canonical Quantization of the Fields with Constraints* (Nauka, Moscow, 1986).
21. V. A. Gordin and V. I. Petviashwili, Fiz. Plasmy (Moscow) **13**, 880 (1987) [Sov. J. Plasma Phys. **13**, 509 (1987)].

JETP Letters, Vol. 77, No. 12, 2003, pp. 662–665. Translated from Pis'ma v Zhurnal Éksperimental'noĭ i Teoreticheskoĭ Fiziki, Vol. 77, No. 12, 2003, pp. 794–797.

Commensurate Oscillations of the Magnetoresistance of a Two-Dimensional Electron Gas in GaAs Quantum Wells with Corrugated Heteroboundaries

A. K. Bakarov*, A. A. Bykov, N. D. Aksenova, D. V. Sheglov, A. V. Latyshev, and A. I. Toropov

Institute of Semiconductor Physics, Siberian Division, Russian Academy of Sciences, Novosibirsk, 630090 Russia

**e-mail: bakarov@thermo.isp.nsc.ru*

Received March 26, 2003; in final form, May 5, 2003

Oscillations of the magnetoresistance commensurate with the spatial modulation period of the growth surfaces were observed in selectively doped GaAs quantum wells with AlAs/GaAs superlattice barriers grown by molecular beam epitaxy. The experimental data obtained are explained by the lateral potential modulation of the two-dimensional electron gas in narrow GaAs quantum wells with corrugated heteroboundaries and agree with the two-dimensional distribution of the local capacitance in such structures. © *2003 MAIK "Nauka/Interperiodica".*

PACS numbers: 73.63.Hs; 73.21.Fg

Numerous experimental studies showed that heteroboundaries in semiconductor structures grown by molecular beam epitaxy (MBE) are not perfectly planar. To some extent, irregularity (corrugation) of heteroboundaries is present in any real MBE structure. Of the number of possible reasons leading to the irregularity of heteroboundaries, the two most important ones should be singled out: the roughness of the initial substrate surfaces [1] and the self-organization of the mounded surface in the growth process [2]. In this work, it is shown that the mounding behavior of the growth surfaces arising in the MBE process leads to the appearance of a long-range scattering potential in selectively doped structures.

The structures under study were selectively GaAs-doped quantum wells 10 nm thick with AlAs/GaAs superlattice barriers [3, 4] grown by MBE on GaAs(100) substrates. The misorientation angle of the substrates did not exceed 0.02°. The surface morphology of the prepared structures was studied using atomic force microscopy (AFM). Magnetotransport experiments were carried out at a temperature of 4.2 K in magnetic fields up to 2 T on *L*-shaped Hall-effect bridges, in which the measuring current flowed along the [110] and $[1\bar{1}0]$ directions.

Studies of the relief using AFM showed an anisotropic character of the surface morphology on all grown structures. A decrease in the As_4 flow led to an increase in the height of the spatial modulation and the degree of anisotropy of the growth surfaces, all other factors being the same [1]. A characteristic AFM image of the surface relief of a structure grown at a minimum As_4 flow required for the maintenance of the As-stabilized surface superstructure is shown in Fig. 1a. The results of a correlation analysis of this surface are presented in Fig. 1b. The anisotropy and periodic character of the surface morphology are clearly seen in the figure. The mobility of the two-dimensional electron gas (2DEG) in this structure at $T = 4.2$ K for the concentration $n_s = 1.7 \times 10^{12}$ cm^{-2} was $\mu_{xx} = 170 \times 10^3$ cm^2 V^{-1} s^{-1} in the [110] direction and $\mu_{yy} = 280 \times 10^3$ cm^2 V^{-1} s^{-1} in the $[1\bar{1}0]$ direction. That is the mean free path by the momentum in the [110] direction $l_{pxx} \sim 2.5$ μm exceeded the spatial modulation period of the growth surfaces $d_{xx} \sim 0.8$ μm in the same direction.

The dependences $\rho_{xx}(B)$ and $\rho_{yy}(B)$ are presented in Fig. 2a for the measuring current flowing along the [110] and $[1\bar{1}0]$ directions, respectively. A difference is observed in the $\rho_{xx}(B)$ and $\rho_{yy}(B)$ values due to the anisotropy of the morphology of heteroboundaries, which is typical of such systems [5, 6]. A maximum appears in the $\rho_{xx}(B)$ dependence at $B = B_{\max}$, which points to one-dimensional periodic potential modulation of the 2DEG [7]. This assumption is fully confirmed by the fact that commensurate oscillations are observed in the magnetoresistance (MR) in the vicinity of $B = B_{\max}$ (Fig. 2b). These oscillations arise in the one-dimensional periodic potential when the conditions $R_c = (n + 1/4)a_{xx}$ are fulfilled, where $R_c = (2mE_F)^{1/2}(\text{eV})^{-1}$ is the classical radius of the cyclotron orbit, E_F is the 2DEG Fermi energy, a_{xx} is the potential modulation period, and n is a positive integer [8]. An analysis of the position of maxima in the magnetic field showed that

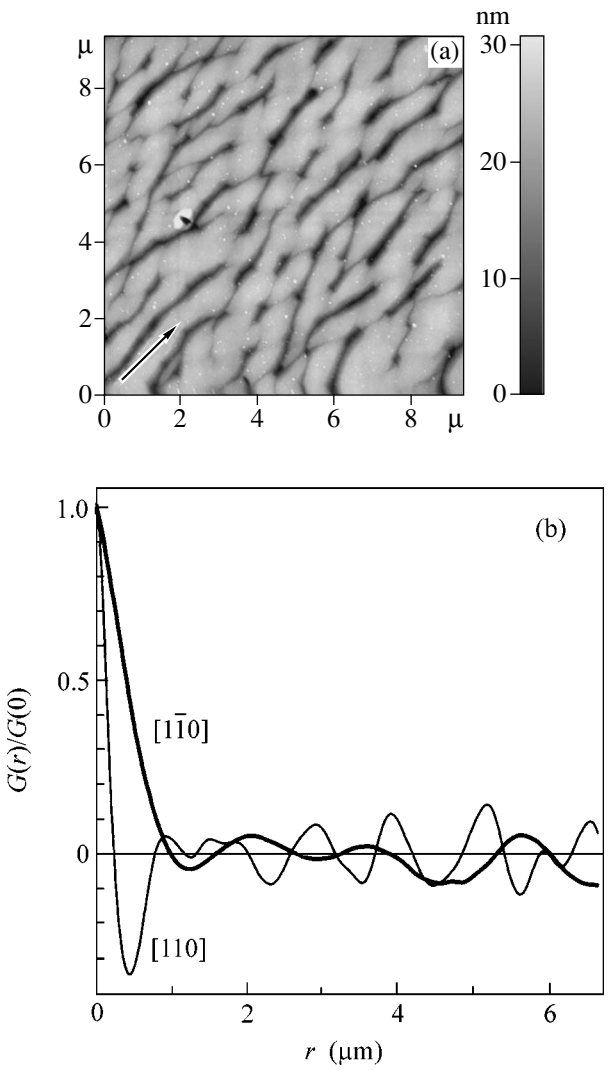

Fig. 1. (a) Two-dimensional AFM image of the surface relief of a "corrugated" MBE structure. The arrow indicates the [1$\bar{1}$0] direction. (b) Autocorrelation functions of the relief in the [110] and [1$\bar{1}$0] directions.

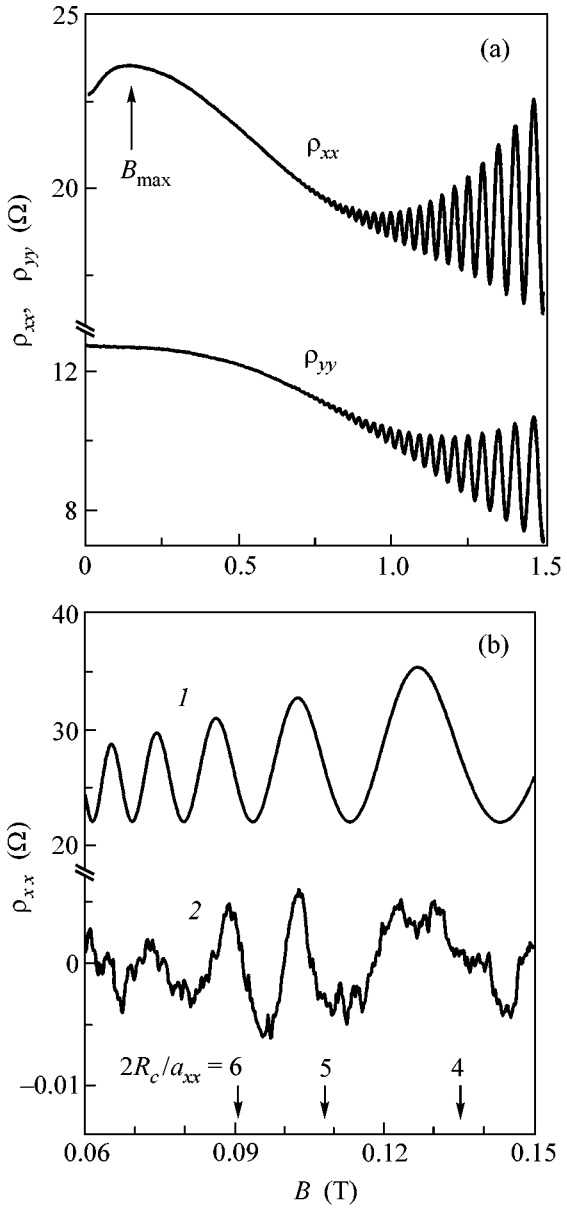

Fig. 2. (a) Longitudinal 2DEG MR in the [110] and [1$\bar{1}$0] directions (ρ_{xx} and ρ_{yy}, respectively) at T = 4.2 K for the concentration $n_s = 1.7 \times 10^{12}$ cm^{-2}. (b) (*1*) Theoretical dependence of the 2DEG MR for the concentration $n_s = 1.7 \times 10^{12}$ cm^{-2} and the mobility $\mu_{xx} = 170 \times 10^3$ cm^2 V^{-1} s^{-1} in a one-dimensional potential with the period a_{xx} = 0.8 μm and the amplitude V_0 = 10 meV. (*2*) The longitudinal MR in the [110] direction with the subtracted monotonic component.

these are due to the potential modulation of the 2DEG with a period $a_{xx} \sim 0.8$ μm, which coincides, to the accuracy of measurements, with the spatial modulation period of the heteroboundaries in the [110] direction determined by AFM.

This experimental fact allows the conclusion to be drawn that the nonplanarity of the growth surfaces is the reason for the lateral potential modulation of the 2DEG in selectively GaAs-doped quantum wells. The magnitude of the potential modulation of the 2DEG calculated by the equation $V_0 = B_{max}a_{xx}(E_F/2\pi^2 m)^{1/2}$ from the work [9] make up 10–15 meV for $E_F \sim$ 60 meV. The theoretical dependence of the 2DEG MR in the one-dimensional periodic potential [8] with the modulation amplitude V_0 = 10 meV and the period a_{xx} = 0.8 μm is represented by curve *1* in Fig. 2b. As is evident in the figure, the amplitude of the commensurate oscillations observed in this work is significantly smaller than the theoretical value. We relate this experimental result to the fact that the potential modulation of the 2DEG in the studied GaAs quantum wells with

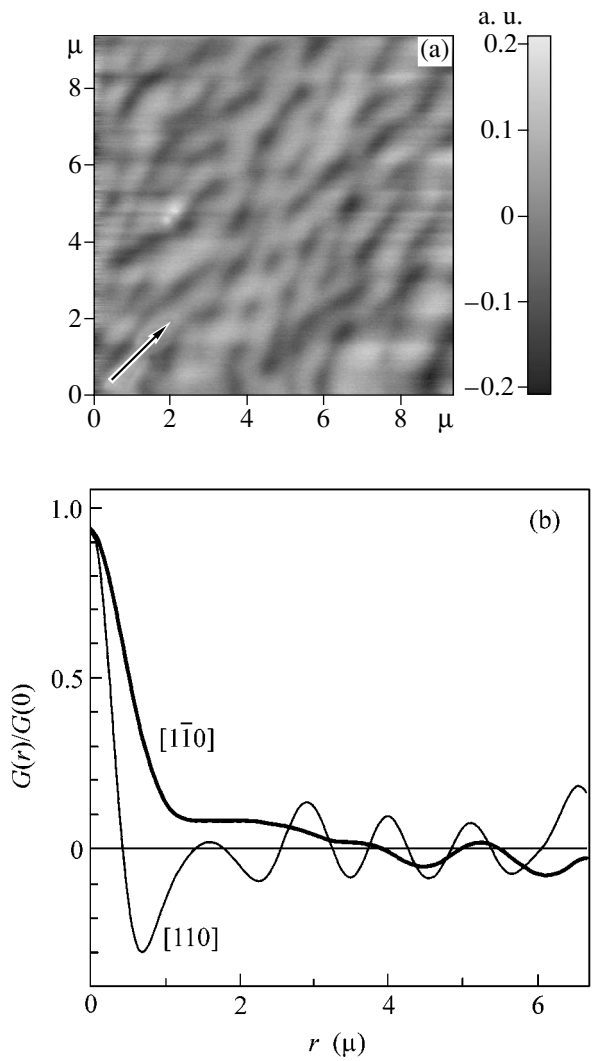

Fig. 3. (a) Local capacitance distribution over the surface of a corrugated MBE structure. The arrow indicates the [1$\bar{1}$0] direction. (b) Autocorrelation functions of the local capacitance distribution in the [110] and [1$\bar{1}$0] directions.

corrugated heteroboundaries is not strictly periodic and one-dimensional [10].

The above interpretation of the experimental data is also in qualitative agreement with the two-dimensional distribution of the local capacitance in the studied structures (Fig. 3a). The local capacitance was measured using a SOLVER P47-H NT-MDT atomic force microscope operating in the noncontact mode using a double-pass procedure that takes into account the effect of the surface relief on the measured local capacitance. In this case, the surface topography is measured during the first passage of the probe (Fig. 1a), and the capacitance signal is measured during the second passage (Fig. 3a) when the probe moves above the surface along the already measured trajectory. The use of this procedure allows one to assume that the surface inhomogeneity of the 2DEG concentration is the main reason for the variation of the local capacitance. The results of the correlation analysis of the two-dimensional image of the local capacitance are given in Fig. 3b. The identity of the autocorrelation functions of the height and capacitance distributions (Fig. 1b and Fig. 3b) is an additional argument that corroborates the conclusion that the lateral potential modulation of the 2DEG in narrow GaAs quantum wells is caused by the morphology of the growth surfaces.

We believe that the variation of the width of the GaAs quantum well along nonplanar heteroboundaries is one of the most probable reasons leading to the lateral modulation of the 2DEG potential in the MBE structures under study [11, 12]. It should be noted that the nonplanarity of the growth surfaces in selectively doped MBE structures will lead not only to the variation of the distance between the quantum-well heteroboundaries but also to the variation of the spacer thickness and to nonuniform incorporation of the dopant. That is, in the general case, there are several mechanisms of the generation of the long-range scattering potential in MBE structures with self-organized corrugated heteroboundaries. Without going into the analysis of particular mechanisms leading to the lateral potential modulation of the 2DEG in GaAs quantum wells, the following inferences about the character of the long-range scattering potential in such structures can be made based on a comparison of the relief of the growth surfaces, the local-capacitance distribution, and magnetotransport measurements.

The long-range scattering potential caused by the nonplanarity of the growth surfaces in MBE structures grown on GaAs(100) substrates is anisotropic. The amplitude and the two-dimensional form of the long-range scattering potential in GaAs quantum wells with AlAs/GaAs superlattice barriers depend on the growth conditions. In conditionally "smooth" structures, it has no clearly defined period and is manifested only in the anisotropy of the 2DEG conductivity [5]. MR anisotropy was observed in all the samples studied in this work and was smaller in the structures with a smaller height of the relief of the growth surfaces, all other factors being the same. In well-defined "corrugated" MBE structures, the long-range scattering potential is quasi-periodic and leads not only to the conductivity anisotropy but also to commensurate MR oscillations.

Thus, the 2DEG MR in narrow GaAs quantum wells with AlAs/GaAs superlattice barriers exhibits oscillations commensurate with the spatial modulation period of the growth surfaces. The experimental data obtained are explained by the lateral potential modulation of the 2DEG in narrow GaAs quantum wells with self-organized nonplanar heteroboundaries. These data point to the importance of the spatial modulation of the growth surfaces in the appearance of the long-range scattering potential in selectively doped MBE structures.

This work was supported by the Russian Foundation for Basic Research, project no. 01-02-16892.

REFERENCES

1. A. Ballestad, B. J. Ruck, M. Adamcuk, *et al.*, Phys. Rev. B **65**, 205302 (2002).
2. G. Apostolopoulos, J. Herfort, L. Daweritz, *et al.*, Phys. Rev. Lett. **84**, 3358 (2000).
3. K.-J. Friedland, R. Hey, H. Kostial, *et al.*, Phys. Rev. Lett. **77**, 4616 (1996).
4. A. A. Bykov, A. K. Bakarov, L. V. Litvin, and A. I. Toropov, Pis'ma Zh. Éksp. Teor. Fiz. **72**, 300 (2000) [JETP Lett. **72**, 209 (2000)].
5. A. A. Bykov, A. K. Bakarov, A. V. Goran, *et al.*, Pis'ma Zh. Éksp. Teor. Fiz. **74**, 182 (2001) [JETP Lett. **74**, 164 (2001)].
6. K.-J. Friedland, R. Hey, O. Bierwagen, *et al.*, Physica E (Amsterdam) **13**, 642 (2002).
7. P. H. Beton, E. S. Alves, P. C. Main, *et al.*, Phys. Rev. B **42**, 9229 (1990).
8. C. W. J. Beenakker, Phys. Rev. Lett. **62**, 2020 (1989).
9. P. H. Beton, M. W. Dellow, P. C. Main, *et al.*, Phys. Rev. B **43**, 9980 (1991).
10. D. E. Grant, A. R. Long, and J. H. Davies, Phys. Rev. B **61**, 13127 (2000).
11. M. Akabori, J. Motohisa, and T. Fukui, Physica E (Amsterdam) **7**, 766 (2000).
12. Y. Yayon, A. Esser, M. Rappaport, *et al.*, Phys. Rev. Lett. **89**, 157402 (2002).

Translated by A. Bagatur'yants

JETP Letters, Vol. 77, No. 12, 2003, pp. 666–670. From Pis'ma v Zhurnal Éksperimental'noĭ i Teoreticheskoĭ Fiziki, Vol. 77, No. 12, 2003, pp. 798–802.

Anomaly in the Tunneling $I(V)$ Characteristics of $Bi_2Sr_2CaCu_2O_{8+x}$¶

A. Mourachkine

Free University of Brussels, B-1050 Brussels, Belgium

Received May 12, 2003

Tunneling measurements have been carried out on slightly overdoped $Bi_2Sr_2CaCu_2O_{8+x}$ single crystals below and above the critical temperature by break-junctions and in-plane point-contacts. An anomaly was found in the tunneling $I(V)$ characteristics. Analysis of the data shows that the anomaly is caused by the superconducting condensate. In the extracted $I(V)$ characteristics of the condensate, the constant asymptotics points to the presence of one-dimensionality in Bi2212. The anomaly found here puts additional constraints on the final theory of high-T_c superconductivity. © *2003 MAIK "Nauka/Interperiodica".*

PACS numbers: 74.50.+r; 74.72.Hs; 74.25.-q

Soon after the discovery of superconductivity (SC) in cuprates [1], it became clear that the concept of the Fermi liquid is not applicable to cuprates: the normal-state properties of cuprates are markedly different from those of conventional metals [2]. The pseudogap, which manifests itself in electronic excitation spectra of cuprates above the critical temperature T_c, is one of the main features of high-T_c SCs. There is a consensus on the doping dependence of the pseudogap in hole-doped cuprates: the magnitude of the pseudogap decreases as the hole concentration increases. Angle-resolved photoemission spectroscopy (ARPES) measurements performed in $Bi_2Sr_2CaCu_2O_{8+x}$ (Bi2212) show that the ARPES spectra consist of two *independent* contributions—from the pseudogap (hump) and the SC condensate (quasiparticle peak) [3]. As the temperature decreases, the quasiparticle peak appears in the spectra slightly above T_c on one side of the hump, meaning that the pseudogap and the SC gap coexist below T_c in Bi2212.

In addition to their peculiar normal-state properties, a number of experiments show that some SC properties of cuprates deviate from the predictions of BCS theory for conventional SCs [2]. For example, the BCS isotope effect is almost absent in optimally doped cuprates. As another example, let us compare tunneling data obtained in cuprates and theoretical predictions for conventional SCs. Figure 1 shows a theoretical $I(V)$ curve for classical SCs (Fig. 6 in [4]) and a tunneling $I(V)$ characteristic obtained in an underdoped Bi2212 single crystal (Fig. 1 in [5]). In the *tunneling* regime, depending on the normal resistance of a junction, the theoretical $I(V)$ curve at high positive (low negative) bias lies somewhat below (above) the normal-state curve, as shown in Fig. 1a. In conventional SCs, the so-called Blonder–Tinkham–Klapwijk (BTK) predictions are verified by tunneling experiments. In cuprates, as one can see in Fig. 1b, the BTK theory is violated: the $I(V)$ curve at high positive (low negative) bias passes not below (above) the line which is parallel to the $I(V)$ curve at high bias but far above (below) the line. This anomaly cannot be explained by the *d*-wave symmetry of the order parameter. This question, for the first time, was raised elsewhere [6]. This finding is the main motivation of the present work.

The data shown in Fig. 1b are obtained in an underdoped Bi2212 single crystal in a SC–insulator–SC (SIS) tunneling junction. If the anomaly is an intrinsic feature of SC in Bi2212, it has to be present in tunneling spectra in the overdoped region of Bi2212 as well. Second, if it is not a SIS-junction effect, it must also manifest itself in SC–insulator–normal metal (SIN)

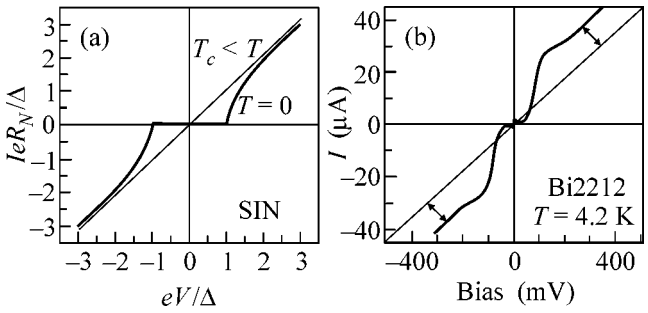

Fig. 1. (a) Theoretical tunneling $I(V)$ characteristic at $T = 0$ for a SIN junction of a SC with the isotropic energy gap [4]. The line is the normal-state curve. (b) Measured $I(V)$ curve in a SIS junction of an underdoped Bi2212 single crystal with $T_c = 83$ K, obtained at $T = 4.2$ K [5]. The line is parallel to the $I(V)$ curve at high bias, and the arrows show the offset from the line.

¶ This article was submitted by the author in English.

0021-3640/03/7712-0666$24.00 © 2003 MAIK "Nauka/Interperiodica"

junctions. Third, the line in Fig. 1b is not the normal-state curve; therefore, it is necessary to obtain tunneling spectra in the normal state. Finally, knowing the normal-state curves, one can estimate the contribution in tunneling spectra from the SC condensate. This work deals with the questions raised above. Tunneling measurements presented in this paper have been performed on overdoped Bi2212 single crystals below and above T_c by break-junctions and in-plane point-contacts, which reveal that the anomaly found in the tunneling $I(V)$ characteristics originates from the SC condensate. In the extracted $I(V)$ characteristics of the SC condensate, the constant asymptotics points to the presence of one-dimensionality in Bi2212. The anomaly found here puts additional constraints on the final theory of SC in cuprates.

It is important to note that the anomaly in tunneling $I(V)$ curves was already discussed in [6]; however, in [6], the anomaly was inferred from abnormal-looking tunneling characteristics. In this work, we show that this anomaly is intrinsically present in any $I(V)$ curve obtained below T_c in Bi2212. Also, the $I(V)$ characteristics measured above T_c were not considered in [6].

The overdoped Bi2212 single crystals were grown using the self-flux method as described elsewhere [7]. The T_c value was determined by the four-contact method. The transition width is less than 1 K. Experimental details of the measurement setup can be found elsewhere [7]. In short, many break-junctions were prepared by gluing a sample with epoxy on a flexible insulating substrate and then were broken in the *ab*-plane by bending the substrate with a differential screw at low temperature in a He ambient. The electrical contacts (typically with a resistance of a few ohms) are made by attaching gold wires to a crystal with silver paint. The $I(V)$ and $dI(V)/dV$ characteristics are determined by the four-terminal method by using the standard lock-in modulation technique. In in-plane SIN tunneling junctions, Pt–Ir wires sharpened mechanically were used as normal tips.

Figure 2a shows SIS tunneling spectra obtained by a break-junction at $T = 8.5$ K in an overdoped Bi2212 single crystal with critical temperature $T_c = 88$ K. The conductance $dI(V)/dV$ exhibits typical features of SIS-junction conductance data in Bi2212: well-defined quasiparticle peaks, a zero-bias peak due to the Josephson current, dips and humps outside the gap structure. As the main result, the $I(V)$ characteristic in Fig. 2a is similar to the $I(V)$ curve shown in Fig. 1b. The gap magnitude Δ, however, is smaller in the overdoped region. Figure 2b shows a set of tunneling $I(V)$ characteristics obtained in different overdoped Bi2212 single crystals with $T_c = 87$–89 K. Comparing Figs. 1b, 2a, and 2b, it is evident that the anomaly is present not only in the underdoped region of Bi2212 but in the overdoped region as well.

Figure 2c depicts tunneling spectra which are similar to those in Fig. 2a but obtained in a SIN junction.

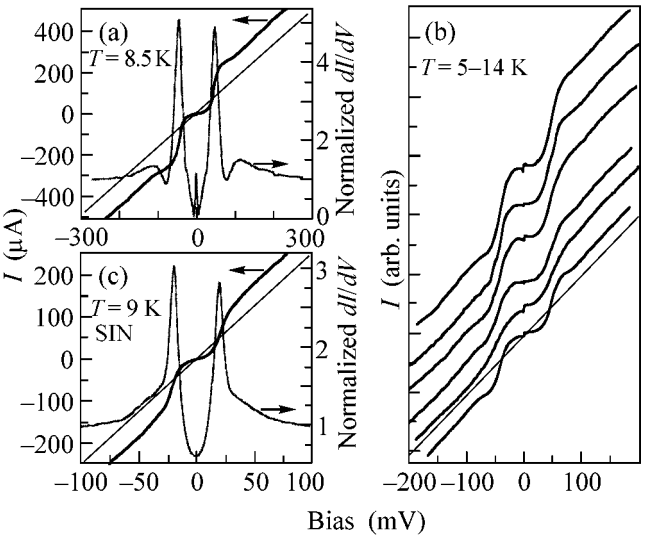

Fig. 2. (a) Tunneling $I(V)$ and $dI(V)/dV$ characteristics obtained at $T = 8.5$ K in a SIS junction of an overdoped Bi2212 single crystal with $T_c = 88$ K. (b) Set of $I(V)$ curves obtained at $T = 5$–14 K in different overdoped Bi2212 single crystals with $T_c = 87$–89 K. The curves are offset for clarity. (c) $I(V)$ and $dI(V)/dV$ characteristics obtained at $T = 9$ K in a SIN junction of an overdoped Bi2212 single crystal with $T_c = 87.5$ K. In all plots, the lines are parallel to the $I(V)$ curves at high bias. The label of the horizontal axis in plot (a) is the same as in plot (c).

Because of the SIN junction, the quasiparticle peaks in the conductance shown in Fig. 2c appear at a bias twice as small as the peak bias in Fig. 2a. The $I(V)$ curve in Fig. 2c clearly indicates that the observed anomaly is not a SIS-junction effect but an intrinsic feature of tunneling $I(V)$ characteristics obtained in Bi2212.

The next question that we discuss is how to obtain tunneling $I(V)$ characteristics in the normal state. There are at least three different solutions. The first two consist in applying a magnetic field below T_c, while the third solution is to measure $I(V)$ above T_c. In the first case, a magnetic field with a magnitude larger than the upper critical magnetic field H_{c2} in Bi2212 renders the whole sample normal. In the second case, by applying a magnetic field with a magnitude larger than the lower critical field H_{c1}, vortices will enter the sample. In the latter case, the normal-state characteristics can be obtained inside vortex cores. Because H_{c2} in Bi2212 is very large, the first solution cannot be realized in laboratory conditions. The second solution seems to be suitable; however, tunneling spectra obtained inside vortex cores have subgap structures which are usually interpreted as a manifestation of bound states [8]. Moreover, technically, it is not easy to realize such measurements. So, we are left with the straightforward solution: to measure $I(V)$ characteristics somewhat above T_c. The main disadvantage of measurements performed above T_c is the presence of substantial thermal fluctuations.

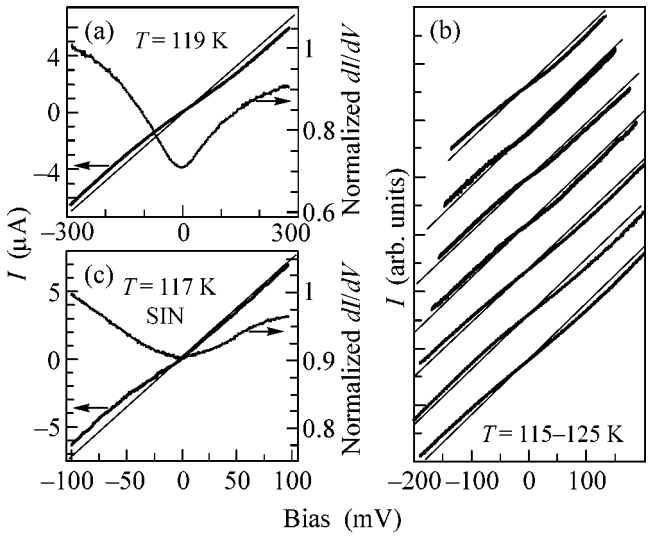

Fig. 3. (a) $I(V)$ and $dI(V)/dV$ characteristics obtained at T = 119 K in the same SIS junction as those in Fig. 2a. (b) Set of $I(V)$ curves obtained at T = 115–125 K in different overdoped Bi2212 single crystals with T_c = 87–89 K. The curves are offset for clarity. (c) $I(V)$ and $dI(V)/dV$ characteristics obtained at T = 117 K in the same SIN junction as those in Fig. 2c. In all plots, the lines are parallel to the $I(V)$ curves at high bias. The label of the horizontal axis in plot (a) is the same as in plot (c).

Figure 3a depicts tunneling spectra obtained at T = 119 K in the same Bi2212 single crystal as those in Fig. 2a. Figure 3b presents a set of $I(V)$ curves measured at T = 115–125 K in different overdoped Bi2212 single crystals. The data in Figs. 3a and 3b are obtained in SIS junctions. Figure 3c shows tunneling data obtained in a SIN junction at T = 117 K in the same Bi2212 single crystal as those in Fig. 2c. The temperatures between 115 and 125 K presented in Fig. 3 were not chosen by accident: in slightly overdoped Bi2212, the onset of SC occurs at 110–116 K [7]. This temperature range is above the onset of SC in our Bi2212 samples and, as a consequence, the data in Figs. 3a–3c mainly provide the contribution from the normal-state pseudogap.

Considering the $I(V)$ characteristics shown in Fig. 3, one can see that, at high positive (low negative) bias, they pass somewhat below (above) the line which is parallel to the $I(V)$ curves at high bias. Thus, the anomaly in the $I(V)$ characteristics found below T_c vanishes somewhat above T_c. Then, it is obvious that the anomaly in the $I(V)$ curves originates from the SC condensate. In Fig. 3, one can see that a straight line can be used as a first approximation for a normal-state $I(V)$ curve, for example, in Fig. 1b. In the $I(V)$ curves measured above T_c, a small "negative" offset from straight lines is caused by the pseudogap: measurements performed in underdoped Bi2212 show that this offset is larger than that in Fig. 3. Thus, it scales with the magnitude of the pseudogap.

We turn now to the last question raised above. From the tunneling characteristics obtained deep below T_c and somewhat above T_c, by taking the difference between the spectra, one can estimate a contribution in the tunneling spectra from the SC condensate. This is equivalent to the procedure usually used in neutron scattering measurements. In our case, however, this procedure only leads to an estimation of the contribution, because by subtracting the spectra we assume that the pseudogap crosses T_c without modification. This is not obvious, particularly at low bias [9].

In order to compare two sets of tunneling spectra, they have to be normalized. The conductance curves can be easily normalized at high bias. How to normalize the corresponding $I(V)$ curves is not a trivial question. The conductance curves at high bias, thus, far away from the gap structure, are almost constant. Consequently, in a SIS junction, by normalizing two conductance curves at high bias, the equation $(dI(V)/dV)_{1,\,\mathrm{norm}} \simeq (dI(V)/dV)_{2,\,\mathrm{norm}}$ holds at bias $|V| \gg 2\Delta/e$, where e is the electron charge. By integrating the equation, we have $I(V)_{1,\,\mathrm{norm}} \simeq I(V)_{2,\,\mathrm{norm}} + C$, where C is a constant, meaning that the corresponding $I(V)_{i,\,\mathrm{notm}}$ curves are parallel to each other at high bias.

In Fig. 4a, the two $I(V)$ characteristics from Figs. 2a and 3a were normalized as described in the previous paragraph: the normal-state $I(V)$ curve is normalized by its value at maximum positive bias, and the $I(V)$ curve from Fig. 2a is adjusted to be parallel at high bias to the normalized normal-state curve. Figure 4b depicts their difference as well as the difference between their normalized conductances. The same procedure has been performed for the tunneling spectra obtained in a SIN junction, which are shown in Figs. 2c and 3c. The differences are depicted in Fig. 4d. The conductances in Figs. 4b and 4d are presented as examples; however, they are not the primary focus of the study: we exclusively discuss the $I(V)$ characteristics. The $I(V)$ data shown in Fig. 1b, which are obtained in an underdoped Bi2212 single crystal, went through the same normalization procedure, and the result is presented in Fig. 4c. In the latter case, the straight line shown in Fig. 1b was used as a normal-state curve. The $I(V)$ characteristics shown in Fig. 2b and their corresponding normal-state curves were normalized in the same manner, and the obtained differences are presented in Fig. 4e.

Analyzing the $I(V)$ characteristics shown in Figs. 4b–4e, which, in the first approximation, represent the contribution from the SC condensate, it is easy to observe the general trends of the curves. First, at high bias, the curves reach a plateau value. Second, at the gap bias, the curves rise/fall sharply. Last, at low bias, the curves go to zero. In Figs. 4b–4e, the negative slope of the curves at low bias, implying a negative differential resistance, is an artifact. This artifact is simply a consequence of the rough estimation used here [9]. *Tout ensemble*, Fig. 4f depicts an idealized $I(V)$ characteristic summarizing the observed tendencies. The first

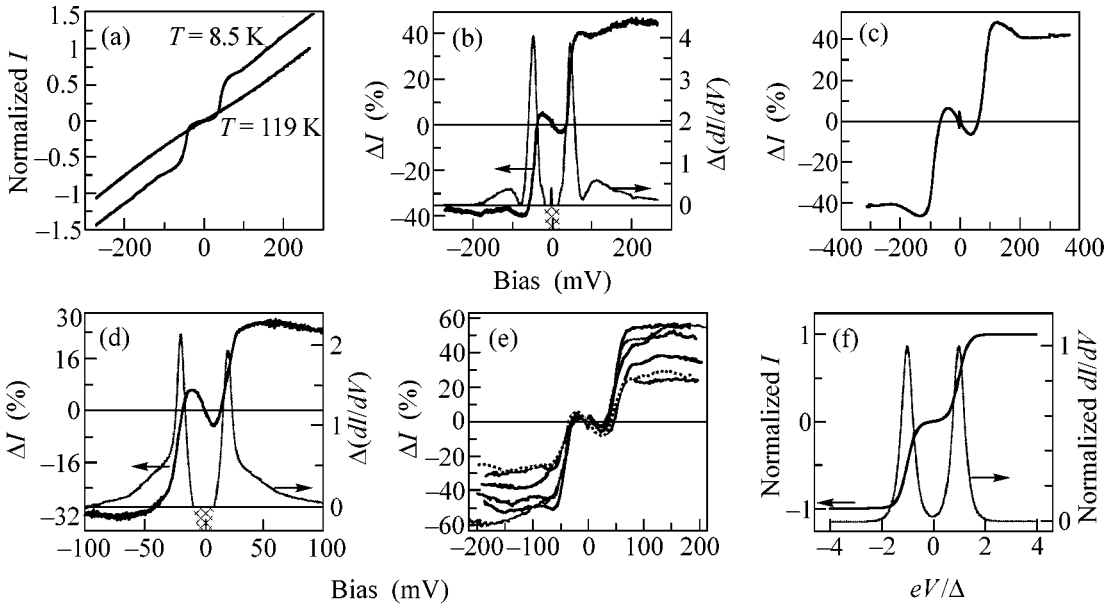

Fig. 4. (a) Two normalized $I(V)$ characteristics from Figs. 2a and 3a, obtained in the same Bi2212 single crystal (T_c = 88 K) at different temperatures. The normalization procedure: the normal-state curve is normalized by its value at maximum positive bias, and the other curve is adjusted to be parallel at high bias to the normalized normal-state curve. (b) Difference between the two $I(V)$ curves presented in plot (a), and the difference between their normalized conductances shown in Figs. 2a and 3a. (c) Difference between the $I(V)$ curve and the line shown in Fig. 1b, which were normalized before subtraction as those in plot (a). The straight line is used as an estimate of the normal-state curve. (d) Difference between the two $I(V)$ curves from Figs. 2c and 3c, normalized before subtraction as those in plot (a), and the difference between their normalized conductances. The data are obtained in a SIN junction. (e) Differences between $I(V)$ characteristics shown in Fig. 2b and their corresponding normal-state curves, normalized before subtraction as those in plot (a). (f) Idealized $I(V)$ characteristic of SC condensate in a SIN junction, and its first derivative. The curves are normalized by their maximum values. In plots (b) and (d), the gray boxes cover the parts of the conductances that are below zero and have no physical meaning. In plots (b)–(e), the current difference is presented in percent.

derivative of the $I(V)$ characteristic is also shown in Fig. 4f. The constant asymptotics of the $I(V)$ characteristic are the fingerprints of the presence of one-dimensionality in the system [6]. In Figs. 4b–4e, one can see that the contribution from the SC condensate in *these* $I(V)$ characteristics at high bias is 25–55% above the contribution from the pseudogap. It is *important* to note that the asymptotics of some $I(V)$ curves obtained in Bi2212 below T_c look similar to those in Fig. 1a; *however*, the anomaly discussed here always appears in the difference obtained between two normalized $I(V)$ curves measured *below* and *above* T_c in one sample.

As shown elsewhere [6], the $I(V)$ characteristic in Fig. 4f can be fitted by the hyperbolic function $f(V) = A(\tanh[(eV - \Delta)/eV_0] + \tanh[(eV + \Delta)/eV_0])$, where e is the electron charge, V is the bias, Δ is the maximum SC gap, and A and V_0 are constants. The conductance $dI(V)/dV$ curve can be well fitted by the derivative $[f(V)'] = A_1(\mathrm{sech}^2[(eV - \Delta)/eV_0] + (\mathrm{sech}^2[(eV + \Delta)/eV_0])$. The hyperbolic tanh and sech^2 fits are in good agreement with predictions of the bisoliton model [10], which is based on the nonlinear Schrödinger equation. The bisoliton theory utilizes the concept of bisolitons–electron (or hole) pairs coupled in a singlet state due to local deformation of the lattice [10].

Finally, it is worth mentioning that the anomaly found here is also present in an $I(V)$ characteristic obtained in optimally doped $YBa_2C_3O_{6.95}$ [11]. It is interesting that the anomaly is also present in the $I(V)$ characteristics measured in some nonsuperconducting materials—in the stripe-ordered perovskite $La_{1.4}Sr_{1.6}Mn_2O_7$ [12] and in quasi-one-dimensional charge-density-wave conductor $NbSe_3$ [13] (in $NbSe_3$, the anomaly is at zero bias). However, this issue is already beyond the scope of this study and will be discussed elsewhere.

In summary, tunneling measurements have been carried out on slightly overdoped $Bi_2Sr_2CaCu_2O_{8+x}$ single crystals below and above T_c by break-junctions and point-contacts. An anomaly was found in the tunneling $I(V)$ characteristics. Analysis of the data shows that the anomaly is caused by the superconducting condensate. The constant asymptotics of the $I(V)$ characteristic of the condensate, shown in Fig. 4f, are the fingerprints of the presence of one-dimensionality in Bi2212 [6]. The anomaly found here puts additional constraints on the final theory of high-T_c superconductivity.

I thank N. Miyakawa for sending the data from [5], Yu.I. Latyshev for sending unpublished data related to [13], and V.Z. Kresin for comments on the manuscript.

REFERENCES

1. J. G. Bednorz and K. A. Müller, Z. Phys. B **64**, 189 (1986).
2. J. Orenstein and A. J. Millis, Science **288**, 468 (2000).
3. A. V. Fedorov, T. Valla, P. D. Johnson, *et al.*, Phys. Rev. Lett. **82**, 2179 (1999).
4. G. E. Blonder, M. Tinkham, and T. M. Klapwijk, Phys. Rev. B **25**, 4515 (1982).
5. N. Miyakawa, P. Guptasarma, J. F. Zasadzinski, *et al.*, Phys. Rev. Lett. **80**, 157 (1998).
6. A. Mourachkine, Europhys. Lett. **55**, 559 (2001).
7. A. Mourachkine, Europhys. Lett. **49**, 86 (2000).
8. S. H. Pan, E. W. Hudson, A. K. Gupta, *et al.*, Phys. Rev. Lett. **85**, 1536 (2000).
9. Crossing T_c from above, the pseudogap undergoes a strong renormalization of quasiparticle excitations at low bias (see Fig. 3 in [3]).
10. A. S. Davydov, Phys. Rep. **190**, 191 (1990).
11. A. G. Sun, A. Truscott, A. S. Katz, *et al.*, Phys. Rev. B **54**, 6734 (1996).
12. T. Nachtrab, S. Heim, M. Mössle, *et al.*, Phys. Rev. B **65**, 012410 (2002).
13. Yu. I. Latyshev, A. A. Sinchenko, L. N. Bulaevskiĭ, *et al.*, Pis'ma Zh. Éksp. Teor. Fiz. **75**, 103 (2002) [JETP Lett. **75**, 93 (2002)].

JETP Letters, Vol. 77, No. 12, 2003, pp. 671–675. From Pis'ma v Zhurnal Éksperimental'noĭ i Teoreticheskoĭ Fiziki, Vol. 77, No. 12, 2003, pp. 803–807.

Quasiparticles in the Superconducting State of High-T_c Metals¶

M. Ya. Amusia[1, 2] and V. R. Shaginyan[1, 3]

[1] *Racah Institute of Physics, Hebrew University, Jerusalem, 91904, Israel*
[2] *Ioffe Physicotechnical Institute, St. Petersburg, 194021 Russia*
[3] *St. Petersburg Nuclear Physics Institute, Gatchina, 188300 Russia*
e-mail: vrshag@thd.pnpi.spb.ru

Received May 6, 2003

We consider the behavior of quasiparticles in the superconducting state of high-T_c metals within the framework of the theory of the superconducting state based on the fermion condensation quantum phase transition. We show that the behavior coincides with the behavior of Bogoliubov quasiparticles, whereas the maximum value of the superconducting gap and other exotic properties are determined by the presence of the fermion condensate. If at low temperatures the normal state is recovered by the application of a magnetic field suppressing the superconductivity, the induced state can be viewed as a Landau–Fermi liquid. These observations are in good agreement with recent experimental facts. © *2003 MAIK "Nauka/Interperiodica".*

PACS numbers: 74.20.-z; 74.25.Fy; 74.72.-h

The Landau–Fermi liquid (LFL) theory explains the major part of the low-temperature properties of Fermi liquids [1]. The LFL theory has demonstrated that the low-energy elementary excitations of a Fermi liquid look like the spectrum of an ideal Fermi gas and can be described in terms of Landau quasiparticles (LQ) with an effective mass M^*, charge e, and spin 1/2. As well, the LFL theory gives theoretical grounds for the BCS (Bardeen, Cooper, and Schrieffer) theory [2] of conventional superconductivity, which accounts for many of the fundamental properties of superconductors. In turn, the BCS theory is based on the notion of quasiparticles, which represent elementary excitations of a superconducting electron liquid and are called Bogoliubov quasiparticles (BQ). In the case of high-T_c metals, when the understanding of their striking behavior remains among the main problems of condensed matter physics, a number of primary ideas of the LFL theory and BCS theory have been called into question. Therefore, there exists a fundamental question as to whether or not a theory of high-T_c metals can be developed in terms of LQ and BQ.

It was reported recently that the full energy dispersion of single-particle excitations and the corresponding coherence factors as a function of momentum were measured on high-T_c cuprate $Bi_2Sr_2Ca_2Cu_3O_{10+\delta}$, T_c = 108 K) by using high-resolution angle-resolved photoemission spectroscopy [3]. All the observed features qualitatively and quantitatively agree with the behavior of BQ predicted from BCS theory. This observation suggests that the superconducting state of high-T_c cuprate is BCS-like and implies the basic validity of BCS formalism in describing the superconducting state [3]. On the other hand, such properties as the pairing mechanism, the maximum value of the superconducting gap Δ_1, the high density of states, and other exotic properties are beyond BCS theory.

Striking experimental facts on the transport properties of the normal state induced by applying a magnetic field greater than the upper critical field B_c were obtained in hole-doped cuprates at overdoped concentration ($Tl_2Ba_2CuO_{6+\delta}$) [4] and at optimal doping concentration ($Bi_2Sr_2CuO_{6+\delta}$) [5]. These data have clearly shown that there is no sizable violation of the Wiedemann–Franz (WF) law. Measurements for strongly overdoped nonsuperconducting $La_{1.7}Sr_{0.3}CuO_4$ have demonstrated that the resistivity ρ exhibits T^2 behavior, $\rho = \rho_0 + \Delta\rho$ with $\Delta\rho = AT^2$, and the WF law is verified to hold perfectly [6]. Since the validity of the WF law is a robust signature of LFL, these experimental facts demonstrate that the observed elementary excitations cannot be distinguished from LQ. Thus, these experimental observations impose strong constraints for models describing the electron liquid of the high-temperature superconductors. For example, in the cases of a Luttinger liquid [7], spin–charge separation (see, e.g., [8]), and, in some solutions of t–J model [9], a violation of the WF law, was predicted.

In this letter, we consider the superconducting state of high-T_c metals within the framework of the theory of the superconducting state based on the fermion condensation quantum phase transition (FCQPT) [10–12]. We show that the superconducting state is BCS-like, the

¶This article was submitted by the authors in English.

elementary excitations are BQ, and the primary ideas of the LFL theory and BCS theory are valid. At temperatures $T \longrightarrow 0$, the normal state recovered by the application of a magnetic field larger than the critical field B_c can be viewed as LFL induced by the magnetic field. In this state, the WF law is held and the elementary excitations are LQ.

At $T < T_c$, the thermodynamic potential Ω of an electron liquid is given by the equation (see, e.g., [13])

$$\Omega = E_{gs} - \mu N - TS, \quad (1)$$

where N is the number of particles, S denotes the entropy, and μ is the chemical potential. The ground-state energy $E_{gs}[k(\mathbf{p}), n(\mathbf{p})]$ of an electron liquid is a functional of the order parameter of the superconducting state $k(\mathbf{p})$ and of the quasiparticle occupation numbers $n(\mathbf{p})$. Here we assume that the electron system is two-dimensional, while all results can be transported to the case of the three-dimensional system. This energy is determined by the known equation of the weak-coupling theory of superconductivity

$$E_{gs} = E[n(\mathbf{p})] + \int \lambda_0 V(\mathbf{p}_1, \mathbf{p}_2) k(\mathbf{p}_1) k^*(\mathbf{p}_2) \frac{d\mathbf{p}_1 d\mathbf{p}_2}{(2\pi)^4}. \quad (2)$$

Here, $E[n(\mathbf{p})]$ is the Landau functional determining the ground-state energy of a normal Fermi liquid. The quasiparticle occupation numbers

$$n(\mathbf{p}) = v^2(\mathbf{p})(1 - f(\mathbf{p})) + u^2(\mathbf{p}) f(\mathbf{p}), \quad (3)$$

and

$$k(\mathbf{p}) = v(\mathbf{p}) u(\mathbf{p})(1 - 2 f(\mathbf{p})), \quad (4)$$

where the coherence factors $v(\mathbf{p})$ and $u(\mathbf{p})$ are obeyed the normalization condition

$$v^2(\mathbf{p}) + u^2(\mathbf{p}) = 1. \quad (5)$$

The distribution function $f(\mathbf{p})$ of BQ defines the entropy

$$S = -2\int [f(\mathbf{p}) \ln f(\mathbf{p}) + (1 - f(\mathbf{p})) \ln(1 - f(\mathbf{p}))] \frac{d\mathbf{p}}{4\pi^2}. \quad (6)$$

We assume that the pairing interaction $\lambda_0 V(\mathbf{p}_1, \mathbf{p}_2)$ is weak and is produced, for instance, by electron–phonon interaction. Minimizing Ω with respect to $\kappa(\mathbf{p})$ and using the definition $\Delta(\mathbf{p}) = -\delta\Omega/k(\mathbf{p})$, we obtain the equation connecting the single-particle energy $\varepsilon(\mathbf{p})$ to the superconducting gap $\Delta(\mathbf{p})$,

$$\varepsilon(\mathbf{p}) - \mu = \Delta(\mathbf{p}) \frac{1 - 2 v^2(\mathbf{p})}{2 v(\mathbf{p}) u(\mathbf{p})}. \quad (7)$$

The single-particle energy $\varepsilon(\mathbf{p})$ is determined by the Landau equation

$$\varepsilon(\mathbf{p}) = \frac{\delta E[n(\mathbf{p})]}{\delta n(\mathbf{p})}. \quad (8)$$

Note that $E[n(\mathbf{p})]$, $\varepsilon[n(\mathbf{p})]$, and the Landau amplitude

$$F_L(\mathbf{p}, \mathbf{p}_1) = \frac{\delta E^2[n(\mathbf{p})]}{\delta n(\mathbf{p}) \delta(\mathbf{p}_1)} \quad (9)$$

implicitly depend on the density x, which defines the strength of F_L. Minimizing Ω with respect to $f(\mathbf{p})$ and after some algebra, we obtain the equation for the superconducting gap $\Delta(\mathbf{p})$

$$\Delta(\mathbf{p}) = -\frac{1}{2}\int \lambda_0 V(\mathbf{p}, \mathbf{p}_1) \frac{\Delta(\mathbf{p}_1)}{E(\mathbf{p}_1)} (1 - 2 f(\mathbf{p})) \frac{d\mathbf{p}_1}{4\pi^2}. \quad (10)$$

Here, the excitation energy $E(\mathbf{p})$ of BQ is given by

$$E(\mathbf{p}) = \frac{\delta(E_{gs} - \mu N)}{\delta f(\mathbf{p})} = \sqrt{(\varepsilon(\mathbf{p}) - \mu)^2 + \Delta^2(\mathbf{p})}. \quad (11)$$

The coherence factors $v(\mathbf{p})$, $u(\mathbf{p})$ and the distribution function $f(\mathbf{p})$ are given by the ordinary relations

$$v^2(\mathbf{p}) = \frac{1}{2}\left(1 - \frac{\varepsilon(\mathbf{p}) - \mu}{E(\mathbf{p})}\right), \quad u^2(\mathbf{p}) = \frac{1}{2}\left(1 + \frac{\varepsilon(\mathbf{p}) - \mu}{E(\mathbf{p})}\right), \quad (12)$$

$$f(\mathbf{p}) = \frac{1}{1 + \exp(E(\mathbf{p})/T)}. \quad (13)$$

Equations (7)–(13) are the conventional equations of the BCS theory [2, 13], determining the superconducting state with BQ and the maximum value of the superconducting gap $\Delta_1 \sim 10^{-3}\varepsilon_F$ provided that one assumes that the system in question has not undergone FCQPT.

Now we turn to a consideration of a superconducting electron liquid with the fermion condensate (FC), which takes place after the FCQPT point. If $\lambda_0 \longrightarrow 0$, then the maximum value of the superconducting gap $\Delta_1 \longrightarrow 0$, as well as the critical temperature $T_c \longrightarrow 0$, and Eq. (7) reduces to the equation [10, 11, 14]

$$\varepsilon(\mathbf{p}) - \mu = 0, \text{ if } 0 < n(\mathbf{p}) < 1; \; p_i \le p \le p_f. \quad (14)$$

At $T \longrightarrow 0$, Eq. (14) defines a new state of electron liquid with FC [10, 15], which is characterized by a flat part of the spectrum in the $(p_f - p_i)$ region and has a strong impact on the system's properties up to temperature T_f [10, 11, 16]. Apparently, the momenta p_i and p_f have to satisfy $p_i < p_F < p_f$, where p_F is the Fermi momentum. When the Landau amplitude $F_L(p = p_F, p_1 = p_F)$ as a function of the density x is sufficiently small, the flat part vanishes, and at $T \longrightarrow 0$ Eq. (14) has only the trivial solution $\varepsilon(p = p_F) = \mu$, and the quasiparticle occupation numbers are given by the step function, $n(\mathbf{p}) = \theta(p_F - p)$ [10]. At some critical density $x = x_{FC}$, the amplitude becomes strong enough so that Eq. (14) possesses the solution corresponding to a formation of the flat part of spectrum; that is, FC is created [17, 18]. Note that a formation of the flat part of the spectrum has been recently confirmed in [19].

Now we can study the relationships between the state defined by Eq. (14) and the superconductivity. At $T \longrightarrow 0$, Eq. (14) defines a particular state of a Fermi liquid with FC, for which the modulus of the order parameter $|k(\mathbf{p})|$ has finite values in the $(p_f - p_i)$ region, whereas $\Delta_1 \longrightarrow 0$ in this region. Observe that $f(\mathbf{p}, T \longrightarrow 0) \longrightarrow 0$, and it follows from Eqs. (3) and (4) that if $0 < n(\mathbf{p}) < 1$ then $|k(\mathbf{p})| \neq 0$ in the region $(p_f - p_i)$. Such a state can be considered as superconducting, with an infinitely small value of Δ_1, so that the entropy of this state is equal to zero. It is obvious that this state, being driven by the quantum phase transition, disappears at $T > 0$ [11]. Any quantum phase transition that takes place at temperature $T = 0$ is determined by a control parameter other than temperature, for example, by pressure, by magnetic field, or by the density of mobile charge carriers x. The quantum phase transition occurs at a quantum critical point. At some density $x \longrightarrow x_{FC}$, when the Landau amplitude F_L becomes sufficiently weak and $p_i \longrightarrow p_F \longrightarrow p_f$, Eq. (14) determines the critical density x_{FC} at which FCQPT takes place, leading to the formation of FC [10, 11]. It follows from Eq. (14) that the system becomes divided into two quasiparticle subsystems: the first subsystem in the $(p_f - p_i)$ range is characterized by the quasiparticles with the effective mass $M^*_{FC} \propto 1/\Delta_1$, while the second one is occupied by quasiparticles with finite mass M^*_L and momenta $p < p_i$. The density of states near the Fermi level tends to infinity, $N(0) \propto M^*_{FC} \propto 1/\Delta_1$ [11].

If $\lambda_0 \neq 0$, then Δ_1 becomes finite. It is seen from Eq. (10) that the superconducting gap depends on the single-particle spectrum $\varepsilon(\mathbf{p})$. On the other hand, it follows from Eq. (7) that $\varepsilon(\mathbf{p})$ depends on $\Delta(\mathbf{p})$ provided that at $\Delta_1 \longrightarrow 0$ Eq. (14) has a solution determining the existence of FC. Let us assume that λ_0 is small so that the particle–particle interaction $\lambda_0 V(\mathbf{p}, \mathbf{p}_1)$can only lead to a small perturbation of the order parameter $k(\mathbf{p})$ determined by Eq. (14). Upon differentiation of both parts of Eq. (7) with respect to the momentum p, we find that the effective mass $M^*_{FC} = d\varepsilon(p)/dp|_{p = p_F}$ becomes finite [11],

$$M^*_{FC} \sim p_F \frac{p_f - p_i}{2\Delta_1}. \tag{15}$$

It follows from Eq. (15) that the effective mass and the density of states $N(0) \propto M^*_{FC} \propto 1/\Delta_1$ are finite and constant at $T < T_c$ [11, 14]. As a result, we are led to the conclusion that, in contrast to the conventional theory of superconductivity, the single-particle spectrum $\varepsilon(\mathbf{p})$ strongly depends on the superconducting gap, and we have to solve Eqs. (8) and (10) in a self-consistent way. On the other hand, let us assume that Eqs. (8) and (10) are solved, and the effective mass M^*_{FC} is determined. Now one can fix the dispersion $\varepsilon(\mathbf{p})$ by choosing the effective mass M^* of system in question equal to M^*_{FC} and then solve Eq. (10) as is done in the case of the conventional theory of superconductivity [2]. As a result, one observes that the superconducting state is characterized by BQ with the dispersion given by Eq. (11), the coherence factors v, u are given by Eq. (12), and the normalization condition (5) is held. We are led to the conclusion that the observed features agree with the behavior of BQ predicted from BCS theory. This observation suggests that the superconducting state with FC is BCS-like and implies the basic validity of BCS formalism in describing the superconducting state. It is exactly the case that was observed experimentally in high-T_c cuprate $Bi_2Sr_2Ca_2Cu_3O_{10+\delta}$ [3].

Consider other differences between the conventional superconducting state and the superconducting state with FC. We consider the case when $T_c \ll T_f$. This means that the order parameter $k(\mathbf{p})$ is slightly perturbed by the pairing interaction, because the particle–particle interaction $\lambda_0 V$ is small compared to the Landau amplitude F_L, and the order parameter $k(\mathbf{p})$ is governed mainly by F_L [10]. We can solve Eq. (10) analytically by taking the Bardeen–Cooper–Schrieffer approximation for the particle–particle interaction: $\lambda_0 V(\mathbf{p}, \mathbf{p}_1) = -\lambda_0$ if $|\varepsilon(\mathbf{p}) - \mu| \leq \omega_D$; i.e., the interaction is zero outside this region, with ω_D being the characteristic phonon energy. As a result, the maximum value of the superconducting gap is given by [14]

$$\begin{aligned}\Delta_1 &\simeq \frac{\lambda_0 p_F (p_f - p_F)}{2\pi} \ln(1 + \sqrt{2}) \\ &\simeq 2\beta\varepsilon_F \frac{p_f - p_F}{p_F} \ln(1 + \sqrt{2}).\end{aligned} \tag{16}$$

Here, the Fermi energy $\varepsilon_F = p_F^2/2M^*_L$, and the dimensionless coupling constant β is given by the relation $\beta = \lambda_0 M^*_L/2\pi$. Taking the usual values of β as $\beta \simeq 0.3$, and assuming $(p_f - p_F)/p_F \simeq 0.2$, we get from Eq. (16) a large value of $\Delta_1 \sim 0.1\varepsilon_F$, while for normal metals one has $\Delta_1 \sim 10^{-3}\varepsilon_F$. Now we determine the energy scale E_0 which defines the region occupied by quasiparticles with the effective mass M^*_{FC}

$$E_0 = \varepsilon(\mathbf{p}_f) - \varepsilon(\mathbf{p}_i) \simeq \frac{2(p_f - p_F)p_F}{M^*_{FC}} \simeq 2\Delta_1. \tag{17}$$

We have returned back to the Landau–Fermi liquid theory, since high-energy degrees of freedom are eliminated and the quasiparticles are introduced. The only difference between LFL, which serves as a basis when constructing the superconducting state, and Fermi liquid after FCQPT is that we have to expand the number of relevant low-energy degrees of freedom by introducing a new type of quasiparticle with the effective mass M^*_{FC} given by Eq. (15) and the energy scale E_0 given by Eq. (17). Therefore, the dispersion $\varepsilon(\mathbf{p})$ is characterized

by two effective masses M_L^* and M_{FC}^* and by the scale E_0, which define the low-temperature properties, including the line shape of quasiparticle excitations [11, 14], while the dispersion of BQ is given by Eq. (11). We note that both the effective mass M_{FC}^* and the scale E_0 are temperature-independent at $T < T_c$, where T_c is the critical temperature of the superconducting phase transition [14]. Obviously, we cannot directly relate these new LFL quasiparticle excitations with the quasiparticle excitations of an ideal Fermi gas, because the system in question has undergone FCQPT. Nonetheless, the main basis of the Landau–Fermi liquid theory survives FCQPT: the low-energy excitations of a strongly correlated liquid with FC are quasiparticles.

As was shown above, the properties of these new quasiparticles are closely related to the properties of the superconducting state. We may say that the quasiparticle system in the range $(p_f - p_i)$ becomes very "soft" and is to be considered as a strongly correlated liquid. On the other hand, the system's properties and dynamics are dominated by a strong collective effect having its origin in FCQPT and determined by the macroscopic number of quasiparticles in the range $(p_f - p_i)$. Such a system cannot be perturbed by the scattering of individual quasiparticles and has features of a "quantum protectorate" [11, 20, 21].

At $T_c < T$, the order parameter κ vanishes, and the behavior of the system in question can be viewed as the behavior of an anomalous electron Fermi liquid, or strongly correlated liquid, with the resistivity being a linear function of temperature, while the effective mass behaves as $M_{FC}^* \propto 1/T$ [11, 16]. Obviously, in this regime one observes strong deviations from the LFL behavior and cannot expect that the WF law will be held.

As any phase transition, FCQPT is related to the order parameter, which induces a broken symmetry. As we have seen, the order parameter is the superconducting order parameter $k(\mathbf{p})$, while Δ_1, being proportional to the coupling constant (see Eq. (16)), can be small. Therefore, the existence of such a state, that is, an electron liquid with FC, can be revealed experimentally, since the order parameter $k(\mathbf{p})$ is suppressed by the critical magnetic field B_c, when $B_c^2 \sim \Delta_1^2$. If the coupling constant $\lambda_0 \longrightarrow 0$, the weak critical magnetic field $B_c \longrightarrow 0$ will destroy the state with FC converting the strongly correlated Fermi liquid into LFL. In this case, the magnetic field plays the role of the control parameter determining the effective mass [22],

$$M_{FC}^* \propto \frac{1}{\sqrt{B}}. \tag{18}$$

Equation (18) shows that by applying a magnetic field B the system can be driven back into LFL with the effective mass M_{FC}^*, which is finite and independent of the temperature. This means that the low-temperature properties depend on the effective mass in accordance with the LFL theory. At $T > T^*$, the system possesses the behavior of a strongly correlated liquid. Here, $T^* \propto \sqrt{B}$ is the temperature at which the transition from LFL to the strongly correlated liquid takes place. Such behavior was observed experimentally in the heavy-electron metal $YbRh_2Si_2$ [23]. If λ_0 is finite, the critical field is also finite, and Eq. (18) is valid at $B > B_c$. In that case, the effective mass M_{FC}^* is finite and temperature-independent at $T < T_c$, and low-temperature elementary excitations of the system can be described in terms of LQ. Thus, the system is driven back to LFL and has the LFL behavior induced by the magnetic field at least at $T < T_c$, while the low-energy elementary excitations are characterized by M_{FC}^* and cannot be distinguished from LQ. As a result, at $T \longrightarrow 0$, the WF law is held in accordance with experimental facts [4, 5].

The existence of FCQPT can also be revealed experimentally, because at densities $x > x_{FC}$, or beyond the FCQPT point, the system should be LFL at sufficiently low temperatures [18]. Recent experimental data have shown that this liquid exists in heavily overdoped nonsuperconducting $La_{1.7}Sr_{0.3}CuO_4$ [6]. It is remarkable that, up to $T = 55$ K, the resistivity exhibits the T^2 behavior and the WF law is verified to within the experimental resolution [6].

In summary, we have shown that the superconducting state with FC is characterized by BQ. The behavior of these BQ agrees with the behavior of BQ predicted from BCS theory and suggests that the superconducting state with FC is BCS-like and implies the basic validity of BCS formalism in describing the superconducting state, although the maximum value of the superconducting gap and other exotic properties are determined by the presence of the fermion condensate. We have also demonstrated that the low-temperature transport properties of high-T_c metals observed in optimally doped and overdoped cuprates by the application of a magnetic field higher than the critical field can be explained within the framework of the fermion condensation theory of high-T_c superconductivity. The quasiparticles are LQ and the WF law is held. The recent experimental observations of BQ in the superconducting state and verifications of the WF law in heavily overdoped, overdoped, and optimally doped cuprates clearly favor the existence of FC in high-T_c metals.

M.Ya.A. is grateful to the Hebrew University Intramural Fund of the Hebrew University for financial support. V.R.Sh. is grateful to the Racah Institute of Physics for the hospitality during his stay in Jerusalem. This work was supported in part by the Russian Foundation for Basic Research, project no. 01-02-17189.

REFERENCES

1. L. D. Landau, Zh. Éksp. Teor. Fiz. **30**, 1058 (1956) [Sov. Phys. JETP **3**, 920 (1956)].
2. J. Bardeen, L. N. Cooper, and J. R. Schriffer, Phys. Rev. **108**, 1175 (1957).
3. H. Matsui *et al.*, Phys. Rev. Lett. (in press); cond-mat/0304505.
4. C. Proust, E. Boaknin, R. W. Hill, *et al.*, Phys. Rev. Lett. **89**, 147003 (2002).
5. R. Bel *et al.*, cond-mat/0304111.
6. S. Nakamae *et al.*, cond-mat/0212283.
7. C. L. Kane and M. P. A. Fisher, Phys. Rev. Lett. **76**, 3192 (1996).
8. T. Senthil and M. P. A. Fisher, Phys. Rev. B **62**, 7850 (2000).
9. A. Houghton, S. Lee, and J. P. Marston, Phys. Rev. B **65**, 220503 (2002).
10. V. A. Khodel and V. R. Shaginyan, Pis'ma Zh. Éksp. Teor. Fiz. **51**, 488 (1990) [JETP Lett. **51**, 553 (1990)]; V. A. Khodel, V. R. Shaginyan, and V. V. Khodel, Phys. Rep. **249**, 1 (1994).
11. M. Ya. Amusia and V. R. Shaginyan, Phys. Rev. B **63**, 224507 (2001).
12. M. Ya. Amusia and V. R. Shaginyan, JETP Lett. **76**, 651 (2002).
13. D. R. Tilley and J. Tilley, *Superfluidity and Superconductivity*, 2nd ed. (Adam Higler, Bristol and New York, 1986); P. G. De Gennes, *Superconductivity of Metals and Alloys* (Benjamin, New York, 1966; Mir, Moscow, 1968).
14. M. Ya. Amusia, S. A. Artamonov, and V. R. Shaginyan, Pis'ma Zh. Éksp. Teor. Fiz. **74**, 435 (2001) [JETP Lett. **74**, 396 (2001)]; V. R. Shaginyan, Physica B & C (Amsterdam) **312–313**, 413 (2002).
15. G. E. Volovik, Pis'ma Zh. Éksp. Teor. Fiz. **53**, 208 (1991) [JETP Lett. **53**, 222 (1991)].
16. J. Dukelsky, V. A. Khodel, P. Schuck, and V. R. Shaginyan, Z. Phys. B **102**, 245 (1997).
17. V. A. Khodel, V. R. Shaginyan, and M. V. Zverev, Pis'ma Zh. Éksp. Teor. Fiz. **65**, 242 (1997) [JETP Lett. **65**, 253 (1997)].
18. V. R. Shaginyan, JETP Lett. **77**, 99 (2003).
19. I. E. Dzyaloshinskii, J. Phys. I (France) **6**, 119 (1996); V. Yu. Irkhin, A. A. Katanin, and M. I. Katsnelson, Phys. Rev. Lett. **89**, 076401 (2002).
20. R. B. Laughlin and D. Pines, Proc. Natl. Acad. Sci. USA **97**, 28 (2000).
21. P. W. Anderson, cond-mat/0007185; cond-mat/0007287.
22. Yu. G. Pogorelov and V. R. Shaginyan, Pis'ma Zh. Éksp. Teor. Fiz. **76**, 614 (2002) [JETP Lett. **76**, 532 (2002)].
23. P. Gegenwart, J. Custers, C. Geibel, *et al.*, Phys. Rev. Lett. **89**, 056402 (2002).

JETP Letters, Vol. 77, No. 12, 2003, pp. 676–679. Translated from Pis'ma v Zhurnal Éksperimental'noĭ i Teoreticheskoĭ Fiziki, Vol. 77, No. 12, 2003, pp. 808–811.

Many-Electron Model of Band Structure and Metal–Insulator Transition under Pressure in $FeBO_3$

S. G. Ovchinnikov

Institute of Physics, Siberian Division, Russian Academy of Sciences, Krasnoyarsk, 660036 Russia

e-mail: sgo@iph.krasn.ru

Received May 5, 2003; in final form, May 19, 2003

A many-electron model is proposed for the band structure of $FeBO_3$ with regard to strong electron correlations in the d^4, d^5, and d^6 configurations. Under normal conditions, $FeBO_3$ is characterized by a dielectric charge-transfer gap in the strong correlation regime $U \gg W$. With increasing pressure, not only does the d-band W width grow but simultaneously the effective Hubbard parameter U_{eff} sharply drops, which is due to the crossover of high-spin and low-spin ground state terms of the Fe^{2+}, Fe^{3+}, and Fe^{4+} ions. It is predicted that a transition from the semiconducting antiferromagnetic state to the metallic paramagnetic state will occur in the high-pressure phase with increasing temperature. © *2003 MAIK "Nauka/Interperiodica".*

PACS numbers: 71.20.-b; 71.30.+h; 71.15.-m

1. A first-order phase transition from the magnetic to nonmagnetic state of $FeBO_3$ was observed at the pressure $P_c = 46$ GPa in a series of recent works [1–3]. This transition was accompanied by the structural transition with a 8.6% decrease in volume. A number of indirect data point to the metallization of the system at $P > P_c$; however, no ultimate clarity in the problem of magnetic and electric properties in the high-pressure phase has been achieved so far. From the general point of view, the metallization and the disappearance of localized magnetic moments with increasing pressure are not surprising, because the bandwidth W increases and the Mott–Hubbard insulator with $U \gg W$ transforms to the metallic state with $U < W$ [4]. However, in the case of $FeBO_3$, as in many other real substances, the simple picture based on the Hubbard model becomes complicated because of the presence of a great number of $d(f)$ orbitals.

In this work, a many-electron model is proposed that takes into account all d orbitals and the strong electron correlations of d electrons. The energies of both high-spin and various low-spin terms of the Fe^{2+}, Fe^{3+}, and Fe^{4+} ions were calculated. It turned out that the electron system under normal conditions occurs in the strong electron correlation regime with a dielectric charge-transfer gap, as classified in [5]. As the pressure grows, not only does the band width W change but the splitting of the e_g and t_{2g} electrons in the crystal field Δ increases as well. It is the growth of Δ that is responsible for the crossover of the high-spin ${}^6A_{1g}$ ($S = 5/2$) and low-spin ${}^2T_{2g}$ ($S = 1/2$) terms of Fe^{3+} and high-spin and low-spin terms of Fe^{2+} and Fe^{4+}. As a result, not only does the collapse of the magnetic moment take place, as was found in [1–3], but a rearrangement of the diagram of the $d^5 \longrightarrow d^4$ and $d^5 \longrightarrow d^6$ excitations takes place as well, so that the effective Hubbard parameter $U_{\text{eff}} = E(d^6) + E(d^4) - 2E(d^5)$ sharply decreases. In this fact, we see the nontrivial feature of the phase transition in $FeBO_3$ under pressure.

2. The first-principles one-electron band-structure calculations of $FeBO_3$ by density functional methods in the local-density approximation [6] and in the generalized gradient approximation [7] and also the molecular orbital calculation of the FeB_6O_6 cluster [8] revealed the following pattern of the electronic structure of $FeBO_3$. The empty conduction band ε_c is mainly formed by the boron s and p states, the valence band top ε_v is mainly formed by the oxygen s and p states, and the band gap between them E_{g0} in the antiferromagnetic phase is 2.5 eV [6], which is sufficiently close to an optical absorption edge of 2.9 eV [9]. The d-electron band lies close to the valence band top with the width $2W_d \approx 2.8$ eV and the crystal-field parameter $\Delta \approx 1$ eV [6]. The hybridization of Fe d electrons with O s and p electrons is very small [6, 8], much smaller than in 3d-metal oxides. This is due to a very strong hybridization inside the BO_3 group; in fact, the $(BO_3)^{3-}$ ion is formed, and the oxygen orbitals are closed on boron, which determines the smallness of p–d hybridization. This circumstance significantly simplifies the many-electron model, because one may calculate the d^n ($n = 4$, 5, and 6) terms of iron in the crystal field rather than the terms of the metal–oxygen complex, as in copper oxides [10].

The intraatomic part of the d-electron Hamiltonian can be written as

$$H_{am} = \sum_{\lambda\sigma}\left(\varepsilon_\lambda n_{\lambda\sigma} + \frac{U_\lambda}{2} n_{\lambda\sigma} n_{\lambda\bar{\sigma}}\right) + \sum_{\lambda,\lambda'}\sum_{\sigma,\sigma'}\left(V_{\lambda\lambda'} n_{\lambda\sigma} n_{\lambda'\sigma'} - J_{\lambda\lambda'} a^+_{\lambda\sigma} a_{\lambda\sigma'} a^+_{\lambda'\sigma'} a_{\lambda'\sigma}\right), \quad (1)$$

0021-3640/03/7712-0676$24.00

where $n_{\lambda\sigma} = a^{+}_{\lambda\sigma} a_{\lambda\sigma}$, $a_{\lambda\sigma}$ designates the creation operator of a d electron on one of the five orbitals λ with the spin projection σ, $\bar{\sigma} = -\sigma$. The first term describes the atomic d levels in the crystal field, the small uniaxial crystal-field component is neglected, and it is assumed that $\varepsilon(t_{2g}) = \varepsilon_d - 2\Delta/5$ and $\varepsilon(e_g) = \varepsilon_d + 3\Delta/5$. The other terms in Eq. (1) correspond to the Coulomb intraorbital U_λ and interorbital $V_{\lambda\lambda'}$ repulsions and also to the Hund exchange $J_{\lambda\lambda'}$. For the sake of simplicity, we will neglect the orbital dependence of the Coulomb matrix elements considering that there are three parameters U, V, and J related to each other by the known condition $U = 2V + J$.

The energies $E_S(d^n)$ of the lowest levels of the d^n configuration with spin S equal

$$\begin{aligned}
E_2(d^4) &= 4\varepsilon_d - 3\Delta/5 + 6V - 6J,\\
E_1(d^4) &= 4\varepsilon_d - 8\Delta/5 + U + 5V - 3J,\\
E_0(d^4) &= 4\varepsilon_d - 8\Delta/5 + 2U + 5V - 2J,\\
E_{5/2}(d^5) &= 5\varepsilon_d + 10V - 10J,\\
E_{3/2}(d^5) &= 5\varepsilon_d - \Delta + U + 9V - 6J,\\
E_{1/2}(d^5) &= 5\varepsilon_d - 2\Delta + 2U + 8V - 4J,\\
E_2(d^6) &= 6\varepsilon_d - 2\Delta/5 + U + 14V - 10J,\\
E_1(d^6) &= 6\varepsilon_d - 7\Delta/5 + 2U + 13V - 7J,\\
E_0(d^6) &= 6\varepsilon_d - 12\Delta/5 + 3U + 12V - 6J.
\end{aligned} \tag{2}$$

The one-electron Green's function without regard for interatomic hopping is calculated exactly with the use of the Hubbard X operators $X^{pq} = |p\rangle\langle q|$ constructed on the eigenstates $|q\rangle$ (Eq. (2). Such functions were calculated for the metals of the iron group in the limit $U \longrightarrow \infty$ in the works [11, 12]. In this case, the energy of the d-electron quasiparticles is determined not by the many-electron terms themselves but by their differences

$$\Omega_{ij} = E_i(d^{n+1}) - E_j(d^n). \tag{3}$$

It is these energies that determine the one-electron band structure of the substance along with the s- and p-electron bands of boron and oxygen. As distinct from the ordinary band states, the quasiparticles specified by Eq. (3) have a variable spectral weight determined by the filling factors $F_{ij} = N_i(d^{n+1}) + N_j(d^n)$, where $N_j(d^n)$ is the filling probability of the ith term of the d^n configuration. This probability is calculated self-consistently through the equation for the chemical potential [11–13].

3. In order to relate the quasiparticle energies (3) to the conduction and valence bands, we will make use of the results of the calculation [6], according to which the valence-band top ε_v coincides with that of the one-electron d band. Thus, we obtain the condition $\varepsilon_v = \varepsilon_d + W_d$. The U and J parameters are found by a comparison of the energies $\Delta E_1 = E_{3/2}(d^5) - E_{5/2}(d^5)$ and with $\Delta E_2 = E_{1/2}(d^5) - E_{5/2}(d^5)$ with exciton peaks at 1.3 and 1.9 eV in the absorption spectra [14]. As a result, we found $U =$ 1.45 eV and $J = 0.35$ eV and calculated the energies of all terms given in Eq. (2) (Fig. 1). It is evident in Fig. 1 that, of all the intraatomic d quasiparticles, the transitions $\Omega_v = E_{5/2}(d^5) - E_2(d^4)$, $\Omega'_v = E_{5/2}(d^5) - E_1(d^4)$, and $\Omega''_v = E_{5/2}(d^5) - E_0(d^4)$ with electron annihilation and also $\Omega_c = E_2(d^6) - E_{5/2}(d^5)$, $\Omega'_c = E_1(d^6) - E_{5/2}(d^5)$, and $\Omega''_c = E_0(d^6) - E_{5/2}(d^5)$ with electron creation have a nonzero weight. All Ω_v energies were found to be lower than the valence band top, and Ω_c fell within the gap E_{g0} (Fig. 2). The Ω_c and Ω_v energies are the centroids of the upper and lower Hubbard bands, which are formed if the d–d hoppings t are subsequently taken into account. The effective parameter

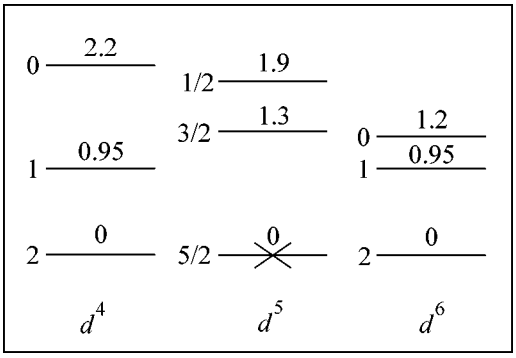

Fig. 1. Diagram of Fe^{4+}, Fe^{3+}, and Fe^{2+} terms; the cross marks the lowest ${}^6A_{1g}$ term filled at $T = 0$. The numbers on the left indicate the spin, and the numbers above indicate the energy (eV) of the term relative to the lowest term for each configuration.

$$\begin{aligned}
U_{\text{eff}} &= \Omega_c - \Omega_v = E_2(d^6) + E_2(d^4) - 2E_{5/2}(d^5)\\
&= U + 4J - \Delta = 1.85 \text{ eV}.
\end{aligned} \tag{4}$$

The interatomic hopping in the antiferromagnetic phase is suppressed because of the spin–polaron effect [15]. In the case of hopping between nearest neighbors, the effective hopping integral is determined by the product of the filling factors on two sites belonging to the opposite sublattices A and B [16]. Thus, for the lower Hubbard band, we obtain

$$\begin{aligned}
t_v^2 &= t^2(\langle X_A^{+5/2,+5/2}\rangle + \langle X_A^{+2,+2}\rangle)\\
&\times(\langle X_B^{+5/2,+5/2}\rangle + \langle X_B^{+2,+2}\rangle),
\end{aligned} \tag{5}$$

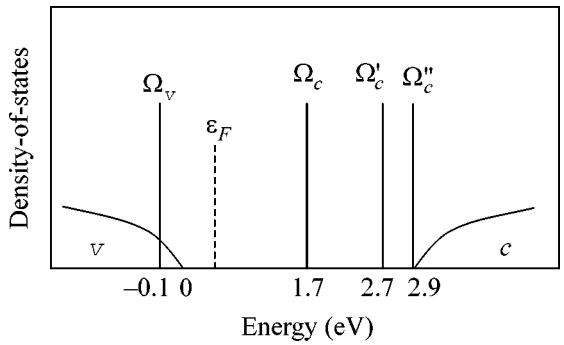

Fig. 2. Diagram of the density of states of $FeBO_3$ at normal pressure in the antiferromagnetic phase.

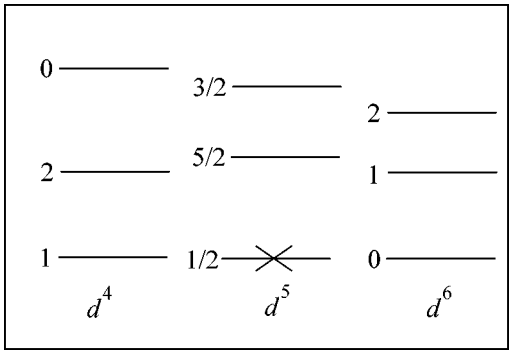

Fig. 3. Diagram of the Fe^{4+}, Fe^{3+}, and Fe^{2+} terms in the high-pressure phase.

where $|+5/2\rangle$ and $|+2\rangle$ are spin sublevels of the $E_{5/2}(d^5)$ and $E_2(d^4)$ terms split in the internal molecular field according to their spin projections. If level $|+5/2\rangle$ is the lowest for sublattice *A* and is filled, then the lowest level for sublattice *B* $|-5/2\rangle$ is unfilled at $T = 0$ (with neglect of the zero quantum functions). Therefore, $\langle X_B^{+5/2,\,+5/2}\rangle = 0$ at $T = 0$, the occupation numbers of all d^4 and d^6 sublevels also equal zero for $FeBO_3$, so that the widths of the Hubbard bands are close to zero. This is why the diagram of density of states in Fig. 2 can be compared with the experiment in the antiferromagnetic phase of $FeBO_3$. Note that, according to this diagram, $FeBO_3$ belongs to the class of dielectrics with a gap caused by the charge-transfer processes. In this case, we consider that a hole with the energy ε_v is created on oxygen and a *d* electron with the energy Ω_c is created on iron ($d^5p^6 \longrightarrow d^6p^5$ process).

4. As pressure is built up, the crystal-field parameters Δ and the interatomic hopping *t* increase. The latter, as we can see from Eq. (4), only slightly affects the band structure in the antiferromagnetic phase. The growth of Δ is more important and leads to the crossover of high-spin and low-spin terms. It is evident from Eq. (2) that, as Δ increases, the $E_{1/2}(d^5)$ term goes down more rapidly than the $E_{3/2}(d^5)$ term; therefore, the crossover with spin 5/2 takes place for $S = 1/2$. It is this crossover that was observed by the Mössbauer effect in [1–3]. We do not study here the thermodynamics of the system under pressure. This was made in first principles calculations [7]. We are interested in understanding how the crossover is manifested in the electronic structure. Thus, we will consider the high-pressure (HP) phase $P > P_c$, in which $\Delta(P) > \Delta_c = (U + 7J)/2$. The crossover of terms $S = 2$ and $S = 1$ for the d^4 configuration also takes place at this pressure, and the crossover of terms $S = 2$ and $S = 0$ for the d^6 configuration takes place even earlier (at lower pressure). The schematic diagram of many-electron levels in the HP phase is shown in Fig. 3. The rearrangement of all terms leads to a change in the effective Hubbard parameter in the HP phase

$$\begin{aligned}\tilde{U}_{\text{eff}} &= E_1(d^4) + E_0(d^6) - 2E_{1/2}(d^5)\\ &= (U - 3J)/2 = 0.2\ \text{eV},\end{aligned} \tag{6}$$

so that, along with the growth of the bandwidth, the importance of strong correlations decreases, and we expect the metallization of the system in the paramagnetic phase. Because we do not know the width of the *d* band, we may speak with confidence only about a tendency toward metallization. Consider two possible variants.

(1) As the band width, we take the result of the band-structure calculation with $W_d = 1.4$ eV. Then, at $U_{\text{eff}} = 0.2$ eV, we expect the metallic paramagnetic state. If the system is characterized by Fermi surface nesting, it will transform into a spin-density-wave state (band ferromagnet) [17–19] with decreasing temperature below

$$T_N = 1.14W_d \exp\left(-\frac{1}{N(\varepsilon_F)U_{\text{eff}}}\right), \tag{7}$$

where $N(\varepsilon_F) \sim 1/W_d$ is the density of states at the Fermi level. The electrical properties below T_N are characterized by a dielectric gap $E_g = 2U_{\text{eff}}\langle S^z\rangle$. Assuming that, at $T = 0$, $\langle S^z\rangle = 1/2$ in the HP phase, we obtain $E_g = 0.2$ eV. For T_N, at $U_{\text{eff}} = 0.2$ eV and $W_d = 1.4$ eV, we obtain the estimate $T_N = 10$ K from Eq. (7).

(2) It is possible that the *d* band is narrower than the overall bandwidth and than U_{eff}. Then the system in the HP phase will remain a Mott–Hubbard insulator and will transform into the metallic state with further growth of the pressure. For the Mott–Hubbard insulator, T_N can be roughly estimated within the effective Heisenberg model with $S = 1/2$. This model in the spin-wave approximation gives [20]

$$T_N = I(0)S(S + 1)/3C, \tag{8}$$

where *C* is the Watson integral and $I(0)$ is the Fourier transform of the interatomic exchange interaction. If

$I(0)$ did not depend on the pressure, T_N in the HP phase would be lower than T_N at $P = 0$ by a factor of 35/3. However, as the interatomic distance decreases, $I(0)$ grows. According to [3], the growth is linear, and $T_N \approx$ 600 K in the vicinity of P_c (at $P = 0$, $T_N = 348$ K). With regard to the increase in the exchange interaction, we obtain the estimate $T_N \approx 50$ K for the HP phase. The electronic structure of a Mott–Hubbard insulator is characterized by the existence of local levels $\tilde{\Omega}_v = E_{1/2}(d^5) - E_1(d^4)$ (filled) and $\tilde{\Omega}_c = E_0(d^6) - E_{1/2}(d^5)$ (empty at $T = 0$) and by the dielectric ground state with the gap $E_g \sim U_{\text{eff}}$.

Thus, both considered variants lead to the conclusion that the HP phase is characterized by a dielectric antiferromagnetic ground state with the gap $E_g =$ 0.2 eV. Both variants give values of T_N that are consistent with each other by the order of magnitude. The distinctions appear above T_N: the metal–insulator transition in the first variant and a semiconductor that transforms into a metal upon further buildup of the pressure, in the second variant. It is necessary to note that all quantitative estimates for the HP phase (for Δ_c, U_{eff}, and T_N values) should be considered as being qualitative, by the order of magnitude, rather than quantitative. Thus, the growth of the pressure will undoubtedly result in an increase in the uniaxial component of the crystal field, which will lead to further splitting of the e_g and t_{2g} states. Hence, the energies of all terms can change by a value comparable to Δ. Nevertheless, it is unlikely that the qualitative conclusion that U_{eff} significantly decreases upon the inversion of high-spin and low-spin terms will change if the model is refined. The conclusion that antiferromagnetism is retained in the HP phase, but with a lowered magnetic moment of the sublattice, was also obtained in [7]. In this work, the conclusion is drawn that the ground state is metallic at $P > P_c$. The interplay between the electrical and magnetic properties in the HP phase calls for further, primarily experimental investigation.

5. In conclusion, we note that the proposed model of the $FeBO_3$ band structure takes into account strong electron correlations and describes the optical absorption spectrum. The main mechanism of the change of the electronic structure with pressure is the increase in the crystal field, which leads to the inversion of high-spin and low-spin terms for the d^4, d^5, and d^6 configurations. An unusual mechanism of the transition from the strong correlation regime to the regime of weak correlation is revealed. This mechanism involves a decrease in the effective Hubbard parameter along with the usual growth of the band width.

I am grateful to I.S. Édel'man for the discussion of the results and to K. Parlinskiĭ and V. Sarkisyan, who sent some unpublished results.

This work was supported by the Russian Foundation for Basic Research, project no. 03-02-16286, and by the program of the Division of Physical Sciences of the Russian Academy of Sciences "Strongly Correlated Electrons."

REFERENCES

1. I. A. Troyan, A. G. Gavrilyuk, V. A. Sarkisyan, *et al.*, Pis'ma Zh. Éksp. Teor. Fiz. **74**, 26 (2001) [JETP Lett. **74**, 24 (2001)].
2. A. G. Gavriliuk, I. A. Trojan, R. Boehler, *et al.*, Pis'ma Zh. Éksp. Teor. Fiz. **75**, 25 (2002) [JETP Lett. **75**, 23 (2002)].
3. V. A. Sarkisyan, I. A. Troyan, I. S. Lyubutin, *et al.*, Pis'ma Zh. Éksp. Teor. Fiz. **76**, 788 (2002) [JETP Lett. **76**, 664 (2002)].
4. N. F. Mott, *Metal–Insulator Transitions* (Taylor and Fransic, London, 1974; Nauka, Moscow, 1979).
5. J. Zaanen, G. A. Sawatzky, and J. W. Allen, Phys. Rev. Lett. **55**, 418 (1985).
6. A. V. Postnikov, St. Bartkowski, M. Neumann, *et al.*, Phys. Rev. B **50**, 14849 (1994).
7. K. Parlinski, Eur. Phys. J. B **27**, 283 (2002).
8. N. B. Ivanova, V. V. Rudenko, A. D. Balaev, *et al.*, Zh. Éksp. Teor. Fiz. **21**, 354 (2002) [JETP **94**, 299 (2002)].
9. I. S. Édel'man, A. V. Malakhovskiĭ, T. I. Vasil'eva, and V. N. Seleznev, Fiz. Tverd. Tela (Leningrad) **14**, 2810 (1972) [Sov. Phys. Solid State **14**, 2442 (1972)].
10. V. A. Gavrichkov, S. G. Ovchinnikov, A. A. Borisov, and E. G. Goryachev, Zh. Éksp. Teor. Fiz. **118**, 422 (2000) [JETP **91**, 369 (2000)].
11. R. O. Zaĭtsev, Pis'ma Zh. Éksp. Teor. Fiz. **65**, 881 (1997) [JETP Lett. **65**, 925 (1997)].
12. R. O. Zaĭtsev, Pis'ma Zh. Éksp. Teor. Fiz. **72**, 109 (2000) [JETP Lett. **72**, 77 (2000)].
13. V. V. Val'kov and S. G. Ovchinnikov, *Quasiparticles in Strongly Correlated Systems* (Sib. Otd. Ross. Akad. Nauk, Novosibirsk, 2001).
14. V. N. Zabluda, A. V. Malakhovskiĭ, and I. S. Édel'man, Fiz. Tverd. Tela (Leningrad) **27**, 133 (1985) [Sov. Phys. Solid State **27**, 77 (1985)].
15. É. L. Nagaev, *Physics of Magnetic Semiconductors* (Nauka, Moscow, 1979).
16. S. G. Ovchinnikov, Zh. Éksp. Teor. Fiz. **107**, 796 (1995) [JETP **80**, 451 (1995)].
17. J. C. Slater, Phys. Rev. **82**, 538 (1951).
18. I. A. Kozlov and L. A. Maksimov, Zh. Éksp. Teor. Fiz. **48**, 1184 (1965) [Sov. Phys. JETP **21**, 790 (1965)].
19. Yu. V. Kopaev, Tr. Fiz. Inst. im. P.N. Lebedeva, Akad. Nauk SSSR **86**, 3 (1975).
20. S. V. Tyablikov, *Methods in the Quantum Theory of Magnetism*, 2nd ed. (Nauka, Moscow, 1975; Plenum, New York, 1967).

Translated by A. Bagatur'yants

JETP Letters, Vol. 77, No. 12, 2003, pp. 680–683. Translated from Pis'ma v Zhurnal Éksperimental'noĭ i Teoreticheskoĭ Fiziki, Vol. 77, No. 12, 2003, pp. 812–817.

Magnetic Resonance of the $RbMnBr_3$ Antiferromagnet under Pressure

L. A. Prozorova, S. S. Sosin*, and S. V. Petrov

Kapitza Institute for Physical Problems, Russian Academy of Sciences, ul. Kosygina 2, Moscow, 117334 Russia

**e-mail: sosin@kapitza.ras.ru*

Received May 29, 2003

The antiferromagnetic resonance spectrum was experimentally studied for a noncollinear $RbMnBr_3$ antiferromagnet under a mechanical pressure applied to the sample in various directions. It is shown that the incommensurate magnetic phase existing in the initial system in the presence of regular crystallographic distortions is sensitive to the pressure applied along one of the sample axes. The critical transition field to the commensurate phase decreased under pressure. It was also found that the pressure influences the uniaxial anisotropy appearing in the crystal basal plane in the presence of orthorhombic distortions. These effects were analyzed with allowance for the domain structure of the sample. © *2003 MAIK "Nauka/Interperiodica".*

PACS numbers: 76.50.+g; 75.50.Ee

In recent years, the crystal and magnetic properties of the $RbMnBr_3$ compound have been intensively studied because of the discovery of an ordered helical state in it that is incommensurate with the crystal lattice spacing at low temperatures. The origin of this state is in the periodical modulation of exchange interaction in the presence of small distortions of a trigonal lattice.

The compound of interest belongs to the ABX_3 type and crystallizes into the simple hexagonal structure with the $P6_3/mmc$ space group (unit-cell parameters a and c). The magnetic ions inside the face-shared halogen octahedra form a chain along the sixfold axis C_6 and a trigonal lattice in the basal plane perpendicular to this axis. In this case, the in-plane exchange interactions of magnetic ions prove to be the same and much weaker than the intrachain exchange ($J' \ll J$).

At room temperature, the crystal lattice of $RbMnBr_3$ is hexagonal with unit-cell sizes $\sqrt{3} \times \sqrt{3}$ times greater in the basal plane (space group $P6_3cm$ [1]). This structure appears due to the second-order phase transition resulting in the periodic displacement of one third of the magnetic ions, together with their halogen environment, along the C_6 axis. Lattice distortions of this type give rise to a "honeycomb" modulation of exchange interaction in the hexagonal plane, as shown in Fig. 1a.

On further cooling to T_c = 220 K, one more phase transition (of the first kind) is observed in $RbMnBr_3$. X-ray studies suggest that the crystal lattice in the low-temperature phase is orthorhombic, while the rectangular unit cell is four times larger than the initial cell and has the sizes $2a \times \sqrt{3}\,a \times c$. In [2], it was assumed that, after the second phase transition, the periodic displacement of magnetic atoms is rearranged and a possible structure was proposed which corresponded qualitatively to the above-mentioned parameters.

However, the structure factor suggested in [2] for the lattice basis did not explain the systematic absence of some reflections in the X-ray diffraction patterns. In recent work [3], a new variant of periodic displacements is discussed (zig-zag chains of ions shifted alternately upward and downward; Fig. 1b), which completely satisfies the experimental data. The exchange interaction between the ion spins in the zig-zags is stronger than between the zig-zags.

Below T_N = 8.5 K, a zero-field incommensurate antiferromagnetic magnetic structure is observed in $RbMnBr_3$. It shows magnetic Bragg peaks at wave vectors $\mathbf{Q} = (h/8 + \xi, h/8 + \xi, l)$ in units of the initial reciprocal lattice, where h and l are integers and $\xi = 0.0183 \pm 0.0004$ [4]. A strong magnetic crystal anisotropy holds spins in the basal plane. The existence of incommensu-

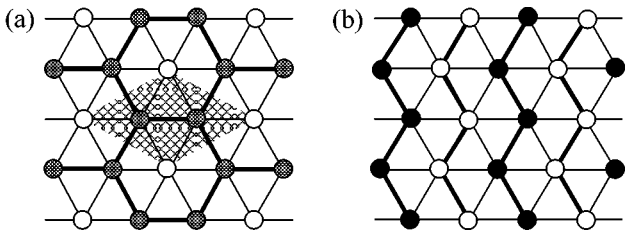

Fig. 1. Two types of distortion of the ideal hexagonal crystal lattice. Magnetic ions situating in the basal plane or shifted upward and downward from it are shown, correspondingly, by the gray, white, and black circles; the strong exchange spin interactions of magnetic ions are shown by the heavy lines.

rability is explained by the low symmetry of a distorted crystal structure allowing the Lifshitz invariant (of an exchange nature). This problem can also be considered within the framework of the microscopic row model [5], which explains the incommensurability by the above-mentioned modulation of exchange interaction. In a magnetic field lying in the basal plane, the incommensurate magnetic structure becomes unfavorable, and the first-order transition to a noncollinear commensurate phase ($\xi = 0$) occurs at a certain field $H^* \simeq 29$ kOe. The magnitude of this field is related to the relative in-plane exchange variation $\delta = (J_1'/J' - 1)$ by the expression $H^* = H_e\sqrt[3]{\pi|\delta|}$, where $H_e = 4S\sqrt{J(J_1' + 2J')}$ is the field of spin collapse into the collinear phase [6]. The period of commensurate magnetic structure corresponds to the quadruple period of the orthorhombic lattice along the zig-zag and to the double period in the perpendicular direction [3]. This is consistent with the experiment [7], where the noncollinear phase showed four $^{2+}$Mn NMR branches that, ordinarily, correspond to the presence of eight sublattices in the spin system.

The interconnection between the crystallographic distortions and the incommensurability in $RbMnBr_3$ can be checked experimentally by studying its magnetic properties under the conditions of uniaxial compression of a sample of this compound. The pressure will distort its crystal structure in a certain direction, thereby changing the ratio between the exchange interactions in the basal plane. Antiferromagnetic resonance (AFMR) provides one way to observe the incommensurability. In the AFMR spectra of incommensurate magnets (see [6]), the resonance absorption at frequencies corresponding to the fields $H \sim H^*$ and the lower acoustic branch shows a hysteresis for different directions of field sweeping [8]. In fields $H \gg H^*$, the hysteresis disappears, and the AFMR spectrum takes its conventional form. This effect allows estimation of the transition field by comparing the field dependence of absorption at different frequencies. In this work, the pressure effect on AFMR of several $RbMnBr_3$ samples was studied in fields close to H^* at pressures up to 200 bar. For compression in the direction perpendicular to the binary plane, the absorption intensity strongly changed monotonically, indicating a decrease in the incommensurate transition field. The presence of the crystallographic domains inside bulky samples showed that this effect also depends on the mutual orientation of the compression direction and the direction of orthorhombic distortion of a hexagonal lattice.

Experimental results. Samples for the study were grown by the Bridgman method from the starting RbBr and $MnBr_2$ powders. They were mixed in the due stoichiometric ratio and placed in a quartz tube, which was then evacuated, unsoldered, and passed through an oven at 760°C with a velocity of 1 mm/h. The resulting crystals were annealed for several days at a temperature of about 400°C. The $RbMnBr_3$ single crystals with a size of about 1 cm^3 had flat cleavages along the binary planes, which allowed the orientation of their C_6 axis perpendicularly to the field direction to within ±0.5°.

To accomplish uniaxial compression of a sample inside the cavity, a special transmission spectrometer was designed. Apart from the input and output waveguides and the absorbing cell (cylindrical cavity with a diameter of 15 mm and a height of 10 mm), the spectrometer was equipped with a cable, one of whose ends was attached to the calibration spring and the other, to a lever mechanism. The spring was placed inside a bellows seal outside a helium Dewar flask, and the lever mechanism was attached to the waveguide walls immediately nearby the cavity. The second end of the spring was attached to a piston which moved on guides by a thread along the setup axis. A coil with a ferromagnetic core was placed inside the spring and allowed the spring stretching to be measured with a high accuracy by measuring its inductance. This ruled out the error that was introduced by the atmospheric pressure, bellows rigidity, and friction in the determination of the force applied to the sample. The sample was glued to a quartz cylinder that was put at the cavity bottom and kept from above by a copper rod. The force transmitted to the rod from the lever mechanism corresponded to the spring stretching force. Although the introduction of a quartz rod into the cavity deteriorated its Q factor (from 10^4 to $1–2 \times 10^3$, depending on the resonance mode), this did not hamper the resonance measurements. The whole setup, including the cavity with the sample, was placed in an evacuated volume. A magnetic field parallel to the setup axis was produced by a superconducting solenoid providing smooth reversible sweeping up to 60 kOe. Measurements were made at frequencies from 33 to 43 GHz mainly at a temperature of 1.3 K (appreciably lower than T_N of $RbMnBr_3$) obtained by pumping out ^{4}He vapor. The sample under study was a platelet with an area of about 4 mm^2 and a thickness of 1 mm.

The absorption lines of a $RbMnBr_3$ sample under various pressures are shown in Fig. 2. The spectra were recorded for up- and downfield sweeping at two frequencies, ν = (a) 33.2 and (b) 42.6 GHz. For the first one, the resonance field of the emitted relativistic AFMR branch (splitted in low fields) is somewhat lower than the transition field to the commensurate phase of the spin system, and, for the second frequency, it lies approximately in the hysteresis region. As seen from Fig. 2a, this absorption is absent at zero pressure for the upfield sweep and appears only upon the downfield sweep. With the buildup of pressure, the absorption amplitude in both sweep directions increases smoothly, and the resonance lines broaden. The position of the weaker maximum virtually does not change, while the stronger maximum shifts to lower fields. The intensity ratio $\alpha = I_{up}/I_{doun}$ for the split lines increases monotonically from 0 to approximately 2/3 (see Discussion). The second resonance line (near 40 kOe in

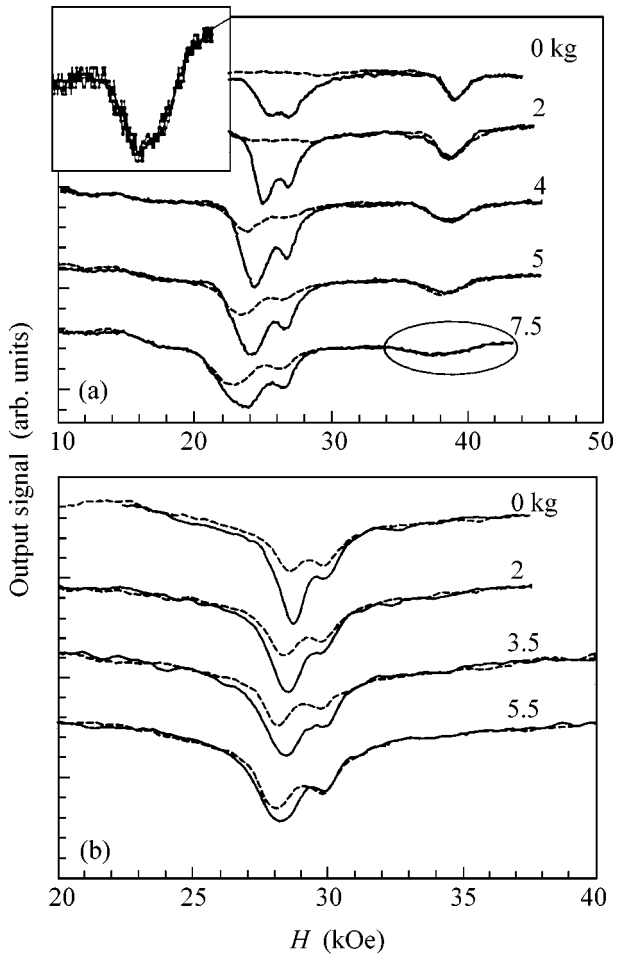

Fig. 2. Magnetic-field dependence of the resonance absorption at frequencies ν = (a) 33.2 and (b) 42.6 GHz for various pressures applied to the sample (T = 1.3 K). The dotted lines correspond to the upfield sweep and the solid line are for the downfield sweep. The fragment enclosed in the oval is shown on an enlarged scale in the inset.

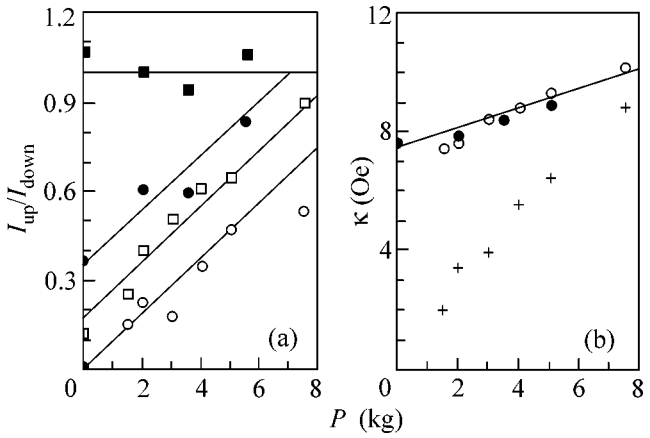

Fig. 3. (a) The I_{up}/I_{down} ratio of the absorption peaks from domain 1 (squares) and domains 2 and 3 (circles): ν = (light symbols) 33.2 and (black symbols) 42.6 GHz. (b) The parameter κ (see text) as a function of pressure; circles correspond to the relativistic branch, and crosses are for the exchange branch. The straight lines are guides to the eye.

Fig. 2a and absent in Fig. 2b) corresponds to the AFMR exchange branch, which softens after spin collapse into the collinear phase. It is also influenced by pressure, broadens, and shifts to lower fields. At a maximum force of 7.5 kg (see inset in Fig. 2a), this line is split by approximately 2 kOe. At the higher frequency (Fig. 2b), pressure influences the relativistic branch in a similar manner, i.e., leads to a monotonic increase in the absorption amplitude, line width, and the parameter α (the latter increases almost to 1), as well as to a downfield shift of the left absorption maximum. The main distinction is that the right line in this case remains virtually unchanged up to the maximal pressure, because it occurs in fields higher than H^*.

Discussion and conclusions. As is noted above, the intensity ratio of the absorption lines of the relativistic AFMR branch for the up- and downfield sweeping can be used as the main characteristic for estimating the transition field H^* from magnetic measurements. The hysteresis of the first-order transition determines the difference in the microwave absorptions in the commensurate phase. The observed pressure-induced change in the absorption amplitude for the upfield sweep and the convergence of the intensities I_{up} and I_{down} (Fig. 3a) are evidence that the uniaxial sample compression in the direction perpendicular to the binary plane reduces the transition field to the commensurate phase, which is estimated at 2–3 kOe. This fact confirms the interconnection between the appearance of the incommensurate magnetic structure and the periodic variation of the exchange interactions in the basal plane. It remains to analyze the question of the influence of uniaxial compression on the positions of resonance peaks, i.e., the pressure-induced shifts of resonance frequencies.

Note, first of all, that the splitting of a resonance line due to the uniform spin-density oscillations in a magnetic field is caused by the presence of three crystalline domains in the sample. They have approximately the same volume and differ in the direction of the orthorhombic distortions in the basal plane of the original hexagonal crystal. The distortions in each domain give rise to the anisotropy with the axis directed perpendicular to the binary plane. The anisotropy axes of different domains form an angle of 120° with each other. In our experiment, the magnetic field is directed along one ($\mathbf{x}_1$) of these axes and forms an angle of ±60° with $\mathbf{x}_2$ and $\mathbf{x}_3$. The intensity ratio of approximately 2 : 1 between the left and right peaks is evidence that the right peak corresponds to the rational field direction.

The field dependence of the relativistic AFMR branch in the commensurate phase at $\mathbf{H} \perp \mathbf{x}$ and $\mathbf{H} \parallel \mathbf{x}$ (in the basal plane) is expressed by $\nu(H) = f(H^2 \pm H_c^2)$,

where f is the increasing function (for weak distortions of a trigonal spin structure, $f(x) \sim x^{\frac{3}{2}}$) and H_c is the critical field at which the anisotropy energy and the magnetic energy are equalized at $\mathbf{H} \parallel \mathbf{x}$. In the commensurate structure, this should induce the in-plane spin-system rotation by 90°; however, in the incommensurate phase, this transition is not observed.

The value of H_c can be estimated from the splitting of this AFMR branch in a magnetic field at a given frequency in different domains. In domain 1, the field is directed along the easy axis (low-intensity line) and at an angle of 60° to this axis in domains 2 and 3. The critical field is determined by the parameter $\kappa = \sqrt{\frac{2}{3}(H_{\mathrm{res}_1}^2 - H_{\mathrm{res}_2}^2)}$ (the factor 2/3 instead of 1/2 gives an approximate correction to the mutual orientation of domains 2 and 3 at an angle of 60° rather 90°) and equal to $H_c(P = 0) \simeq \kappa_0 \simeq 7.5$ kOe at zero pressure. It is seen from Fig. 2 that this field increases under pressure, although only in domains 2 and 3, because the corresponding resonance line shifts to lower fields, while the resonance of domain 1 is not shifted. The simple estimate $H_c(P) \simeq \kappa_0 + 3\Delta\kappa(P)$ shows that the field H_c increases in domains 2 and 3 approximately twofold at the maximal pressure (Fig. 3b).

The field corresponding to the collapse of sublattices into a collinear phase also depends on the field direction. For the two limiting orientations $\mathbf{H} \parallel \mathbf{x}$ and $\mathbf{H} \perp \mathbf{x}$, it is $H_e^2 = H_{e_0}^2 \pm H_c^2$. Because of this, the splitting is also observed for the resonance line corresponding to the AFMR exchange branch (see Experimental results). The corresponding results obtained by fitting the resonance absorption at various pressures by two Lorentzian peaks are shown in Fig. 3b. The fact that the obtained H_c values deviate from the results for the relativistic branch is explained by the large line widths of the AFMR exchange branch, which hampers the exact line resolution at low pressures.

Note in conclusion that the transition field to the commensurate phase depends also on H_c. For this reason, its change in domains 2 and 3 (where H_c depends on P) is a combined effect. The pressure-induced shift of AFMR lines also affects the estimate of H^* by the method used in this work. Because of this, the observed pressure-induced changes in the resonance-peak intensities in the first domain can be considered as the only direct evidence of the H^* dependence on the exchange modulation in the basal plane.

We are grateful to I. A. Zaliznyak for the idea of the experiment and to A.I. Smirnov and M.E. Zhitomirskiĭ for helpful discussions. This work was supported in part by the Russian Foundation for Basic Research, project nos. 01-02-17557 and 03-02-16579. S.S.S. is also supported by the Foundation for Assistance of National Science.

REFERENCES

1. H. von Fink and H.-J. Seifert, Acta Crystallogr. B **38**, 912 (1982).
2. O. A. Petrenko, M. A. Lumsden, M. D. Lumsden, and M. F. Collins, J. Phys.: Condens. Matter **8**, 10899 (1996).
3. T. Kato, J. Phys. Soc. Jpn. **71**, 300 (2002).
4. L. Heller, M. F. Collins, Y. S. Yang, and B. Collier, Phys. Rev. B **49**, 1104 (1994).
5. W. Zhang, W. M. Saslow, and M. Gabay, Phys. Rev. B **44**, 5129 (1991); W. Zhang, W. M. Saslow, M. Gabay, and M. Benakli, Phys. Rev. B **48**, 10204 (1993).
6. M. E. Zhitomirsky, O. A. Petrenko, and L. A. Prozorova, Phys. Rev. B **52**, 3511 (1995).
7. A. M. Tikhonov and S. V. Petrov, Phys. Rev. B **61**, 9629 (2000).
8. I. M. Vitebskiĭ, O. A. Petrenko, S. V. Petrov, and L. A. Prozorova, Zh. Éksp. Teor. Fiz. **103**, 326 (1993) [JETP **76**, 178 (1993)]; A. N. Bazhan, I. A. Zaliznyak, D. V. Nikiforov, *et al.*, Zh. Éksp. Teor. Fiz. **103**, 691 (1993) [JETP **76**, 342 (1993)].

Translated by V. Sakun

JETP Letters, Vol. 77, No. 12, 2003, pp. 684–685. Translated from Pis'ma v Zhurnal Éksperimental'noĭ i Teoreticheskoĭ Fiziki, Vol. 77, No. 12, 2003, pp. 823–824.

Information for Authors

PACS numbers: 01.30.-y

The journal *Pis'ma Zh. Éksp. Teor. Fiz.* (and its English edition *JETP Letters*) publishes short papers that need to be urgently published and are of broad physical interest. These papers should report first observations of new physical phenomena or new fundamental theoretical results.

This journal accepts and publishes manuscripts submitted in Russian or English. All manuscripts submitted in English are checked for language. If the English text appears unreadable, the Editorial Board may request that the authors submit the Russian variant of the manuscript for publication.

All articles in *JETP Letters* are published in English. The translation of manuscripts submitted in Russian, as well as the editing of manuscripts submitted in English, is performed by the International Academic Publishing Company (IAPC) "Nauka/Interperiodica."

The total length of any paper should not exceed five journal pages in the Russian edition. This length approximately corresponds to 25 KB in *LATeX* format, including 1 KB for each figure. You can estimate the manuscript length more accurately by preparing it according to an example that is available on the Web server for the journal (http://www.jetpletters.ac.ru) by using the style file (jetpl.cls) available on the same server.

Manuscripts may be submitted to the Editorial Board in the following ways:

(1) Conventional mail to the following address: *Pis'ma Zh. Éksp. Teor. Fiz.*, ul. Kosygina 2, Moscow, 117334 Russia. A manuscript should be submitted in duplicate with figures on separate sheets (for half-tone figures, one additional copy should be submitted). Please append the e-mail and postal addresses (including the postal code), the office and home phone numbers, and the complete name and patronymic of the author to whom correspondence should be addressed. The authors of English manuscripts should also submit a floppy disk containing the text in *LATeX* format.

(2) Electronic mail to the e-mail address letters@kapitza.ras.ru. In this case, each figure should be submitted in the form of an individual file in PostScript (*.ps), EncapsulatedPostScript (*.eps), or PaintBrush (*.pcx) formats.

Acceptance or rejection of a paper for publication is decided by the Editorial Board with a proposal from the Editorial Board member specializing in the appropriate section. A manuscript can be rejected if it is not topical enough, does not provide considerable development as compared to other publications in this field, considers too specific a subject, etc. As a rule, the referee's reports on rejected papers are not sent. The authors may resubmit a rejected manuscript, appending an explanatory letter to it. In this case, the manuscript will be put under additional review.

The Editorial Board sends (or hand delivers if the authors live in Moscow) five reprints of the papers published in the Russian edition. The English version is sent to the authors in electronic form by IAPC "Nauka/Interperiodica."

MANUSCRIPT PREPARATION

The first page of a manuscript should have the following form:

THE TITLE

Initials and Surnames of the Authors

Institutions where the authors work, including city and postal code (the e-mail address of one of the authors is desirable)

Text of the Abstract

PACS: … (see http://publish.aps.org/PACS/).

Then, after one empty line, the main text follows.

Because abstracts may now be distributed separately from the papers (databases, online systems, etc.), the abstract text should be self-contained with no references or abbreviations and with understandable notation.

Abbreviations must be given in capital letters with no periods and should be explained as they are first introduced. Footnotes in the main text must be numbered consecutively in order of their appearance.

Cited references must be given in a general list at the end of a manuscript and should be numbered with an ordinal number (e.g., [1]) consecutively as they are mentioned in the main text. The reference to a journal article should cite the following: the initials and surnames of the authors, journal name, volume number (in boldface type), the first page of the paper, and year

0021-3640/03/7712-0684$24.00 © 2003 MAIK "Nauka/Interperiodica"

enclosed in parentheses. If an article is written by more than four authors, indicate only the first three, e.g.,

1. A. B. Ivanov, V. G. Petrov, I. M. Sergeev, *et al.*, Zh. Éksp. Teor. Fiz. **92**, 290 (1990) [JETP **71**, 161 (1990)].

References to books must cite the following: the initials and surnames of the authors, the complete book title, and the year and place of publication (in the case of translated books, give the information for the original in parentheses).

Use decimal points instead of commas. Three-vectors with no arrow above them must be given in boldface type.

We recommend that authors preparing figures electronically adhere to the following rules: prepare figures in the frame; direct dashes on the axes inside the figure; when possible, use Times font; use numerals (including those on the axes in an insert) and lowercase letters with a height of 3–4% of the maximum figure size (height or width) of the figures; put measurement units on the axes in parentheses. When preparing the figure, keep in mind that, as a rule, the width of a figure in printing does not exceed 82 mm; in exclusive cases, a figure can be set at the entire width of the sheet (up to 160 mm).

Examples of the preparation of a manuscript and figures, as well as a style file, are available on our Web server (http://www.jetpletters.ac.ru/).

Translated by R. Tyapaev